

Optically mediated thermal response of Quartz Tuning Forks modified with a
silicon bridge for bolometric and atmospheric sensing through Photothermal

Spectroscopy

by

John Errington Hawk

A thesis submitted in partial fulfillment of the requirements for the degree of

Doctor of Philosophy

In

Chemical Engineering

Department of Chemical and Materials Engineering
University of Alberta

© John Errington Hawk, 2019

Abstract

Due to the inherent benefits offered by the Quartz Tuning Fork (QTF) platform, QTFs have found utility in a variety of scientific applications to include, but not limited to spectroscopy, microscopy, and atmospheric sensing. It is from the intersection of these applications that the proceeding work will develop. This work will discuss the suitability and limitations of the point-mass mathematical model thus far used, and a distributed beam model will be investigated and experimentally verified for the first time with this system to allow for the detection and monitoring of optically mediated thermal signals using custom modified QTFs. To date, this model has not been investigated as to its applicability and utility for this type of modified QTF platform. Further, newly created modified QTFs will be tested to demonstrate their utility as a platform capable of conducting mid infrared (MIR) fingerprint analysis via Photothermal Spectroscopy while functioning in two distinct modes of operation, as well as testing with an off the shelf modified QTF platform that is commonly used in AFM applications. These two modes of operation will be compared to existing microcantilever based, and unmodified QTF based, photothermal spectroscopy techniques for the first time demonstrating improvement over these platforms at the same stage of development. In closing, techniques are discussed to allow for extension of this modified QTF platform for other optical regions beyond MIR and conclude with offering possible means to improve the responsivity of currently employed modified QTF chemical vapor sensors, as well as possible improvements of another competing IR fingerprinting platform.

Preface

This thesis is an original work of John Errington Hawk.

Acknowledgements

I would like to thank all those who made this work possible. In particular, I would like to thank Dr. Arindham Phani and Dr. Charles Van Neste for the stimulating discussions which would often last late into the night. All the members of the group were fantastic people. Lastly, I would like to thank my supervisor Dr Thomas Thundat for all of the assistance and support he provided throughout this program. This research was supported by the Canada Excellence Research Chairs (CERC) program.

Contents

Chapter 1: Introduction	1
1.1. Atomic Force Microscope	2
1.2. Quartz tuning forks	4
1.2.1. Imaging	4
1.3. Atmospheric sensing	11
1.3.2. Microfabricated microcantilever based sensing	11
1.3.3. Quartz tuning fork based sensing	11
1.4. Conclusion	20
1.5. References	23
Chapter 2: Operational Theory	27
2.1. Point mass model	27
2.2. Distributed Beam model	29
2.2.1. Mathematical Model	32
2.2.2. Addition of shear term at the terminal end	36
2.2.3. Sensitivity	42
2.3. References	45
Chapter 3: Experimental Method	48
3.1. QTF Platform	48

3.2.	Self-Sensing and Self-Actuating Electronics	53
3.3.	References	58
Chapter 4:	Response to HeNe laser	59
4.1.	Optically mediated response: methodology	59
4.2.	Thermal Response test	61
4.3.	Bolometric applications	64
4.3.1.	40 kHz QTFs	67
4.3.2.	32768 Hz QTFs	72
4.3.3.	Results for Optimized Conditions - 40 kHz QTF	77
4.4.	Improving Optical fill factor	86
4.5.	References	88
Chapter 5:	Atmospheric sensing–IR fingerprinting	89
5.1.	Microcantilever based - PCDS	89
5.2.	Quartz Tuning Fork based	91
5.2.1.	Quartz Enhanced Photoacoustic Spectroscopy - QEPAS	92
5.2.2.	Standoff Photoacoustic Spectroscopy	95
5.2.3.	Silicon bridge modified QTFs	98
5.3.	Akiyama probes	121
5.4.	Potential improvement for PCDS	124
5.5.	References	126

Chapter 6:	Conclusion	130
Chapter 7:	Future work	132
References		134
Appendix		145

List of tables

TABLE 2.1. NUMERICAL SOLUTION TO EQUATION 2.11 FOR THE FIRST THREE EIGENMODES. RATIO OF FREQUENCIES BETWEEN EACH EIGENMODE AS PREDICTED FROM EQUATION 2.8.....	34
TABLE 4.1. MEASURED POWER OUTPUT AND ABSORBED POWER FROM THE LDV HeNe LASER FOR ALL INTERNAL FILTERS.	66

List of figures

FIGURE 1.1. SCHEMATIC OF THE FIRST USE OF “OPTICAL BEAM BOUNCE” TECHNIQUE FOR ATOMIC FORCE MICROSCOPE, AS SHOWN BY MEYER AND NABIL [2]. REPRINTED FROM G. MEYER, N M. AMER, ERRATUM: NOVEL OPTICAL APPROACH TO ATOMIC FORCE MICROSCOPY, APPL. PHYS. LETT. 53, 1045 (1988), APPL PHYS LETT, 53(24) 12, (1988) 2400-2402, WITH THE PERMISSION OF AIP PUBLISHING.	3
FIGURE 1.2. A TYPICAL MICROFABRICATED MICROCANTILEVER AS USED FOR ATOMIC FORCE MICROSCOPY.....	4
FIGURE 1.3. SCANNING NEAR-FIELD ACOUSTIC MICROSCOPE (SNAM), AS SHOWN BY GUNTHER ET AL. [3]. REPRINTED BY PERMISSION FROM SPRINGER NATURE: SPRINGER, APPLIED PHYSICS B, <i>SCANNING NEAR-FIELD ACOUSTIC MICROSCOPY</i> , P. GUNTHER, U. CH. FISCHER, AND K. DRANSFIELD, (1989).....	5
FIGURE 1.4. MODIFIED QTF FOR NEAR-FIELD SCANNING OPTICAL MICROSCOPE (NSOM), AS SHOWN BY KARRAI ET AL. [4]. REPRINTED FROM, K. KARRAI AND R. GROBER, PIEZOELECTRIC TIP-SAMPLE DISTANCE CONTROL FOR NEAR FIELD OPTICAL MICROSCOPES, APPL PHYS LETT, 66 (14) 1842-1844 (1995), WITH THE PERMISSION OF AIP PUBLISHING.	6
FIGURE 1.5. MODIFIED QTF AS A QPLUS SENSOR, AS SHOWN BY GIESSIBL [7]. REPRINTED FROM, FRANZ J. GIESSIBL, <i>HIGH-SPEED FORCE SENSOR FOR MICROSCOPY AND PROFILOMETRY UTILIZING A QUARTZ TUNING FORK</i> , APPL PHYS LETT, VOLUME 73 NUMBER 26, 3956-3958 (1998), WITH THE PERMISSION OF AIP PUBLISHING.....	8

FIGURE 1.6. AKIYAMA PROBES. (A) SEM OF AN AKIYAMA PROBE. (B) BATCH ASSEMBLY OF AKIYAMA PROBES. THE INSET ILLUSTRATES THE CANTILEVER SUPPORT PRIOR TO ATTACHMENT. REPRINTED FROM, T. AKIYAMA ET AL, SYMMETRICALLY ARRANGED QUARTZ TUNING FORK WITH SOFT CANTILEVER FOR INTERMITTENT CONTACT MODE ATOMIC FORCE MICROSCOPY, VOLUME 74 NUMBER 1 1, 112-117, (2003), WITH THE PERMISSION OF AIP PUBLISHING. 9

FIGURE 1.7. MOTION OF AN AKIYAMA PROBE USING FINITE ELEMENT MODELING. REPRINTED FROM APPLIED SURFACE SCIENCE, 210, T. AKIYAMA, U STAUFER, N.F. DE ROOIJ, SELF-SENSING AND SELF-ACTUATING PROBE BASED ON QUARTZ TUNING FORK COMBINED WITH MICROFABRICATED CANTILEVER FOR DYNAMIC MODE ATOMIC FORCE MICROSCOPY, 18-21, (2003), WITH PERMISSION FROM ELSEVIER. 10

FIGURE 1.8. NITROCELLULOSE/TOLUENE SULFONAMIDE FORMALDEHYDE RESIN POLYMER STRAND AS SHOWN BY BOUSSAAD AND TAO. [18] REPRINTED WITH PERMISSION FROM S. BOUSSAAD AND N.J. TAO, POLYMER WIRE CHEMICAL SENSOR USING A MICROFABRICATED TUNING FORK, NANOLETTERS, VOL 3 NO 8, 1173-1176 (2003). COPYRIGHT (2003) AMERICAN CHEMICAL SOCIETY. 13

FIGURE 1.9. MULTI COMPONENT SYSTEM AS DETAILED BY REN ET AL. [19]. REPRINTED WITH PERMISSION FROM, M. REN, E.S. FORZANI, AND N. TAO, *CHEMICAL SENSOR BASED ON MICROFABRICATED WRISTWATCH TUNING FORKS*, ANAL. CHEM., 77, 2700-2707 (2005). COPYRIGHT (2005) AMERICAN CHEMICAL SOCIETY. 15

FIGURE 1.10. TSOW AND TAO PS+SC-F105 POLYMER RESPONSE TO 635 NM LASER. ESTIMATED ABSORBED POWER IS APPROXIMATELY 1.1 nW [20]. REPRINTED FROM, F. TSOW, N. TAO, *MICROFABRICATED TUNING FORK TEMPERATURE AND INFRARED*

<p><i>SENSOR</i>, APPLIED PHYSICS LETTERS, 90, 174102 (2007), WITH THE PERMISSION OF AIP PUBLISHING.....</p>	16
<p>FIGURE 1.11. TSOW AND TAO RESPONSE OF PS+SC-F105 POLYMER STRAND TO IR RADIATION EMITTED FROM A SOLDERING IRON AT 98 °C (TOP) AND 110 °C (BOTTOM), BOTH AT A DISTANCE OF 25 CM. [20] REPRINTED FROM, F. TSOW, N. TAO, MICROFABRICATED TUNING FORK TEMPERATURE AND INFRARED SENSOR, APPLIED PHYSICS LETTERS, 90, 174102 (2007), WITH THE PERMISSION OF AIP PUBLISHING.</p>	17
<p>FIGURE 1.12. TECHNIQUE FOR AFFIXING THIN POLYMER BEAMS TO QTFs AS DEMONSTRATED BY JEON’S GROUP (TOP) ACTUAL DEVICE (BOTTOM). [25] REPRINTED FROM M. YUN, S. LEE, C. YIM, N. JUNG, T. THUNDAT, AND S. JEON, <i>SUSPENDED POLYMER NANOBIDGE ON A QUARTZ RESONATOR</i>, APPLIED PHYSICS LETTERS, 103, 053109 (2013), WITH THE PERMISSION OF AIP PUBLISHING.</p>	18
<p>FIGURE 1.13. RESPONSE OF A 30 NM PS LAYER ON A QTF (A AND C) AND QCM (B AND D) TO 10%, 15%, 20%, 25%, 30%, AND 35% CONCENTRATIONS OF ETHANOL VAPOR AS DEMONSTRATED BY JEON’S GROUP. [25] REPRINTED FROM M. YUN, S. LEE, C. YIM, N. JUNG, T. THUNDAT, AND S. JEON, <i>SUSPENDED POLYMER NANOBIDGE ON A QUARTZ RESONATOR</i>, APPLIED PHYSICS LETTERS, 103, 053109 (2013), WITH THE PERMISSION OF AIP PUBLISHING.</p>	19
<p>FIGURE 2.1. A SIMPLE HARMONIC OSCILLATOR MODEL EMPLOYED TO DATE FOR MODIFIED QTF BASED CHEMICAL VAPOR SENSING. HERE, K_c REPRESENTS THE QTF TINE, K^* REPRESENTS THE POLYMER STRAND, AND M^* IS THE EFFECTIVE MASS OF THE QTF TINE.</p>	28

FIGURE 2.2. GRAPHICAL REPRESENTATION OF AN EULER-BERNOULLI BEAM WITH A SPRING AND DASHPOT ELEMENT LOCATED AT $L(x) = L$. REPRINTED FROM JE HAWK, MS GHORAISHI, ARINDAM PHANI, AND THOMAS THUNDAT, EXPLOITING BROADER DYNAMIC RANGE IN SI-BRIDGE MODIFIED QTF'S FOR SENSITIVE THERMOMETRIC APPLICATIONS, SENSORS AND ACTUATORS A: PHYSICAL, 279, 442-447 (2018)..... 36

FIGURE 2.3. CLAMPED-FREE (A) AND CLAMPED-SPRING COUPLED (B) BEAM DEFORMATION SHAPES. REPRINTED FROM JE HAWK, MS GHORAISHI, ARINDAM PHANI, AND THOMAS THUNDAT, EXPLOITING BROADER DYNAMIC RANGE IN SI-BRIDGE MODIFIED QTF'S FOR SENSITIVE THERMOMETRIC APPLICATIONS, SENSORS AND ACTUATORS A: PHYSICAL, 279, 442-447 (2018). 39

FIGURE 2.4. PREDICTED RATIO OF k^*/k_c FOR A RANGE OF FREQUENCY RESPONSES FOR DISTRIBUTED BEAM AND POINT-MASS (HOOKEAN) MODELS. REPRINTED FROM JE HAWK, MS GHORAISHI, ARINDAM PHANI, AND THOMAS THUNDAT, EXPLOITING BROADER DYNAMIC RANGE IN SI-BRIDGE MODIFIED QTF'S FOR SENSITIVE THERMOMETRIC APPLICATIONS, SENSORS AND ACTUATORS A: PHYSICAL, 279, 442-447 (2018)..... 40

FIGURE 2.5. COMPARISON OF MODELS FOR ONE OF THE QTFs USED IN THIS STUDY..... 41

FIGURE 2.6. COMPARISON OF THE PERCENT DIFFERENCE BETWEEN THE POINT-MASS AND DISTRIBUTED BEAM MODELS. 41

FIGURE 2.7. PREDICTED SENSITIVITIES OF DISTRIBUTED BEAM AND POINT-MASS (HOOKEAN) MODELS. REPRINTED FROM JE HAWK, MS GHORAISHI, ARINDAM PHANI, AND THOMAS THUNDAT, EXPLOITING BROADER DYNAMIC RANGE IN SI-

BRIDGE MODIFIED QTF'S FOR SENSITIVE THERMOMETRIC APPLICATIONS, SENSORS AND ACTUATORS A: PHYSICAL, 279, 442-447 (2018).	43
FIGURE 3.1. TYPICAL 40 KHZ QTF AS USED IN THIS STUDY.....	49
FIGURE 3.2. NANOWORLD ARROW™ TL2 LEVERS USED IN THIS STUDY.....	50
FIGURE 3.3. TYPICAL SILICON BRIDGED QTF AS USED IN THIS STUDY.	50
FIGURE 3.4. 4294A IMPEDANCE ANALYZER RESPONSE OF A QTF REMOVED FROM ITS CANISTER (LEFT) AND MODIFIED WITH A SILICON BRIDGE (RIGHT).....	51
FIGURE 3.5. POLYTEC MSA-500 LASER DOPPLER VIBROMETER IMAGE OF THE MOTION OF THE SILICON BRIDGING STRUCTURE.	52
FIGURE 3.6. MOTION OF A SILICON BRIDGE MODIFIED QTF USING A POLYTEC MSA-500 LASER DOPPLER VIBROMETER.	53
FIGURE 3.7. TUNING FORK SENSOR CONTROLLER (TFSC) USED IN THIS STUDY.	54
FIGURE 3.8. TUNING FORK SENSOR CONTROLLER HOLDER WITH PREAMPLIFIER AND VARIABLE POTENTIOMETER.	54
FIGURE 3.9. AKIYAMA PROBE (LEFT) AND CUSTOM FABRICATED QTF MOUNT (RIGHT)..	55
FIGURE 3.10. EXPERIMENTAL ARRANGEMENT.	56
FIGURE 3.11. TEFLON FLOW CELL COMPRISED OF TWO 1/2 INCH BLOCKS SANDWICHED TOGETHER WITH A 3/4 INCH PRIMARY CHAMBER (VISIBLE FROM TOP) FED THROUGH 1/8 INCH INLET AND OUTLET PORTS ON THE BOTTOM (NOT VISIBLE).....	57
FIGURE 4.1. SCHEMATIC OF CONFIGURATION FOR EXPERIMENTAL VERIFICATION OF SILICON BRIDGE MODIFIED QTF THERMAL RESPONSE.	62
FIGURE 4.2. COMPARISON OF THEORETICAL (BLACK) AND EXPERIMENTAL (BLUE) THERMAL RESPONSE OF THE MODIFIED QTF. REPRINTED FROM JE HAWK, MS	

GHORAISHI, ARINDAM PHANI, AND THOMAS THUNDAT, EXPLOITING BROADER DYNAMIC RANGE IN SI-BRIDGE MODIFIED QTF'S FOR SENSITIVE THERMOMETRIC APPLICATIONS, SENSORS AND ACTUATORS A: PHYSICAL, 279, 442-447 (2018)..... 63

FIGURE 4.3 RESPONSE OF AN AKIYAMA PROBE TO HeNe LASER LIGHT TO 332 μW , 219 μW , AND 144 μW INCIDENT POWER. (TOP) RAW OUTPUT FROM THE TFSC (BOTTOM) CONFIRMING DATA ACQUIRED USING THE LASER DOPPLER VIBROMETER. 64

FIGURE 4.4. DEVICE TESTED WHILE OPEN TO ATMOSPHERE, YET RECESSED IN FLOW CELL. POWER LEVELS ARE (RIGHT TO LEFT): 78.2 μW , 51.9 μW , 34.1 μW , 23 μW , 13 μW , 9.9 μW , 6.4 μW , AND 4.3 μW 68

FIGURE 4.5. MAXIMUM TEMPERATURE RISE FOR 78.2 μW ABSORBED POWER FOR THE FOUR DIFFERENT OPEN CELL TESTS. 69

FIGURE 4.6. EXPERIMENT #1, DEVICE TESTED WITH QUARTZ COVERSIP. POWER LEVELS ARE (RIGHT TO LEFT): 78.2 μW , 51.9 μW , 34.1 μW , 23 μW , 13 μW , 9.9 μW , 6.4 μW , AND 4.3 μW 70

FIGURE 4.7. MAXIMUM TEMPERATURE RISE FOR 78.2 μW ABSORBED POWER FOR THREE DIFFERENT QUARTZ COVERSIP COVERED CELL TESTS. 71

FIGURE 4.8. QUARTZ COVERSIP - EXPERIMENT #2 - 32768 BASE FREQUENCY QTF TESTED WITH HeNe LASER POWERS OF (LEFT TO RIGHT): 78.2 μW , 51.9 μW , 34.1 μW , 23 μW , AND 78.2 μW 73

FIGURE 4.9. GLASS COVERSIP - EXPERIMENT #1 - 32768 BASE FREQUENCY QTF TESTED WITH HeNe LASER POWERS OF (LEFT TO RIGHT): 78.2 μW , 51.9 μW , 34.1 μW , 23 μW , AND 78.2 μW 74

FIGURE 4.10. GLASS COVERSIP - EXPERIMENT #1 - 32768 BASE FREQUENCY QTF TESTED WITH HeNe LASER POWERS OF (LEFT TO RIGHT): 78.2 μW , 51.9 μW , 34.1 μW , 23 μW , AND 78.2 μW 76

FIGURE 4.11. EXPERIMENT #1 – GLASS COVERSIP – OVERHEAD LIGHTS ON - POWER LEVELS ARE (RIGHT TO LEFT): 78.2 μW , 51.9 μW , 34.1 μW , 23 μW , 13 μW , 9.9 μW ,6.4 μW , AND 4.3 μW 78

FIGURE 4.12. MAXIMUM TEMPERATURE WITH GLASS COVERSIP AND OVERHEAD LIGHTS ON FOR 78.2 μW .ABSORBED POWER..... 79

FIGURE 4.13. EXPERIMENT #1 – GLASS COVERSIP – OVERHEAD LIGHTS OFF - POWER LEVELS ARE (RIGHT TO LEFT): 78.2 μW , 51.9 μW , 34.1 μW , 23 μW , 13 μW , 9.9 μW ,6.4 μW , AND 4.3 μW 80

FIGURE 4.14. MAXIMUM TEMPERATURE WITH GLASS COVERSIP AND OVERHEAD LIGHTS OFF FOR 78.2 μW .ABSORBED POWER. 81

FIGURE 4.15. RESPONSE OF A SILICON BRIDGE MODIFIED QTF TO ABSORBED HeNe LASER. POWER LEVELS ARE (RIGHT TO LEFT): 78.2 μW , 51.9 μW , 34.1 μW , 23 μW , 13 μW , 9.9 μW ,6.4 μW AND 4.3 μW . REPRINTED FROM JE HAWK, MS GHORAISHI, ARINDAM PHANI, AND THOMAS THUNDAT, EXPLOITING BROADER DYNAMIC RANGE IN SI-BRIDGE MODIFIED QTF’S FOR SENSITIVE THERMOMETRIC APPLICATIONS, SENSORS AND ACTUATORS A: PHYSICAL, 279, 442-447 (2018). 82

FIGURE 4.16. ZOOMED IN PORTION OF FIGURE 4.19. RESPONSE OF A SILICON BRIDGE MODIFIED QTF TO HeNe LASER AT $4.3 \mu W$. REPRINTED FROM JE HAWK, MS GHORAISHI, ARINDAM PHANI, AND THOMAS THUNDAT, EXPLOITING BROADER DYNAMIC RANGE IN SI-BRIDGE MODIFIED QTF'S FOR SENSITIVE THERMOMETRIC APPLICATIONS, *SENSORS AND ACTUATORS A: PHYSICAL*, 279, 442-447 (2018)..... 83

FIGURE 4.17. RESPONSE OF PS+SC-F105 POLYMER TO 635 NM INCIDENT LIGHT (BLACK) AS SHOWN BY TSOW AND TAO [8] WHERE QTF AMPLITUDE OF OSCILLATION WAS USED AS A PROXY FOR FREQUENCY. THE RED LINE INDICATES THE LASER VOLTAGE PULSE. REPRINTED FROM, F. TSOW, N. TAO, MICROFABRICATED TUNING FORK TEMPERATURE AND INFRARED SENSOR, *APPLIED PHYSICS LETTERS*, 90, 174102 (2007), WITH THE PERMISSION OF AIP PUBLISHING 85

FIGURE 5.1. TYPICAL PCDS EXPERIMENTAL SETUP AS SHOWN BY KIM ET AL. [4] REPRINTED WITH PERMISSION FROM, S. KIM, D. LEE, R. THUNDAT, M. BAGHERI, S. JEON, AND T. THUNDAT, *PHOTOTHERMAL CANTILEVER DEFLECTION SPECTROSCOPY*, *ECS TRANSACTIONS*, 50 (12) 459-464 (2012). COPYRIGHT [2012], THE ELECTROCHEMICAL SOCIETY 90

FIGURE 5.2. QEPAS CONFIGURATIONS. (A) THE LASER IS PASSED BETWEEN THE TINES OF THE QTF. (B) THE LASER IMPINGES ONTO THE QTF. (C) THE LASER IS DIRECTED THROUGH AN ACOUSTIC RESONATOR TUBE. AS SHOWN BY KOSTEREV ET AL. [10] REPRINTED WITH PERMISSION FROM A.A. KOSTEREV, YU. A. BAKHIRKIN, R.F. CURL, AND F.K. TITTEL, *QUARTZ-ENHANCED PHOTOACOUSTIC SPECTROSCOPY*, *OPTICS LETTERS*, VOL 27 No 21, 1902-1904 (2002), OSA PUBLISHING 93

FIGURE 5.3. SPECTRAL DATA OF THE $2\nu_3$ METHANE LINE USING QEPAS. (A) DASHED CURVE DEPICTS 6.7% (RIGHT AXIS) AND THE SOLID CURVE DEPICTS 0.17% (LEFT AXIS) METHANE CONCENTRATIONS. THE TOTAL CELL PRESSURE IS 375 TORR. THE X-AXIS IS TEMPERATURE OF THE LASER USED WHICH CONTROLS THE LASER OUTPUT FREQUENCY (B) SIMULATED METHANE ABSORPTION AT 0.17% CONCENTRATION USING HITRAN'96 DATA. AS SHOWN IN [10] REPRINTED WITH PERMISSION FROM A.A. KOSTEREV, YU. A. BAKHIRKIN, R.F. CURL, AND F.K. TITTEL, QUARTZ-ENHANCED PHOTOACOUSTIC SPECTROSCOPY, OPTICS LETTERS, VOL 27 No 21, 1902-1904 (2002), OSA PUBLISHING..... 94

FIGURE 5.4. STANDOFF PHOTOACOUSTIC SPECTROSCOPY AS SHOWN IN [17]. REPRINTED FROM, C.W. VAN NESTE, L.R. SENESAC, AND T. THUNDAT, *STANDOFF PHOTOACOUSTIC SPECTROSCOPY*, APPLIED PHYSICS LETTERS, 92, 234102 (2008), WITH THE PERMISSION OF AIP PUBLISHING. 96

FIGURE 5.5. RESPONSE OF A POLY(N-ISOPROPYLACRYLAMIDE) POLYMER STRAND MODIFIED QTF AS SHOWN IN [21]. RESPONSE TO 98 °C SOLDERING IRON AT 25 CM (TOP) AND 110 °C SOLDERING IRON AT 25 CM (BOTTOM). REPRINTED FROM, F. TSOW, N. TAO, MICROFABRICATED TUNING FORK TEMPERATURE AND INFRARED SENSOR, APPLIED PHYSICS LETTERS, 90, 174102 (2007), WITH THE PERMISSION OF AIP PUBLISHING. 98

FIGURE 5.6. EXPERIMENTAL SETUP FOR INFRARED SPECTRAL DATA ACQUISITION..... 99

FIGURE 5.7. MODIFIED CUSTOM FLOW CELL WITH 5.0 CM OPTICAL TUBE WITH ZINC SELENIDE WINDOW (YELLOW) 101

FIGURE 5.8. LONG OPTICAL PATH (5.3 CM) FREQUENCY RESPONSE OF A SILICON BRIDGE
MODIFIED QTF FOR VARIOUS CONCENTRATIONS OF METHANE. 103

FIGURE 5.9. METHANE SPECTRUM AS OBTAINED BY RAHIMI ET AL. [6], THE LARGEST
CENTRAL RESPONSE IS AT Q BRANCH AT 7656 NM (1306 CM⁻¹). REPRINTED WITH
PERMISSION FROM M. RAHIMI, I. CHAE, J.E. HAWK, S.K. MITRA, AND T. THUNDAT,
*METHANE SENSING AT ROOM TEMPERATURE USING PHOTOTHERMAL CANTILEVER
DEFLECTION SPECTROSCOPY*, SENSORS AND ACTUATORS B:CHEMICAL, 221 (2015)
564-569 104

FIGURE 5.10. 5.3 CM OPTICAL PATH. FREQUENCY DIFFERENCE AFTER SUBTRACTION OF IR
BACKGROUND FOR VARIOUS CONCENTRATIONS OF METHANE GAS FOR EACH
WAVENUMBER. WITH ERROR BARS. 105

FIGURE 5.11. 5.3 CM OPTICAL PATH. FREQUENCY DIFFERENCE AFTER SUBTRACTION OF IR
BACKGROUND FOR VARIOUS CONCENTRATIONS OF METHANE GAS FOR EACH
WAVENUMBER. WITHOUT ERROR BARS..... 106

FIGURE 5.12. 5.3 CM OPTICAL PATH. CHANGE IN SPRING CONSTANT AS A FUNCTION OF
WAVENUMBER FOR VARIOUS CONCENTRATIONS OF METHANE GAS..... 107

FIGURE 5.13. 5.3 CM OPTICAL PATH. CHANGE IN SPRING CONSTANT AS A FUNCTION OF
WAVENUMBER FOR 0.05 VOL% CONCENTRATION OF METHANE GAS. 108

FIGURE 5.14. 5.3 CM OPTICAL PATH. CHANGE IN TEMPERATURE AS A FUNCTION OF
WAVENUMBER FOR VARIOUS CONCENTRATIONS OF METHANE GAS..... 109

FIGURE 5.15. 5.3 CM OPTICAL PATH. CHANGE IN TEMPERATURE AS A FUNCTION OF
WAVENUMBER FOR 0.05 VOL% CONCENTRATIONS OF METHANE GAS..... 110

FIGURE 5.16. 5.3 CM OPTICAL PATH. CHANGE IN TEMPERATURE AS A FUNCTION OF WAVENUMBER FOR LOWEST CONCENTRATIONS OF METHANE GAS TESTED. 111

FIGURE 5.17. FITTING OF CHANGE IN SPRING CONSTANT FOR VARIOUS CONCENTRATIONS OF METHANE GAS, IN TERMS OF THE NUMBER OF MOLECULES PER CM³. THE SLOPE AT EACH WAVENUMBER IS THE ABSORPTION CROSS-SECTION FOR THAT WAVENUMBER. 112

FIGURE 5.18. ABSORPTION CROSS-SECTION OF METHANE GAS AS MEASURED USING A SILICON BRIDGE MODIFIED QTF..... 113

FIGURE 5.19. ABSORPTION CROSS-SECTION DATA OBTAINED FROM PACIFIC NORTHWEST NATIONAL LABORATORY (PNNL)..... 114

FIGURE 5.20. MODIFIED CUSTOM FLOW CELL WITH ZINC SELENIDE WINDOW (YELLOW) AFFIXED DIRECTLY ON TOP. OPTICAL PATH LENGTH IS APPROXIMATELY 3 MM..... 115

FIGURE 5.21. SHORT OPTICAL PATH FREQUENCY RESPONSE OF SILICON MODIFIED QTF FOR VARIOUS CONCENTRATIONS OF METHANE..... 116

FIGURE 5.22. MEASURED FREQUENCY SHIFT BELOW THE IR BACKGROUND FOR EACH WAVENUMBER FOR VARIOUS CONCENTRATIONS OF METHANE GAS. WITH ERROR BARS. 117

FIGURE 5.23. MEASURED FREQUENCY SHIFT BELOW THE IR BACKGROUND FOR EACH WAVENUMBER FOR VARIOUS CONCENTRATIONS OF METHANE GAS. WITHOUT ERROR BARS FOR CLARITY..... 118

FIGURE 5.24. CHANGE IN SPRING CONSTANT OF THE BRIDGING ELEMENT FOR VARIOUS CONCENTRATIONS OF METHANE GAS AS A FUNCTION OF IR WAVENUMBER. 119

FIGURE 5.25. CHANGE IN TEMPERATURE OF THE BRIDGING ELEMENT FOR VARIOUS CONCENTRATIONS OF METHANE GAS AS A FUNCTION OF IR WAVENUMBER.	120
FIGURE 5.26. IR SPECTRUM OF P, Q, AND R BRANCH OF THE METHANE ν_4 ABSORPTION LINE AS ACQUIRED USING AN AKIYAMA PROBE.....	122
FIGURE 5.27. IR SPECTRUM THE Q BRANCH OF THE METHANE ν_4 ABSORPTION LINE AS ACQUIRED USING AN AKIYAMA PROBE	123

Chapter 1: Introduction

Quartz Tuning Forks, single crystal electromechanical oscillators, are foundational to the modern world. Due to their stability, low power consumption and high precision, these platforms have become invaluable as a fundamental component for time keeping and frequency measurements. These simple devices were incorporated into wristwatches with the introduction of the Seiko Quartz-Astron in 1969 and have since become ubiquitous throughout the industry with millions being produced each year.

Operating on the principle of the piezoelectric effect, which was first discovered by Jacques and Pierre Curie in 1882, quartz crystal will generate a voltage when a stress is applied (Piezoelectric effect) or deform when a voltage is applied (Piezostriktion). Exploitation of this phenomenon allows for the direct conversion of mechanical vibrations into electrical responses as well as the converse, i.e., conversion of electrical signals into mechanical responses. A QTF is an extremely simple design in which the two tines are electrically actuated via excitation of the metal thin films that are deposited on them. These electrodes' configuration will determine if the tines oscillate either in, or out, of phase. This antiphase operation is preferred as the center of mass of the system remains stationary throughout operation. In either mode of operation however, the accepted lumped element electrical model of a quartz oscillator is the Butterworth-Van Dyke model.

The Butterworth-Van Dyke model is comprised of a series resistance, inductance, and capacitance denoted R , L , and C_m respectively, which represent the motional component, in parallel with a stray capacitance denoted C_p . As is discussed in a later chapter, it is necessary to compensate for and cancel this stray, or parasitic, capacitance in order to accurately monitor the motional component of the QTF tine.

As with other comparable competing platforms like the cantilevered beams used for atomic force microscopy (AFM), QTFs have demonstrated the ability to be extended beyond their initial developmental role as timekeeping devices and, with only slight modification, have been demonstrated as stable sensing platforms while the ability to allow for purely electrical excitation and readout affords much greater simplicity and utility of the QTF platform.

1.1. Atomic Force Microscope

The advent of the atomic force microscope (AFM), in 1986 [1], opened the door to the investigation and study of the surfaces of non-conducting materials. Built off of the ground-breaking platform of the scanning tunneling microscope (STM), which was awarded the Nobel Prize in Physics in the same year, the AFM interrogated the features of a sample via the interaction between its surface and a small gold foil cantilevered beam (CL).

This configuration detected the displacement of the gold CL by monitoring the tunneling current between it and the STM tunneling tip, using this information in a

feedback loop to map the surface of the sample. Despite the success of this approach, or rather because of it, several techniques were attempted in order to simplify this arrangement and find an alternate mechanism to replace the STM. In 1988 Meyer and Amer [2] demonstrated the optical beam deflection technique, wherein they attached a mirror to the backside of a tungsten wire to reflect a Helium Neon (HeNe) laser beam onto a position sensitive detector (PSD), as shown in Figure 1.1.

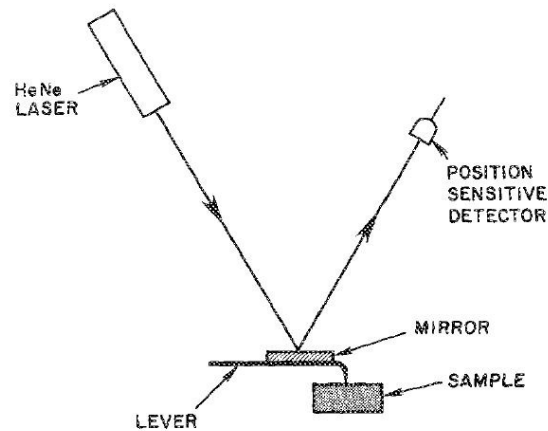


Figure 1.1. Schematic of the first use of “optical beam bounce” technique for atomic force microscope, as shown by Meyer and Nabil [2]. Reprinted from G. Meyer, N M. Amer, *Erratum: Novel optical approach to atomic force microscopy*, Appl. Phys. Lett. 53, 1045 (1988), Appl Phys Lett, 53(24) 12, (1988) 2400-2402, with the permission of AIP Publishing.

This technique, coupled with bulk microfabricated CLs, shown in Figure 1.2, would go on to become arguably the most popular implementation, and has found wide scale commercial success even to this day.

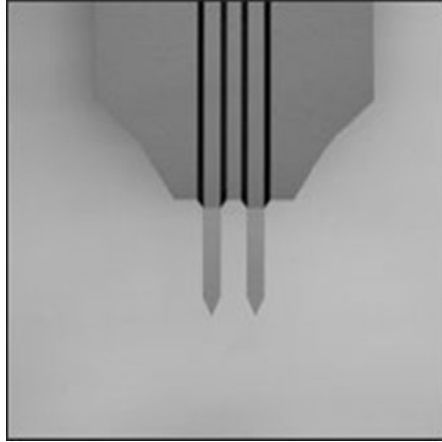


Figure 1.2. A typical microfabricated microcantilever as used for atomic force microscopy.

1.2. Quartz tuning forks

1.2.1. Imaging

Driven by the success of the AFM and its ability to successfully image the surface of non-conductive samples, alternate microscopy techniques were devised and the humble QTF made its first foray into this field. The initial approach demonstrated using a QTF was conducted by Gunther et al. in 1989 [3] and called scanning near-field acoustic microscopy (SNAM). Whereas an AFM monitors the change in deflection (some recent implementations monitor frequency) of the CL tip due to interactions between the tip and sample, SNAM monitored the changes in amplitude of an unmodified QTF caused by hydrodynamic forces in the acoustic near field region around the tip. In their work, Gunther et al. successfully imaged a grating pattern of Chromium, deposited 30 nm thick and 8 microns in periodicity, by rotating the QTF

such that the tip corner of one of the tines interacted with the sample, see Figure 1.3. Due to the lack of lateral resolution, approximately 3 microns, from the radius of curvature of the edges of the QTF, this approach did not yield continued success.

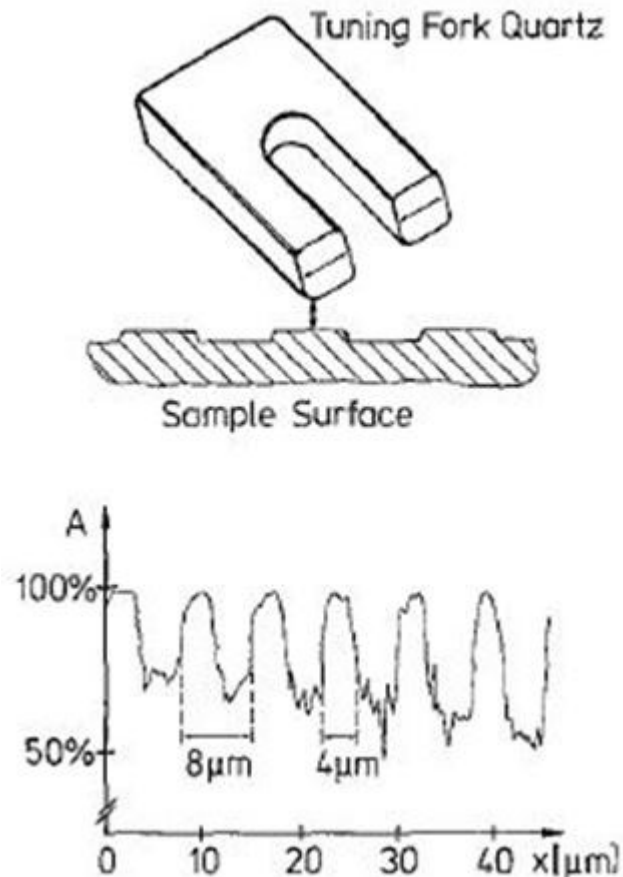


Figure 1.3. Scanning near-field acoustic microscope (SNAM), as shown by Gunther et al. [3]. Reprinted by permission from Springer Nature: Springer, Applied Physics B, *Scanning Near-Field Acoustic Microscopy*, P. Gunther, U. Ch. Fischer, and K. Dransfield, (1989).

The viability of using a QTF for microscopy applications languished for several years until Karrai et al. realized a novel approach to near field scanning optical microscopy (NSOM), in 1995, by attaching a tapered optical fiber to one of the tines [4], see Figure 1.4. The QTF was connected to a dither to facilitate mechanical actuation of the tines and, as in SNAM, the amplitude of the tine's oscillation lateral to the surface was monitored and used as the feedback mechanism to maintain the tip sample distance at a constant value.

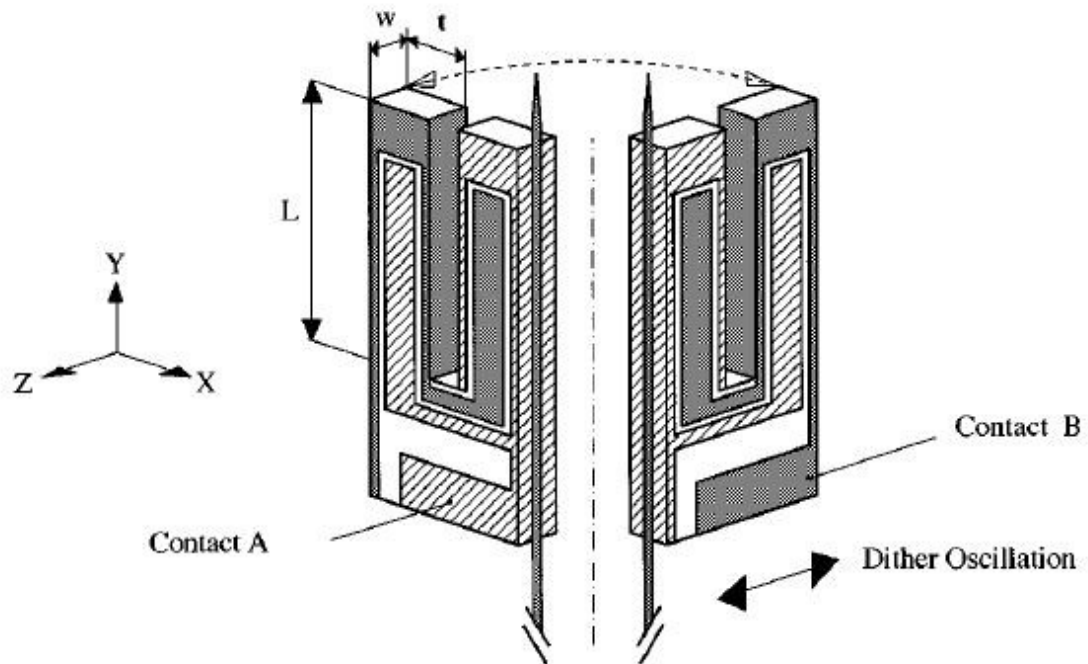


Figure 1.4. Modified QTF for near-field scanning optical microscope (NSOM), as shown by Karrai et al. [4]. Reprinted from, K. Karrai and R. Grober, *Piezoelectric tip-sample distance control for near field optical microscopes*, Appl Phys Lett, 66 (14)

1842-1844 (1995), with the permission of AIP Publishing.

Due to the fact that QTFs are highly stable and generally exhibit a high Quality factor (Q), the ratio of energy stored to lost, on the order of 10^3 , it is readily apparent that any system that uses a change in amplitude of oscillation of the tines would be cumbrously slow. This was another of the drawbacks which inhibited the further development of SNAM and, were it not for the development of the frequency modulation (FM) mode of operation for AFM [5], some of the key benefits of using a QTF for microscopy and sensing applications would have been too deleterious. At its heart, FM mode uses the CL (or QTF) itself as the frequency determining element of an oscillator circuit. Simplified by the addition of a phase locked loop (PLL), as was demonstrated by Edwards et al. in 1997 [6] who performed the first magnetic force imaging using a QTF, the high Q benefits of a tuning fork sensor could be exploited and compete with CL based AFM in terms of imaging speed.

To this point in its development, all attempts to modify a QTF for imaging applications, other than SNAM, involved affixing a probe to only one of the tines of the QTF. However, as was mentioned earlier, the most ubiquitous variant of the QTF drives the two tines in a symmetric, out-of-phase, motion. This method clearly maintains the center of mass of the system at a fixed point. Affixing a tip to only one of the tines would break the symmetry of their respective motion as the tip, on only one tine, is subjected to any tip-sample interaction and, as pointed out by Giessibl [7], this could lead to lower resolution and difficulty in interpreting the imaging signal. In order to compensate for this, Giessibl affixed a tungsten tip to one of the tines and rigidly glued

the other tine to a firmly supported structure, thus demonstrating faster scanning and greater clarity than Edwards et al.. Giessibl has patented this technique which he currently markets under the name “qPlus”. In 2000, Giessibl used this platform, shown in Figure 1.5, to obtain the first atomic resolution image of Silicon (111)-(7x7) using a QTF system, clearly demonstrating the capabilities of this imaging technique.

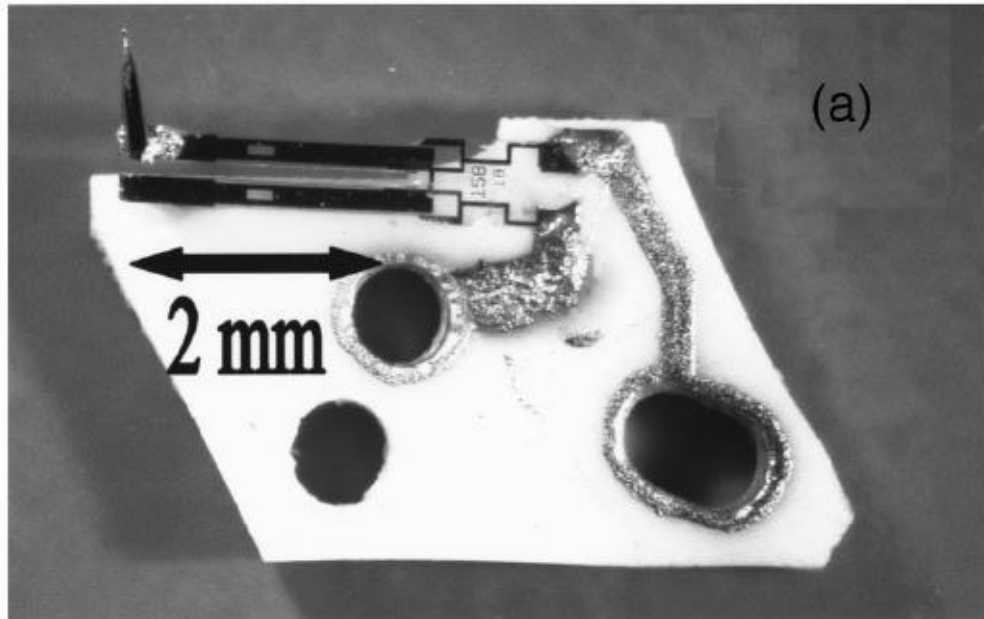


Figure 1.5. Modified QTF as a qPlus sensor, as shown by Giessibl [7]. Reprinted from, Franz J. Giessibl, *High-speed force sensor for microscopy and profilometry utilizing a quartz tuning fork*, Appl Phys Lett, Volume 73 number 26, 3956-3958 (1998), with the permission of AIP Publishing.

Following in the success of the qPlus sensor, several concepts and designs for QTF based scanning probe microscopy have been developed. However, one of the designs readily lends itself to the basis of the current work, namely detection of optical signals and environmental sensing using mid-IR fingerprinting techniques and was adapted for use in part of the following study. Whereas other approaches are mainly limited to attaching various material tips to the QTF platform, in 2003 Akiyama et al. [8] fundamentally altered the QTF based AFM approach by attaching a u-shaped microfabricated cantilever to the apex of the tines as shown in Figure 1.6.

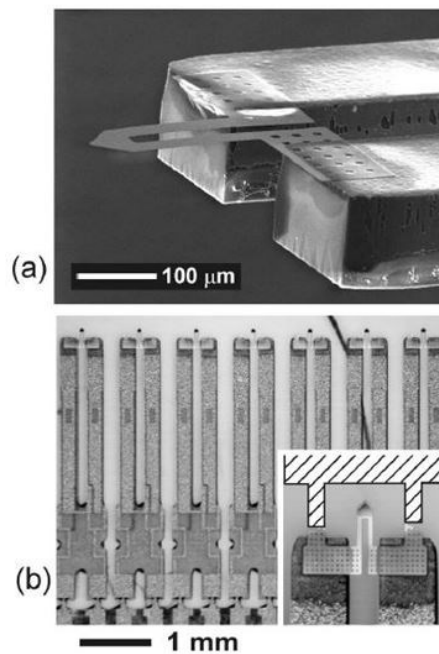


Figure 1.6. Akiyama probes. (a) SEM of an Akiyama probe. (b) Batch assembly of Akiyama probes. The inset illustrates the cantilever support prior to attachment.

Reprinted from, T. Akiyama et al, *Symmetrically arranged quartz tuning fork with soft cantilever for intermittent contact mode atomic force microscopy*, Volume 74 Number 1

1, 112-117, (2003), with the permission of AIP Publishing.

Marketed under the name “Akiyama Probe”, this platform overcomes all of the issues that initially plagued the QTF-AFM approach. It affords the full range of symmetric motion of the out-of-phase QTF tines since the load is distributed evenly across them, and benefits from the already developed electronics required to simultaneously drive and monitor the frequency of the system. However, it does exhibit some negative aspects for the current work. As is discussed in a later chapter, the design of this system does not readily lend itself to an analytical model to describe it, and modelling has only been accomplished using finite element method analysis, see Figure 1.7. The system does however afford a responsive element, the terminal CL, capable of responding to thermally mediated stimuli and was exploited for initial proof of concept.

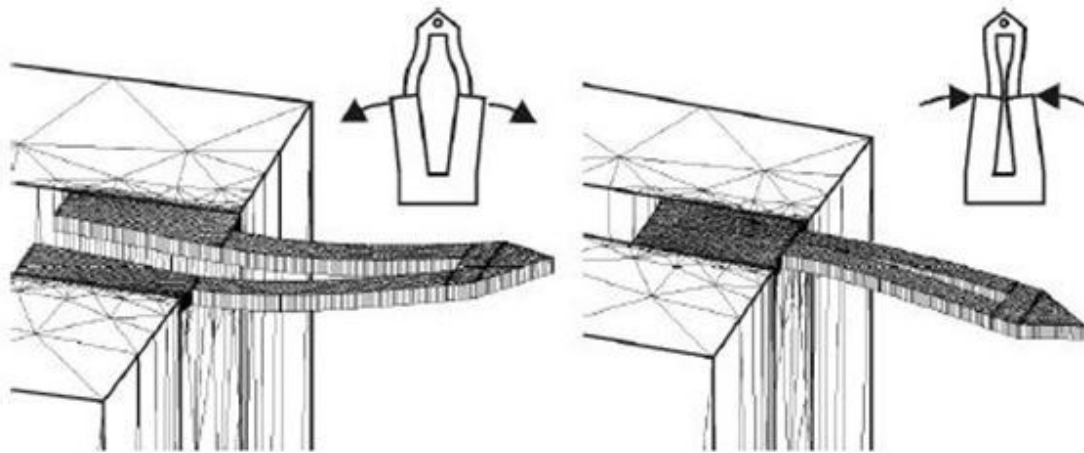


Figure 1.7. Motion of an Akiyama probe using finite element modeling. Reprinted from Applied Surface Science, 210, T. Akiyama, U Staufer, N.F. de Rooij, *Self-sensing and self-actuating probe based on quartz tuning fork combined with microfabricated cantilever for dynamic mode atomic force microscopy*, 18-21, (2003), with permission from Elsevier.

1.3. Atmospheric sensing

1.3.2. Microfabricated microcantilever based sensing

As is often the case where operational aspects and tools used in a transformative technology are co-opted to improve upon previous endeavors, this was also the case for AFM, whose primary sensing element is the microfabricated CL. Though macroscopic beams with lengths from a few mm to 100 mm had been demonstrated as sensitive detection platforms [9-11], the reduction in size and stiffness afforded by bulk fabricated micromachined CLs, coupled with the already developed detection schemes, opened new avenues for the detection and monitoring of atmospheric vapors and heat. From self-assembled monolayers on gold surfaces and polymer attachment for the detection of explosive vapors [12-14], to more recent reports using infrared (IR) for the detection of Methane gas [15], the modified CL technique has been demonstrated to be a highly sensitive platform. Indeed, a Google Scholar search readily reveals that the search term “modified microcantilever based sensing” reports in excess of twenty nine thousand results.

1.3.3. Quartz tuning fork based sensing

Unlike the broad reporting and usage of the CL platform for atmospheric sensing, the QTF system has received far less attention. Perhaps this is due to the limited number of options there are for modifying the system. The simplest approach for modifying QTFs is by applying a responsive coating to the body of the tines and recording the

frequency response as the analyte sorbs onto/into the coating. Any change in the frequency response of the QTF is attributed to increasing mass of the system as the stiffness of the tines remains unaffected. This approach has been most recently demonstrated by Deng et al. [16, 17] for the detection of volatile organic compounds (VOCs). However, a more interesting approach, at least to this author, was demonstrated in 2003 by Boussaad and Tao. In their inaugural work, rather than coat the tines of the QTF for sensing applications, a more elegant solution was found by simply pulling a small diameter strand of polymer between the apexes of the two tines. This approach allows for the balanced oscillation of the tines and, due to the small diameter of the polymer strand, rapid diffusion into the responsive element. Since this initial work, this approach has been continued by few other research groups. Indeed, the entire body of this line of research resides in only fourteen publications which are discussed below.

Seeking to find a viable competitive platform to the then burgeoning microfabricated CL, in 2003 Boussaad and Tao were the first to demonstrate their novel concept for chemical sensing using a modified QTF and demonstrated its viability in two variations. Using nitrocellulose/toluene sulfonamide formaldehyde resin, a polymer used in nail polish products, a singular strand of polymer of approximately 15 microns in diameter was pulled between the apexes of the two tines, as shown in Figure 1.8.

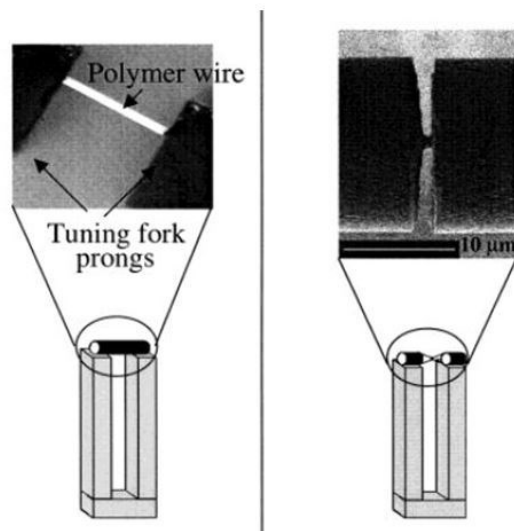


Figure 1.8. Nitrocellulose/toluene sulfonamide formaldehyde resin polymer strand as shown by Boussaad and Tao. [18] Reprinted with permission from S. Boussaad and N.J. Tao, *Polymer Wire Chemical Sensor Using a Microfabricated Tuning Fork*, NanoLetters, Vol 3 No 8, 1173-1176 (2003). Copyright (2003) American Chemical Society.

After testing the response of this system to ethanol vapor, the polymer strand was then trimmed using a focused ion beam system to the reported dimensions of 100 nm by 500 nm and tested again to the same vapors. Monitoring of this system was facilitated by “inducing near resonance oscillations in the tuning fork and detecting the change in oscillation amplitude with a lock in amplifier,” [18] a method similar to that which is routinely employed in the operation of amplitude modulated atomic force microscopy (AM-AFM). Though functional for qualitative measurements, this amplitude monitoring does preclude the ability to derive quantifiable measurements and data; nonetheless it is a commendable initial test for technique viability and successfully

demonstrated the sensing concept. Despite this seeming limitation of not being able to actively detect frequency changes during sensing operations, it is indeed possible to measure the frequency of the QTF before and after polymer deposition allowing for the quantification of material properties of the polymer wire. To this end, Boussard and Tao proffered the equation

$$E = \frac{2Lk_{fork}}{Af_0} \Delta f_0 \quad (1.1)$$

where E is the Young's Modulus, L is the length, and A is the cross-sectional area of the polymer strand respectively, k_{fork} is the spring constant of the quartz tuning fork tine, f_0 is the initial frequency, and Δf_0 is the change in frequency of the system. This model assumes the system is a point-mass simple harmonic oscillator with two springs in parallel, one spring being the tuning fork tine and the other being the polymer strand, and that the strain on the polymer strand is axial.

In 2005 Ren et al. [19] continued on with this platform and improved upon the frequency monitoring capability as well as increase the number of QTFs that were modified. By increasing the number of forks, and hence test polymers, while actively interrogated and addressing each QTF element via frequency sweeping and monitoring via lock in amplifier, they were able to simultaneously monitor the total system response to various analytes. Though extremely versatile, this approach limits the time per scan and thus data acquisition rates. A schematic of their setup is shown in Figure 1.9.

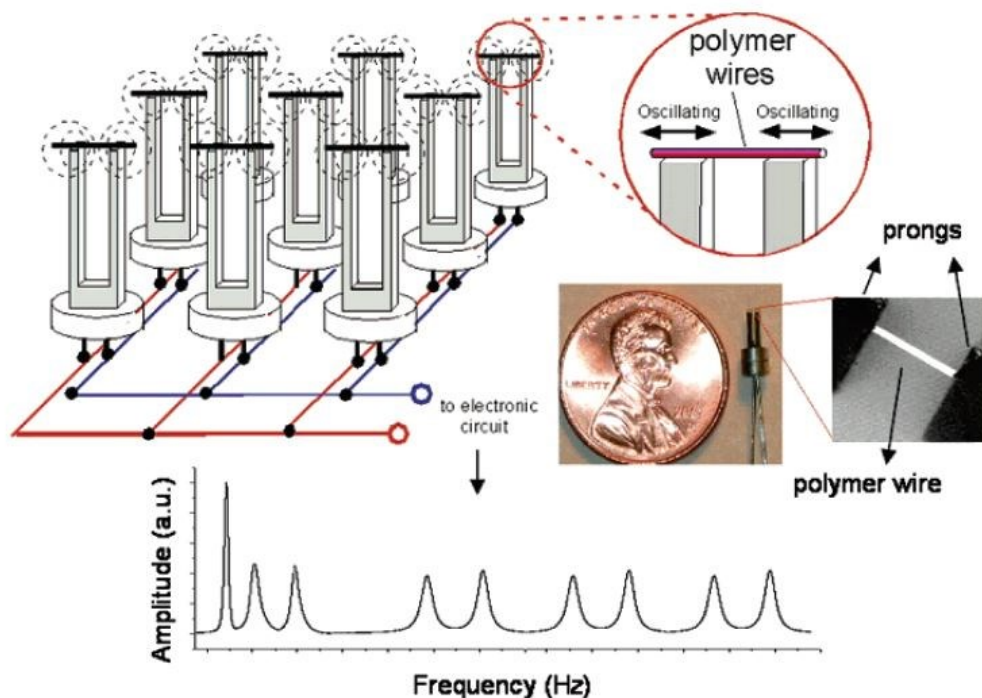


Figure 1.9. Multi component system as detailed by Ren et al. [19]. Reprinted with permission from, M. Ren, E.S. Forzani, and N. Tao, *Chemical Sensor Based on Microfabricated Wristwatch Tuning Forks*, *Anal. Chem.*, 77, 2700-2707 (2005). Copyright (2005) American Chemical Society.

In 2007, Francis Tsow and Nongjian Tao were the first, and prior to this present work the only, to utilize this platform for the monitoring of optical signals [20]. Reverting to the experimental configuration demonstrated by Boussaad and Tao, i.e. driving near resonance and monitoring the systems's amplitude via lock in amplifier, Tsow and Tao tested the response of a 9:1 mixture of polystyrene (PS) and SC-F105 (a

hyperbranched fluoroalcohol polycarbosilane) polymer strand to a 635 nm laser beam, as shown in Figure 1.10, and the IR radiation emitted from a soldering iron at 98° C and 110° C at a distance of 25 cm, as shown in Figure 1.11.

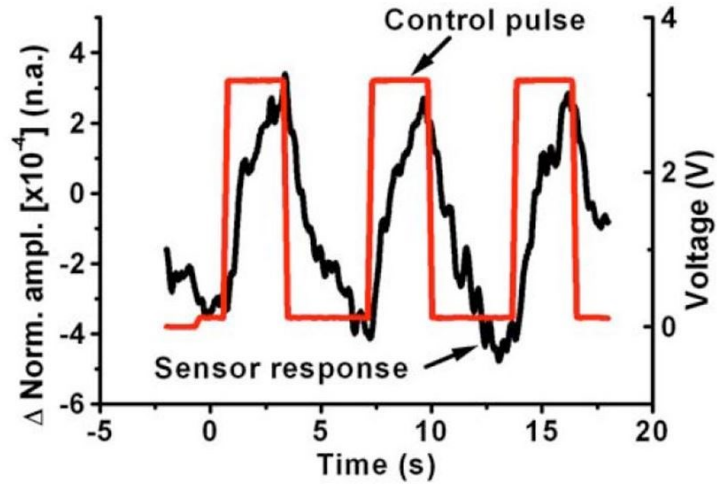


Figure 1.10. Tsow and Tao PS+SC-F105 polymer response to 635 nm Laser. Estimated absorbed power is approximately 1.1 nW [20]. Reprinted from, F. Tsow, N. Tao, *Microfabricated Tuning Fork Temperature and Infrared Sensor*, Applied Physics Letters, 90, 174102 (2007), with the permission of AIP Publishing.

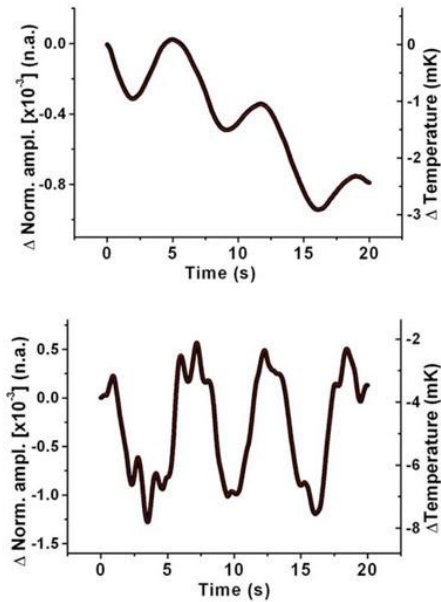


Figure 1.11. Tsow and Tao response of PS+SC-F105 polymer strand to IR radiation emitted from a soldering iron at 98 °C (Top) and 110 °C (Bottom), both at a distance of 25 cm. [20] Reprinted from, F. Tsow, N. Tao, *Microfabricated Tuning Fork Temperature and Infrared Sensor*, Applied Physics Letters, 90, 174102 (2007), with the permission of AIP Publishing.

Following this milestone of monitoring thermal response due to optical signals, the research group of Nongjian Tao improved the monitoring electronics and tested more polymers eventually leading up to the development and testing of a portable modified QTF based sensor [21-24]. There have been no further publications using this implementation of the platform from this research group after 2009.

In 2013 the research group headed by Sangmin Jeon continued the research on this platform with a novel concept [25]. By spin coating a thin layer of PS onto a silicon

wafer and then immersing the silicon wafer in water, it was possible to separate the two components as the hydrophobic PS would lift off the wafer and float on the water. The PS layer could then easily be attached to the QTF platform and the excess material could be cut off. The technique employed, and final device, can be seen in Figure 1.12.

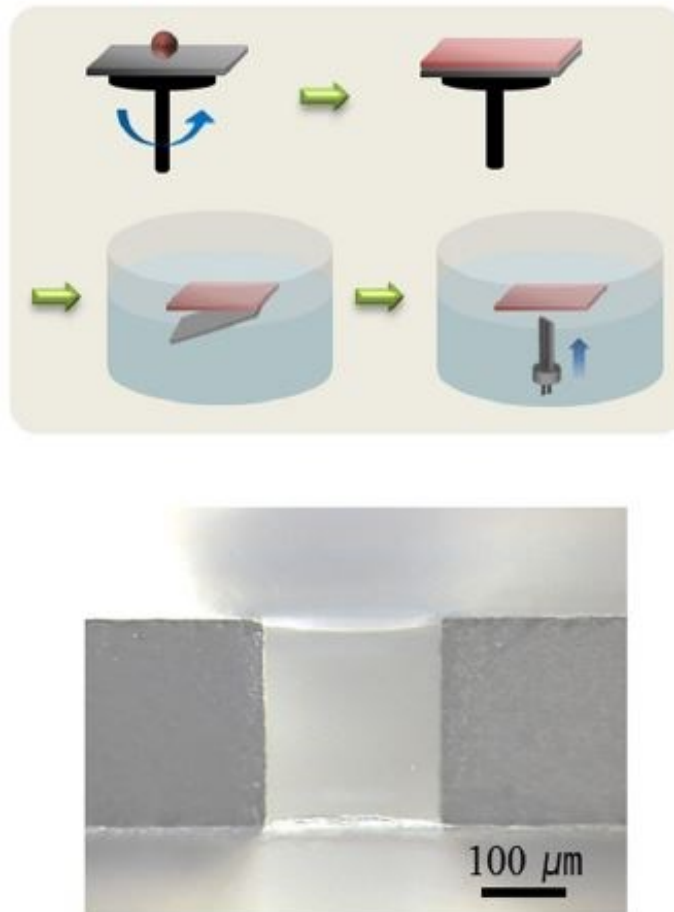


Figure 1.12. Technique for affixing thin polymer beams to QTFs as demonstrated by Jeon's group (Top) Actual device (Bottom). [25] Reprinted from M. Yun, S. Lee, C. Yim, N. Jung, T. Thundat, and S. Jeon, *Suspended polymer nanobridge on a quartz resonator*, Applied Physics Letters, 103, 053109 (2013), with the permission of AIP Publishing.

This approach was tested with ethanol vapors and the results were compared with those obtained using the same PS layer thickness spun onto a Quartz Crystal Microbalance (QCM). These results can be seen in Figure 1.13. Their results demonstrated that the response of a 32 kHz QTF, to changes in stiffness of the polymer attachment, was able to directly compete with the mass sensitivity of a 5MHz QCM. As a typical 5MHz QCM offers approximately 20 ng/cm²/Hz sensitivity, this clearly shows that monitoring changes in the Young's modulus of a polymer could be a stronger sensor platform response than the simple mass sensing offered by QCM.

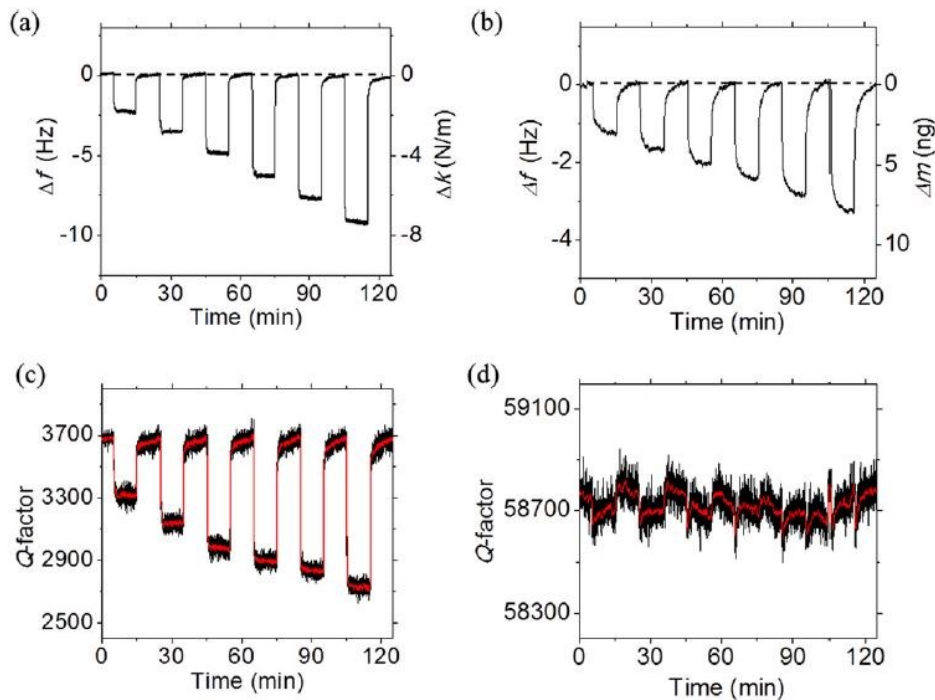


Figure 1.13. Response of a 30 nm PS layer on a QTF (a and c) and QCM (b and d) to 10%, 15%, 20%, 25%, 30%, and 35% concentrations of ethanol vapor as demonstrated by Jeon's group. [25] Reprinted from M. Yun, S. Lee, C. Yim, N. Jung, T. Thundat, and S. Jeon, *Suspended polymer nanobridge on a quartz resonator*, Applied Physics Letters, 103, 053109 (2013), with the permission of AIP Publishing.

In 2014, Jeon's group continued with two publications. In one, they demonstrated a means to improve the sensitivity of the modified QTF in a novel improvement over that shown by Tao. Whereas Tao's group increased the sensitivity of the QTF device by ion milling the polymer strand to a smaller cross section, Jeon's group found that it was possible to increase the platform's sensitivity by photo induced crosslinking of the polymer strand [26]. This was quickly followed by a demonstration of a bi-layer beam comprised of PS spin coated onto a graphene layer, the total thickness being 60 nm [27]. This group's most recent work was demonstrated in 2017 with the disclosure of yet another means to increase the sensitivity of the modified QTF platform, this time by increasing the surface area of the polymer strand. By electro spinning a poly(methyl methacrylate) (PMMA) wire under high humidity, they were able to form a porous structured strand allowing for greater exposure of the polymer strand to the analyte vapor. This was compared against a non-porous and bare QTF [28].

In 2015, the third and, thus far, final group entered into the study of this platform. Sampson et al have offered three publications discussing the finite element method (FEM) modeled dynamics [29], methanol sensing [30], and detection of methanol adulterated ethanol using aniline-doped PS wires [31].

1.4. Conclusion

To date, modified QTFs have overwhelmingly been exploited as a platform for chemical vapor sensing. Given that micron sized polymer strands offer an excellent configuration for rapid diffusion of vapor analytes, and thus their detection, this seems

an ideal use of this system. However, there is relative dearth of research into the optical signal detection capabilities of this platform. To that end, a novel modification and adaptation of this platform allowing for the detection of optical frequency radiation, specifically at 632 nm, will be disclosed herein. Further, this platform will be used for the acquisition of mid IR fingerprinting for proof of concept using Methane gas in two configuration variants by exploiting Photothermal Spectroscopy techniques. The results of this mid IR response will be compared to one of two existing unmodified QTF mid IR techniques showing improvement over one system at the same stage of development, and offer a potential means to improve the other. These results will be compared using a custom developed platform and an off the shelf Akiyama probe that is currently employed for QTF based AFM operations. Further, as all mathematical modelling of this system thus far has assumed the point mass harmonic oscillator with two springs in parallel, a distributed beam analysis will be investigated as the former model will be shown to be inapplicable in this new operational regime. In closing, alternative variants for the detection of chemical vapors and a means to improve the responsivity of the polymer strand modified QTFs currently employed will be included.

In the following chapters, the background material necessary to successfully implement and understand the system's behavior will be detailed. In Chapter 2, the mathematical model will be presented followed with the experimental methodology in Chapter 3. Chapter 4 will validate the mathematical model and proceed to demonstrate the system's response to HeNe laser light, and Chapter 5 will fully implement all of the concepts presented into a unified procedure to utilize this novel platform as a mid-IR

fingerprinting platform in two distinct modes of operation. Conclusions will be presented in Chapter 6 followed by future work and study applications in Chapter 7.

1.5. References

- 1- G. Binnig, C.F. Quate, and Ch. Gerber, *Atomic Force Microscope*, Phys Rev Lett, Vol 56 number 9 pg 930-933 (1986).
- 2- G. Meyer, N M. Amer, *Erratum: Novel optical approach to atomic force microscopy*, Appl. Phys. Lett. 53, 1045 (1988), Appl Phys Lett, 53(24) 12, (1988) 2400-2402.
- 3- P. Gunther, U. Ch. Fischer, and K. Dransfield, *Scanning Near-Field Acoustic Microscopy*, Applied Physics B, 48, 89-92 (1989).
- 4- K. Karrai and R. Grober, *Piezoelectric tip-sample distance control for near field optical microscopes*, Appl Phys Lett, 66 (14) 1842-1844 (1995).
- 5- T.R. Albrecht, P. Grutter, D. Horne, and D. Rugar, *Frequency modulation detection using high- Q cantilevers for enhanced force microscopy sensitivity*, J. Appl. Phys., 69 (2) (1991)
- 6- H. Edwards, L. Taylor, and W. Duncan, *Fast, high-resolution atomic force microscopy using a quartz tuning fork as actuator and sensor*, J. Appl. Phys., 82 (3), (1997).
- 7- Franz J. Giessibl, *High-speed force sensor for microscopy and profilometry utilizing a quartz tuning fork*, Appl Phys Lett, Volume 73 number 26, 3956-3958 (1998).
- 8- T. Akiyama, U. Staufer, and N.F.de Rooij, *Self-sensing and self-actuating probe based on quartz tuning fork combined with microfabricated cantilever for dynamic mode atomic force microscopy*, Applied Surface Science, 210 (2003) 18-21.

- 9- P.J. Shaver, *Bimetal Strip Hydrogen Gas Detectors*, Rev. Sci. Instr., 40, 901-905 (1969).
- 10- E.H. Taylor, W.C. Waggener, *Measurement of Adsorption Forces*, J. Phys. Chem., 83: 1361-1362 (1979).
- 11- R.V. Jones, *The Detection of Thermal Radiation Using Linear Expansion*, Proceedings of the Royal Society of London. Series A, Mathematical and Physical Sciences, 249: 100 (1959).
- 12- L.A. Pinnaduwege, V. Boiadjiev, J.E. Hawk, and T. Thundat, *Sensitive detection of plastic explosives with self-assembled monolayer-coated microcantilevers*, Applied Physics Letters 83 (7) 1471-1473 (2003).
- 13- L.A. Pinnaduwege, J.E. Hawk, V. Boiadjiev, and T. Thundat, *Use of Microcantilevers for the Monitoring of Molecular Binding to Self-Assembled Monolayers*, Langmuir 19 (19) 7841-7844 (2003).
- 14- L.A. Pinnaduwege, T. Thundat, J.E. Hawk, D.L. Hedden, P.F. Britt, E.J. Houser, S. Stepnowski, R.A. McGill, D Bubb, *Detection of 2,4-dinitrotoluene using microcantilevers*, Sensors and Actuators B: Chemical, 99 (2-3) 223-229 (2004).
- 15- M. Rahimi, I. Chae, J.E. Hawk, S.K. Mitra, T. Thundat, *Methane sensing at room temperature using photothermal cantilever deflection spectroscopy*, Sensors and Actuators B: Chemical, 221, 564-569 (2015).
- 16- Y. Deng, C. Chen, X. Qin, X. Xian, T.L. Alford, H. W. Choi, F. Tsow, and E.S. Forzani, *Aging effect of a molecularly imprinted polymer on a quartz tuning*

- fork for detection of volatile organic compounds*, Sensors and Actuators B: Chemical, 211 (2015) 25-32.
- 17- Y. Deng, N. Liu, F. Tsow, X. Xian, and E. Forzani, *Adsorption Thermodynamic Analysis of a Quartz Tuning Fork Based Sensor for Volatile Organic Compounds Detection*, ACS Sensors, 2 (2017) 1662-1668.
- 18- S. Boussaad and N.J. Tao, *Polymer Wire Chemical Sensor Using a Microfabricated Tuning Fork*, NanoLetters, Vol 3 No 8, 1173-1176 (2003).
- 19- M. Ren, E.S. Forzani, and N. Tao, *Chemical Sensor Based on Microfabricated Wristwatch Tuning Forks*, Anal. Chem., 77, 2700-2707 (2005).
- 20- F. Tsow, N. Tao, *Microfabricated Tuning Fork Temperature and Infrared Sensor*, Applied Physics Letters, 90, 174102 (2007).
- 21- F. Tsow, E.S. Forzani, and N.J. Tao, *Frequency-Coded Chemical Sensors*, Anal. Chem., 80, 606-611 (2008).
- 22- F. Tsow, E. Forzani, A. Rai, R. Wang, R. Tsui, S. Mastroianni, C. Knobbe, A.J. Gandolfi, and N.J. Tao, *A Wearable and Wireless Sensor System for Real-Time Monitoring of Toxic Environmental Volatile Organic Compounds*, IEEE Sensors Journal, Vol 9, No 12, (2009).
- 23- R. Wang, F. Tsow, X. Zhang, J. Peng, E.S. Forzani, Y. Chen, J.C. Crittenden, H. Destailats, and N. Tao, *Real-Time Ozone Detection Based on a Microfabricated Quartz Crystal Tuning Fork Sensor*, Sensors, 9, 5655-5663 (2009).
- 24- A. Rai, F. Tsow, S. Nassirpour, J. Bankers, M. Spinatsch, M.P. He, E.S. Forzani, and N.J. Tao, *Selective detection of sulfur derivatives using*

- microfabricated tuning fork-based sensors*, Sensors and Actuators B: Chemical, 140, (2009) 490-499.
- 25- M. Yun, S. Lee, C. Yim, N. Jung, T. Thundat, and S. Jeon, *Suspended polymer nanobridge on a quartz resonator*, Applied Physics Letters, 103, 053109 (2013).
- 26- S. Lee, M. Yun, S. Jeon, *A tunable microresonator sensor based on a photocrosslinking polymer nanowire*, Applied Physics Letters, 104, 053506 (2014).
- 27- M. Yun, E. Lee, K. Cho, and S. Jeon, *Enhanced sensitivity of a microfabricated resonator using a graphene-polystyrene bilayer membrane*, Applied Physics Letters, 105, 173116 (2014).
- 28- S. Hwang, W. Kim, H. Yoon, and S. Jeon, *Performance Enhancement of a Microfabricated Resonator Using Electrospun Nanoporous Polymer Wire*, ACS Sensors, (2017) 2, 1355-1358.
- 29- S.A. Sampson, K.S. Date, S.V. Panchal, A. Ambrale, and S.S. Datar, *Investigation of QTF based gas sensors*, Sensors and Actuators B: Chemical, 216 (2015) 586-594.
- 30- S.A. Sampson, S.V. Panchal, K.S. Date and S.S. Datar, *QTF Based Methanol Sensors*, Proceedings of the 2015 2nd International Symposium on Physics and Technology of Sensors, 8-10th March, 2015, Pune, India.
- 31- S.A. Sampson, S.V. Panchal, A. Mishra, S. Banerjee, and S.S. Datar, *Quartz tuning fork based portable sensor for vapor phase detection of ethanol by using aniline-doped microwires*, Microchim Acta, (2017) 184, 1659-1667.

Chapter 2: Operational Theory

In order to attempt to quantify changes in the system's behavior and response, it is first necessary to present an acceptable mathematical framework from which to proceed. Whereas the forthcoming mathematical model has been previously employed for certain AFM applications, it has not been implemented within the framework of bridge modified QTFs. It is with this in mind that the model is presented so that it may be investigated whether it is adequate to describe the system at hand in the event of failure of the point-mass model which is currently employed by other practitioners.

2.1. Point mass model

A point-mass model is typically assumed for small amplitude flexural oscillations of rigid beams such as microfabricated CLs and QTFs. To this end, a Hookean response is assumed such that $F=-kx$, where k is the spring constant and x is displacement. Imposition of Newton's second law, and the assumption of a sinusoidal driving force, readily resolves to the solution for the natural frequency of the system

$$\omega = 2\pi f = \sqrt{\frac{k}{m}} \quad (2.1)$$

where ω is the angular frequency, k is the spring constant, and m is the mass of the system, respectively. This Hookean assumption affords the opportunity to quickly

approximate the deflections and natural resonance frequency of CL beams, and has been used almost exclusively thus far in the study of the modified QTFs discussed in Chapter 1.

By employing the model shown in Figure 2.1, quantification of the relative frequency shift caused by imposition of a terminally attached polymer spring, k^* , in parallel to the spring element which represents the QTF tine, k_c , is expressed as

$$\omega_f = \sqrt{\frac{k^* + k_c}{m^*}} = \omega_0 \sqrt{1 + \frac{k^*}{k_c}} \quad (2.2)$$

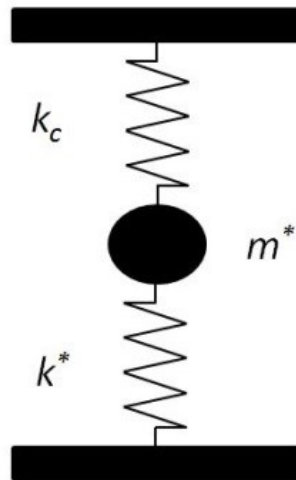


Figure 2.1. A simple harmonic oscillator model employed to date for modified QTF based chemical vapor sensing. Here, k_c represents the QTF tine, k^* represents the polymer strand, and m^* is the effective mass of the QTF tine.

This formalism has been used in the study of the response of QTF oscillators which have had a polymer strand [1] or polymer bridge [2] attached to the terminal ends of the fork. However, it has been shown that the point mass model fails to accurately predict quantitatively correct values for the amplitudes and resonant frequencies when k^* is of the same order of magnitude, or larger than, the spring constant, k_c , of the QTF tine [3]. While this is not the case for small radius polymeric strands pulled between the tines of a QTF, it is the case for the devices which were custom fabricated for this work and an alternate model must accordingly be found.

2.2. Distributed Beam model

Several analytical solutions to evaluate transversely vibrating beam's deflection and frequency have been put forth and find frequent utility, two of the most commonly utilized being Timoshenko beam theory [4, 5] and Euler-Bernoulli beam theory [6], also called classical beam theory. Being the progenitor of the analytical techniques which followed, Euler-Bernoulli beam theory relies on certain conditional requisites, namely [7]

- 1- One of the dimensions is much larger than the other two.
- 2- The material is Hookean, i.e. there is a linear relation between stress and strain.

[8].

- 3- The angle of rotation is small, such that the small angle assumption is applicable.
- 4- Planes perpendicular to the neutral axis remain perpendicular after any deformation.
- 5- The cross-section is symmetric such that the neutral axis coincides with the centroidal axis.
- 6- The Poisson effect can be neglected.

Although Timoshenko theory has been shown to be an improvement over classical beam theory in that it allows for relaxation of conditions 4, the shear is not considered constant over the cross-section, and 6, Euler-Bernoulli beam theory has been demonstrated to reveal excellent agreement with experimental results when analyzing Giessibl's modified QTF system, the qPlus [9], and will be used throughout this current work. Nonetheless, both analytical solutions can be readily calculated and provide a deeper understanding of how differing parameters can influence the vibration, which lies outside the ability of Hookean type approximations.

Given that the success and utility afforded by the AFM was the impetus for the advent of the modified QTF based systems which followed, it is unsurprising that the mathematical models which can be used to describe the AFM CL are also applicable for use with modified QTFs. Indeed, both systems are simply nothing more than cantilevered beams clamped at one end and free at the other, and are equally capable of being modeled as a distributed beam using classical beam theory. The only parameter

which differentiates the two however, is the boundary condition which is applied to the free end of the beam, namely the shear condition at the terminal end. Whether discussing the modified QTFs which have been used for chemical sensing, as shown in Chapter 1, or the qPlus system developed by Giessibl, this shear term is indeed negligible and the simple harmonic oscillator is a viable model [10]. However, in the course of this work it was found that, using the custom modified QTFs demonstrated herein, this shear term could not be neglected and still yield viable results. The appropriate mathematical model was developed for certain AFM techniques, namely ultrasonic force microscopy (UFM), atomic force acoustic microscopy (AFAM), and scanning acoustic force microscopy (SAFM). All of these techniques require a more forceful interface between the CL and sample, and the terminal shear is non-negligible. This more appropriate model has not, to the author's knowledge, been tested for viability using a modified QTF platform, thus its adequacy to describe the custom modified QTF system used in this work will be investigated and discussed to follow.

2.2.1. Mathematical Model

The classical beam equation of motion for damped transverse flexural vibrations is given as [11]:

$$EI \frac{\delta^4 y}{\delta x^4} + \eta_{air} \rho A \frac{\delta y}{\delta t} + \rho A \frac{\delta^2 y}{\delta t^2} = 0 \quad (2.3)$$

where E is the Young's modulus, ρ is mass density, A is the cross sectional area, I is the area moment of inertia, and η_{air} is a damping constant due to dissipation in air, with $y(x)$

being beam deflection, $\frac{\delta y}{\delta x}$ is beam slope, $\frac{\delta^2 y}{\delta x^2}$ is torsional moment, and $\frac{\delta^3 y}{\delta x^3}$ is shear

force at position x . It is necessary to find a time harmonic solution with angular frequency $\omega = 2\pi f$. The solution of the differential equation may be expressed as [12]

$$y(x,t) = y(x) \cdot y(t) = (c_1 e^{\alpha x} + c_2 e^{-\alpha x} + c_3 e^{i\alpha x} + c_4 e^{-i\alpha x}) e^{i\omega t} \quad (2.4)$$

Where c_1 , c_2 , c_3 , and c_4 are constants. Upon substitution of Equation 2.4 into Equation 2.3, it is a straightforward process to obtain the dispersion relation for the flexural wave with the complex wave number α

$$EI\alpha^4 + i\rho A\eta_{air}\omega - \rho A\omega^2 = 0 \quad (2.5)$$

which can be reduced to

$$\alpha_{\pm} = \pm 4 \sqrt{\frac{\rho A}{EI} (\omega^2 \mp i \eta_{air} \omega)} \quad (2.6)$$

Given the high quality factors, defined as the ratio of energy stored to lost, of the QTFs which will be used throughout this work, air damping will be assumed to be negligible, and the dispersion relation can be simplified to

$$f = \frac{(\alpha L)^2}{2\pi} \frac{1}{L^2} \sqrt{\frac{EI}{\rho A}} \quad (2.7)$$

For conditions such that the beam dimensions do not change, Equation 2.7 is valid for all vibrational modes and allows a simple method to determine the dimensionless wave number, αL , for the beam's respective boundary conditions from a measureable quantity, namely the frequency.

$$\frac{f}{(\alpha L)^2} = \frac{1}{2\pi L^2} \sqrt{\frac{EI}{\rho A}} = \frac{f_{1,free}}{(\alpha_{1,free} L)^2} \quad (2.8)$$

In order to initially evaluate $(\alpha_{1,free} L)$, an alternate expression for the general solution for the mode shape $y(x)$ given by,

$$y(x) = A_1 (\cos(\alpha x) + \cosh(\alpha x)) + A_2 (\cos(\alpha x) - \cosh(\alpha x)) + A_3 (\sin(\alpha x) + \sinh(\alpha x)) + A_4 (\sin(\alpha x) - \sinh(\alpha x)) \quad (2.9)$$

where A_1 , A_2 , A_3 , and A_4 are constants, can be employed. After using Equation 2.9 in Equation 2.3 and upon imposition of the boundary conditions for a clamped-free beam,

$$x = 0 : \left\{ \begin{array}{l} y(x) = 0 \\ \frac{\delta y(x)}{\delta x} = 0 \end{array} \right\} \quad x = L : \left\{ \begin{array}{l} \frac{\delta^2 y}{\delta x^2} = 0 \\ \frac{\delta^3 y}{\delta x^3} = 0 \end{array} \right\} \quad (2.10)$$

textbooks [13,14] give the solution for a beam with one end clamped and the other end free:

$$\cos \alpha_n L \cosh \alpha_n L + 1 = 0 \quad (2.11)$$

Numerical solutions of Equation 2.11 will provide the results for the roots $\alpha_n L$ for each eigenmode of the beam, where $n = \{1, 2, 3, \dots\}$, and the first three solutions are given in Table 2.1.

Table 2.1. Numerical Solution to Equation 2.11 for the first three eigenmodes. Ratio of frequencies between each eigenmode as predicted from Equation 2.8.

n	$(\alpha_n L)_{free}$	$f_{n,free} / f_{1,free}$
1	1.87510	1
2	4.69409	6.27
3	7.85476	17.55

2.2.1.1. Calculation of distributed beam mass as an equivalent point mass.

Interestingly, using the formalism from Equation 2.8 allows a straightforward process to evaluate the effective mass of a distributed beam, as is commonly used with modified CL sensors [15] for employment of the Hookean, point-mass model. Therein the effective mass of the beam, m^* , is related to the total mass of the beam, m_b , through the relation $m^* = nm_b$ [16]. Where n is a geometric parameter given the value of 0.24 for a rectangular shaped beam [17].

Recalling the Hookean model and Equation 2.1:

$$\omega_{1,free} = \sqrt{\frac{k_c}{m^*}} \equiv \omega_0 \quad (2.12)$$

and realization that the spring constant of a rectangular cantilevered beam can be expressed as:

$$k_c = \frac{3EI}{L^3} = \frac{Ewt^3}{4L^3} \quad (2.13)$$

One can solve for the effective mass of a beam using the complex wave number, αL , from Equation 2.7:

$$m^* = \frac{k_c}{\omega_{1,free}^2} = \frac{3\rho Lwt}{(\alpha_{1,free}L)^4} \approx \frac{1}{4}m \quad (2.14)$$

Though this formalism using m^* will not be used in the following work, this approach offers great facility in the derivation of the effective mass of a rectangular distributed beam as is routinely common when working with AFM cantilevered beam sensors.

2.2.2. Addition of shear term at the terminal end

Although the solution given by Equation 2.11 provides a ready means to evaluate a clamped-free distributed beam system, the imposition of a bridging element at the apex of the QTF tines, as shown in Figure 2.2, alters the shear force at $x = L$, leading to a different boundary condition at this point.

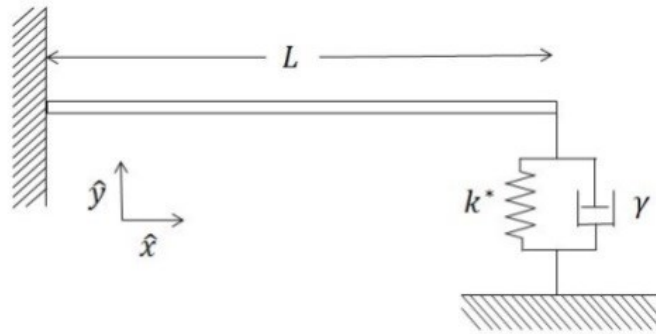


Figure 2.2. Graphical representation of an Euler-Bernoulli beam with a spring and dashpot element located at $L(x) = L$. Reprinted from JE Hawk, MS Ghoraishi, Arindam Phani, and Thomas Thundat, *Exploiting broader dynamic range in Si-bridge modified*

QTF's for sensitive thermometric applications, Sensors and Actuators A: Physical, 279, 442-447 (2018).

With the inclusion of a spring element, k^* , and dashpot, γ , representing any internal damping of the spring element, the shear term becomes

$$EI \frac{\delta^3 y}{\delta x^3} = k^* y(t) + \gamma \frac{\delta y(t)}{\delta t} \quad (2.15)$$

which can be recast into the form:

$$\frac{\delta^3 y}{\delta x^3} = \frac{1}{EI} (k^* y(t) + \gamma \omega y(t)) \quad (2.16)$$

During the course of this work, it was assumed that internal damping of the spring element was negligible and was thus excluded from further computations. Simplification of Equation 2.16 is accomplished using the substitution of the spring constant of the tuning fork tine, k_c

$$EI = \frac{k_c L^3}{3}$$

to obtain:

$$\frac{\delta^3 y}{\delta x^3} = y(t) \left(\frac{3k^*}{k_c L^3} \right) \quad (2.17)$$

This model was originally employed to describe vibrations of surface-coupled AFM CLs and it was therein that the fundamental solution used throughout this work [18, 19] was initially disclosed.

$$(1 + \cos \alpha L \cosh \alpha L) + \frac{3k^*}{(\alpha L)^3 k_c} (\sin \alpha L \cosh \alpha L - \sinh \alpha L \cos \alpha L) = 0 \equiv \Gamma \quad (2.18)$$

There are several interesting points to this equation which should be noted. When the spring element $k^* \rightarrow 0$, one obtains the standard equation for a clamped-free beam, given by the first term in Equation 2.18, and when the spring element $k^* \rightarrow \infty$, one obtains the standard equation for a clamped-pinned beam, given as the second term in Equation 2.18. The multiplicative factor, $\frac{3k^*}{(\alpha L)^3 k_c}$, being the determining component.

As the stiffness of the spring element varies, whether due to chemical vapors interacting with a polymer strand, or thermally induced stress changes in a solid bridging element, the dimensionless wavenumber, αL , and the beam shape will smoothly vary throughout these two extremes, as shown in Figure 2.3.

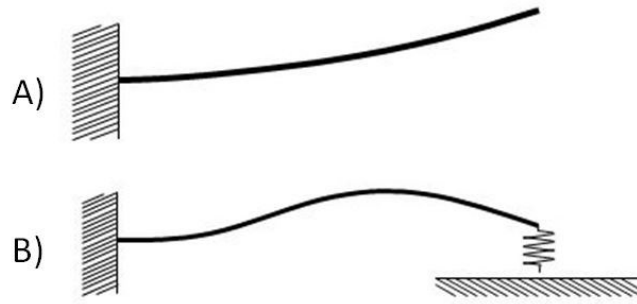


Figure 2.3. Clamped-free (A) and clamped-spring coupled (B) beam deformation shapes. Reprinted from JE Hawk, MS Ghorashi, Arindam Phani, and Thomas Thundat, *Exploiting broader dynamic range in Si-bridge modified QTF's for sensitive thermometric applications*, Sensors and Actuators A: Physical, 279, 442-447 (2018).

As was discussed previously, for small values of k^*/k_c the point-mass and clamped-spring coupled beam model yield similar results; however, as $k^*/k_c \rightarrow 1$ the two models begin to diverge drastically. Comparison of the relative frequency shift using the clamped-spring coupled model and point mass model is shown in Figure 2.4 and zoomed in Figure 2.5 with the percent difference between the distributed beam model and point-mass model shown in Figure 2.6.

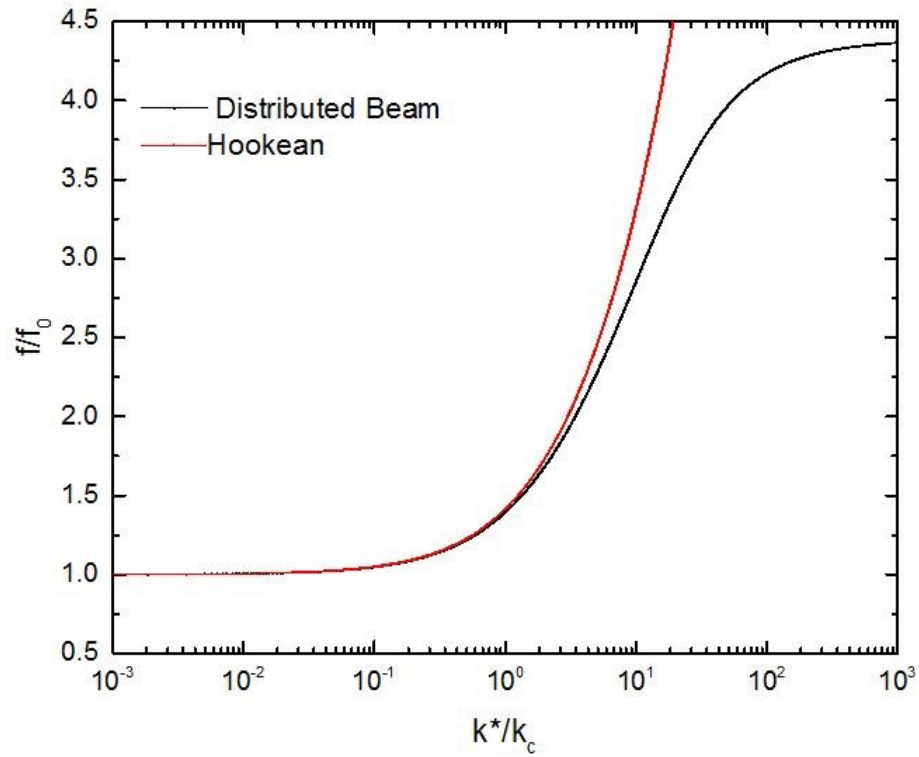


Figure 2.4. Predicted ratio of k^*/k_c for a range of frequency responses for distributed beam and point-mass (Hookean) models. Reprinted from JE Hawk, MS Ghorraishi, Arindam Phani, and Thomas Thundat, *Exploiting broader dynamic range in Si-bridge modified QTF's for sensitive thermometric applications*, Sensors and Actuators A: Physical, 279, 442-447 (2018).

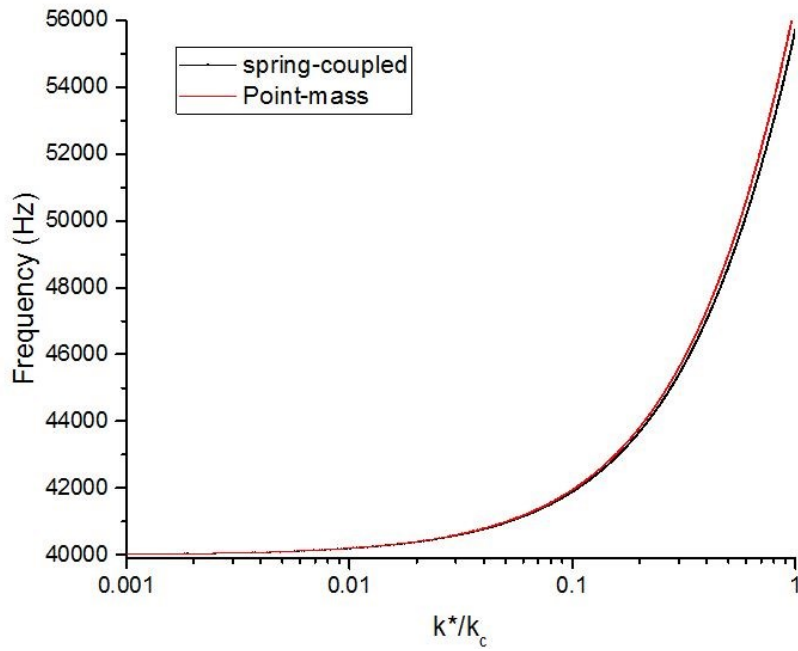


Figure 2.5. Comparison of models for one of the QTFs used in this study.

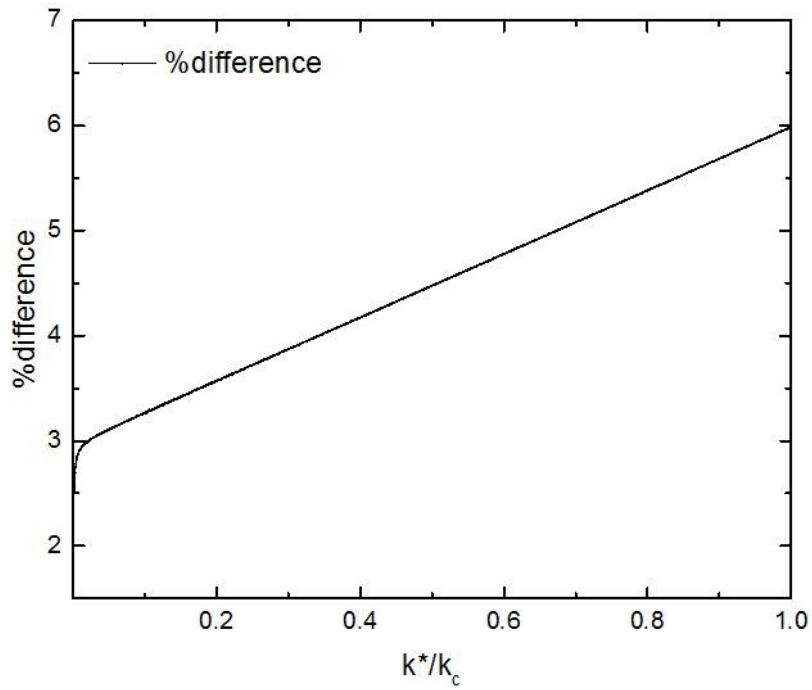


Figure 2.6. Comparison of the percent difference between the point-mass and distributed beam models.

2.2.3. Sensitivity

Comparison of the sensitivities, defined as the change in frequency per change in stiffness, of both the point-mass and the clamped-spring coupled beam model are achieved as follows. Inspection of the point-mass model, Equation 2.1, readily reveals

that $\frac{df}{dk} \Big|_{\lim k^* \rightarrow 0} = \frac{1}{2}$. Evaluation of the sensitivity of the distributed beam system is not

as straightforward, yet is still readily calculable using the chain rule, Equations 2.8 and

2.18, and substituting $k = \frac{k^*}{k_c}$

$$\frac{df}{dk} = \frac{df}{d(\alpha L)} \left(\frac{\frac{d\Gamma}{dk}}{\frac{d\Gamma}{d(\alpha L)}} \right) \quad (2.19)$$

The result of Equation 2.19 was solved by Turner and Wiehn [20] and shown to be

$$\begin{aligned} \frac{1}{f_0} \frac{df}{dk} &= (2(\alpha L)(\cos \alpha L \sinh \alpha L - \sin \alpha L \cosh \alpha L)) \\ &\times \left\{ 3(\alpha L)^2 (1 + \cos \alpha L \cosh \alpha L) + \right. \\ &\left. (\alpha L)^3 (\cos \alpha L \sinh \alpha L - \sin \alpha L \cosh \alpha L) + 2k(\sin \alpha L \sinh \alpha L) \right\}^{-1} \end{aligned} \quad (2.20)$$

A comparison of the sensitivity of both the point-mass model and distributed beam model are shown in Figure 2.7.

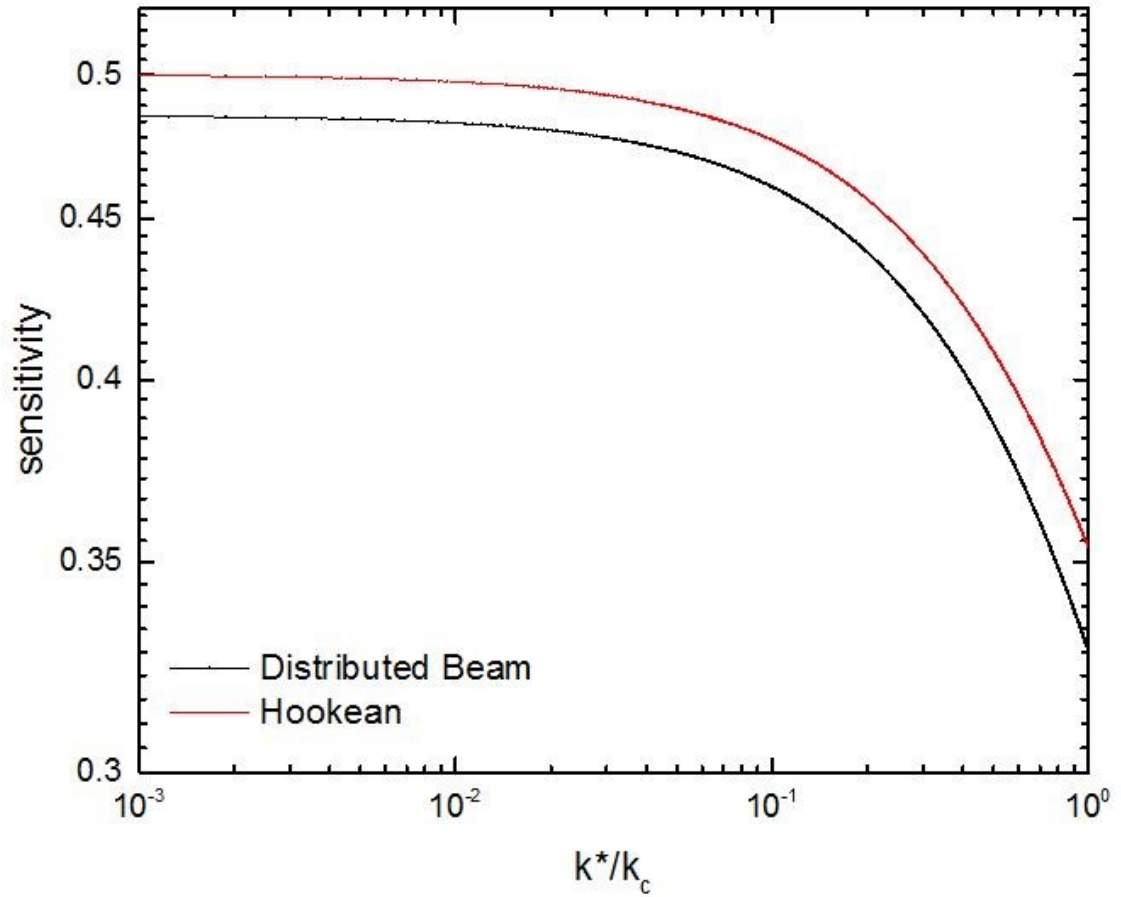


Figure 2.7. Predicted sensitivities of Distributed Beam and point-mass (Hookean) models. Reprinted from JE Hawk, MS Ghorashi, Arindam Phani, and Thomas Thundat, *Exploiting broader dynamic range in Si-bridge modified QTF's for sensitive thermometric applications*, Sensors and Actuators A: Physical, 279, 442-447 (2018).

Conclusion

With both models presented and compared, it readily becomes apparent that when the stiffness of the bridging element is much smaller than that of the QTF tines, as is routinely found when polymeric strands are employed, both models yield comparable results and the practitioner can employ either model; however, as the stiffness of the bridging element increases and becomes comparable to that of the QTF tines, the standard point-mass model fails to accurately predict stiffness changes and the practitioner should adopt the presented distributed beam model. In the next chapter, the experimental methodology will be discussed.

2.3. References

- 1- S. Boussaad and N.J. Tao, *Polymer wire chemical sensor using a microfabricated tuning fork*, NanoLetters, Vol 3 No 8 , 1173-1176 (2003).
- 2- M. Yun, S. Lee, C. Yim, N. Jung, T. Thundat, and S. Jeon, *Suspended polymer nanobridge on a quartz resonator*, Applied Physics Letters, 103, 053109 (2013).
- 3- J.A. Turner, S. Hirsekorn, U. Rabe, W. Arnold, *High-frequency response of atomic-force microscope cantilevers*, J Appl Phys, 82:966 (1997).
- 4- S.P. Timoshenko, *On the correction factor for shear of the differential equation for transverse vibrations of bars of uniform cross-section*, Philosophical Magazine, p. 744 (1921).
- 5- S.P. Timoshenko, *On the transverse vibrations of bars of uniform cross-section*, Philosophical Magazine, p. 125 (1922).
- 6- S.P. Timoshenko, *History of strength of materials*, McGraw-Hill New York (1953).
- 7- S.M. Han, H. Benaroya and T. Wei, *Dynamics of transversely vibrating beams using four engineering theories*, Journal of Sound and Vibration, 225(5), 935-988 (1999).
- 8- W.D. Means, *Hookean Behavior. In: Stress and Strain*. Springer, New York, NY (1976).
- 9- J. Melcher, J. Stirling, and G. Shaw, *A simple method for the determination of qPlus sensor spring constants*, Beilstein Journal of Nanotechnology, 6, 1733-1742 (2015)

- 10- F. J. Giessibl, *Forces and frequency shifts in atomic-resolution dynamic-force microscopy*, Physical Review B, Vol 56, number 24, 16010-16015 (1997)
- 11- Y. Lei, T. Murmu, M.I. Friswell, *Dynamic characteristics of damped viscoelastic nonlocal Euler-Bernoulli beams*, European Journal of Mechanics A/Solids, 42, 125-136 (2013)
- 12- E. Volterra, E.C. Zachmanoglou, *Dynamics of Vibrations*, Charles E. Merrill Books Inc, Columbus, Ohio, 1965.
- 13- W. Weaver, S.P. Timoshenko, D.H. Young, *Vibration Problems in Engineering*, John Wiley, New York (1990).
- 14- F.W. Stokey, *Vibration of Systems Having Distributed Mass and Elasticity*. In: *Harris CM, Crede CE (eds) Shock and Vibration Handbook*, McGraw-Hill, New York, Chapter 7 (1976).
- 15- T. Thundat, E.A. Wachter, S.L. Sharp, R.J. Warmack, *Detection of Mercury Vapor Using Resonating Microcantilevers*, Appl Phys Lett, 66, 1695 (1995)
- 16- M.J. Madou, *Fundamentals of Microfabrication: The Science of Miniaturization*, Second Edition, CRC Press, (1997).
- 17- G.Y. Chen, T. Thundat, E.A. Wachter, and R.J. Warmack, *Adsorption-Induced Surface Stress and Its Effects on Resonance Frequency of Cantilevers*, J. Appl. Phys., vol. 77, pp. 3618-3622, (1995).
- 18- K. Yamanaka and S. Nakano, *Ultrasonic atomic force microscope with overtone excitation*, Jpn J Appl Phys, 35, 3787 (1996).

- 19- U. Rabe, K. Janser, and W. Arnold, *Vibrations of free and surface-coupled atomic force microscope cantilevers: Theory and experiment*, Rev Sci Instr 67, 3281 (1996).
- 20- J.A. Turner and J.S. Wiehn, *Sensitivity of flexural and torsional vibration modes of atomic force microscope cantilevers to surface stiffness variations*, Nanotechnology 12, 322 (2001).

Chapter 3: Experimental Method

3.1. QTF Platform

In order to examine the bolometric response of a modified quartz tuning fork system, two different systems were tested. Work initially began with the off-the-shelf Akiyama Probe. As was briefly discussed in Chapter 1, the Akiyama probe platform was developed in 2003 as a novel means to conduct AFM operations in a fully electronic, self-sensing, and self-actuating mode [1] while eliminating the optical beam alignment of standard CL based AFM systems and simplifying AFM operations [2]. However, this system proved too difficult to model and allow for a means to determine the underlying cause for any response of the system to optical stimuli. Indeed, FEM analysis was required to simply illustrate the motion of the terminally attached structure. [3]. Initial tests had confirmed, and the Akiyama probe user manual states, that thermal variation will cause a shift in the resonance response of the system.

Given that the goal for discussion in this work was whether the modified QTF system could be used to monitor optically mediated thermal responses, and further for the monitoring of airborne chemical analytes, it was of absolute necessity that a model for thermally mediated changes be investigated. Indeed, as was shown by Datskos et al. [4], photogeneration of free charge carriers could cause a change in the net stress of the silicon attachment: yet, as they observed, this photoinduced stress would be in the opposite direction and up to four times larger than thermal excitation alone when a

silicon sensing element is used. To allow for simplified modelling of the modified QTF to thermally mediated variations, a new system was assembled.

To realize this new platform, quartz tuning forks, $f_0 = 40\text{kHz}$, were obtained from Digikey Canada and subsequently removed from their canister casing, see Figure 3.1, to allow attachment of a rectangular silicon bridge using cyanoacrylate adhesive. The QTF dimensions were $3\text{mm} \times 250\mu\text{m} \times 250\mu\text{m}$ in length, width, and thickness respectively. The spring constant of the tuning fork was obtained using $k_c = 3EI/L^3 = 2842\text{N/m}$ with the Young's modulus of quartz taken as 78.6 GPa [5].



Figure 3.1. Typical 40 kHz QTF as used in this study.

The silicon bridging structures chosen were Arrow TL-2 microcantilevers (Nanoworld), shown in Figure 3.2, $500\mu\text{m} \times 100\mu\text{m} \times 1\mu\text{m}$ in length, width, and

thickness respectively. One lever was manually affixed to the apex of the QTF tines, as seen in Figure 3.3, using cyanoacrylate adhesive. Since the spacing between the tines is $250\mu\text{m}$, this is taken as the effective length of the clamped-clamped bridging structure.

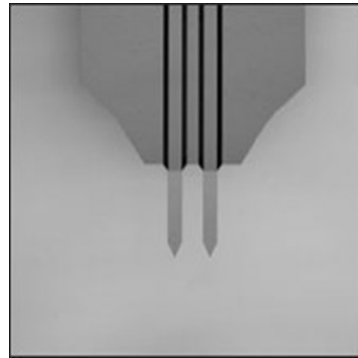


Figure 3.2. NanoWorld Arrow™ TL2 levers used in this study.

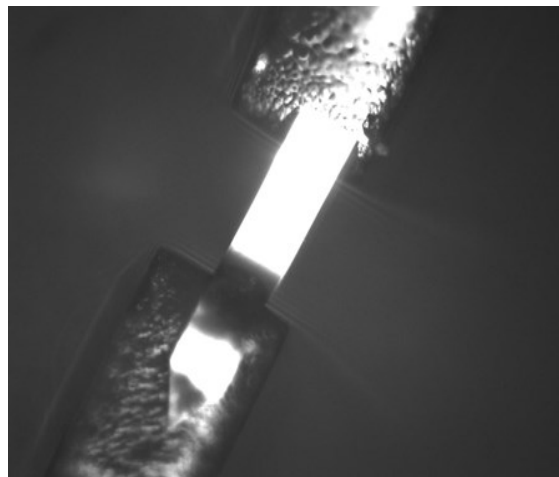


Figure 3.3. Typical silicon bridged QTF as used in this study.

The new silicon bridge modified QTF's resonance response was tested using an Agilent 4294A precision impedance analyzer and the data was recorded using a custom LabVIEW program coded by the author. Figure 3.4 demonstrates the response of an

unmodified QTF removed from its container, as well as a modified QTF. In this figure, the ordinate axis is displayed in units of conductance, ie the quotient of current and voltage. This is instructive in that it monitors the magnitude of the current which passes through the oscillator circuit which, at both electrical and mechanical resonance, is maximized. The quality factor of the modified QTF was determined to be ≈ 500 , indicating good energy storage to loss ratio, while the quality factor of the unmodified, “out-of-the-can”, QTF is on the order of 10^3 . Both of these values are smaller than an “in-the-can” QTF due to losses incurred due to air damping, for the “out-of-can” QTF, and air damping and reduced oscillation amplitude of the modified QTF.

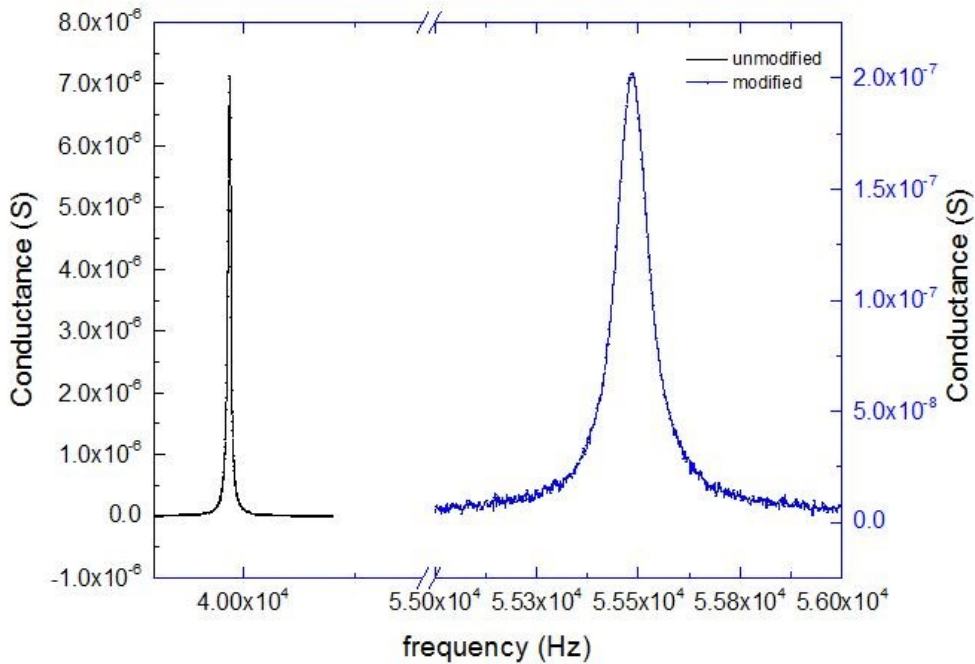


Figure 3.4. 4294A Impedance analyzer response of a QTF removed from its canister (Left) and modified with a silicon bridge (Right).

After attachment of the bridging element, the silicon bridge modified QTF was electrically excited into resonance and the bridging element was monitored using a Polytec MSA-500 Laser Doppler Vibrometer (LDV) to determine the motion of the bridge. As was noted in Chapter 1 with the discussion of thin polymer strands, the QTF can excite the affixed structure axially, i.e. in the direction of the polymer length and in the same direction as the tines' motion, or in a transverse direction, i.e. the tines oscillate in and out and the bridge structure moves up and down. The motional direction of the silicon bridging element was observed to be in the transverse direction as shown in Figure 3.5.

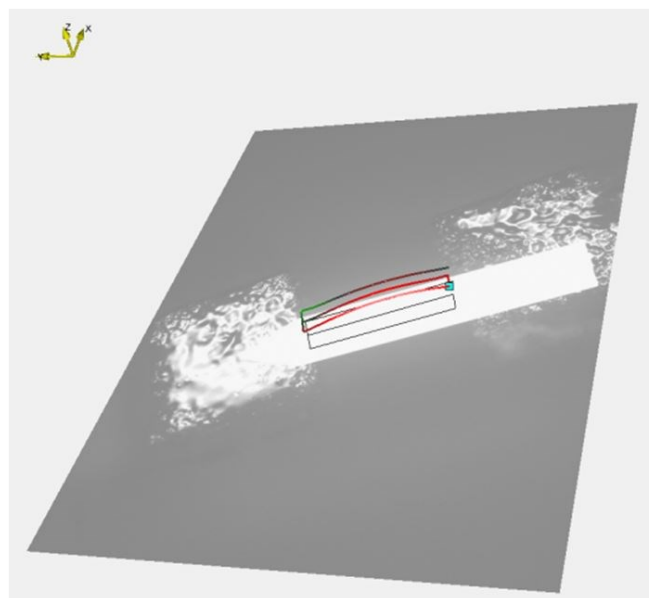


Figure 3.5. Polytec MSA-500 Laser Doppler Vibrometer image of the motion of the silicon bridging structure.

The motion of one of the tines of the QTF was also monitored with the LDV to determine if the mathematical model detailed in Chapter 2 is applicable, see Figure 3.6.

It was observed that the tine's motion did respond in the manner predicted by the presented clamped-spring coupled beam model.

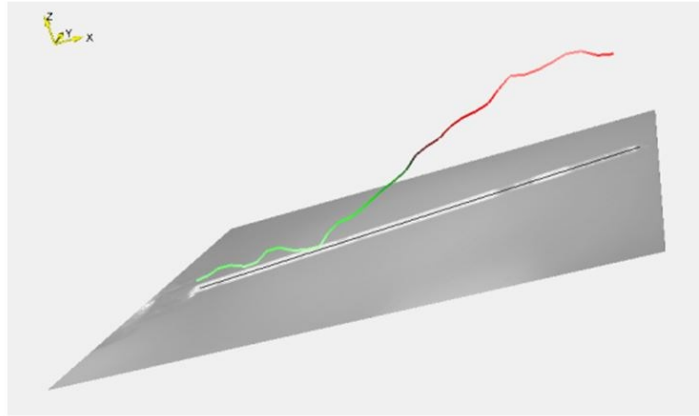


Figure 3.6. Motion of a silicon bridge modified QTF using a Polytec MSA-500 Laser Doppler Vibrometer.

3.2. Self-Sensing and Self-Actuating Electronics

Closed loop actuation of both the Akiyama probe and silicon bridge modified QTF was accomplished using a Tuning Fork Sensor Controller (TFSC), shown in Figure 3.7, which was purchased from NanoAndMore USA. The QTFs of both the Akiyama probe and custom silicon bridge modified QTF were driven at their fundamental frequency by the TFSC which operates in a feedback mode configuration, i.e. the output of the driven QTF was amplified and reintroduced to the QTF as an input. The QTFs were mounted onto the accompanying TFSC holder which has a variable potentiometer to allow for cancelling of any stray capacitance with the QTF, and allows for direct measurement of the motional arm of the fork, shown in Figure 3.8.



Figure 3.7. Tuning Fork Sensor Controller (TFSC) used in this study.

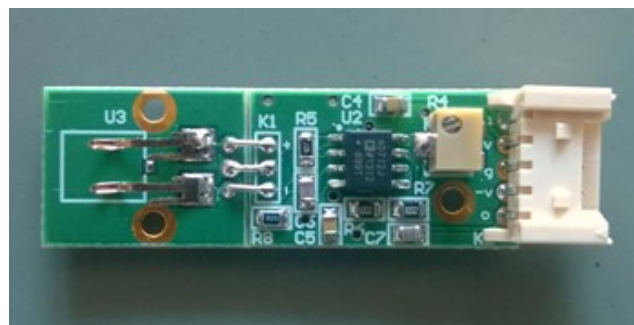


Figure 3.8. Tuning Fork Sensor Controller holder with preamplifier and variable potentiometer.

As the TFSC controller holder is designed for use with Akiyama probes, which are affixed to a ceramic plate, it was necessary to modify the system to allow for the proper interfacing of the silicon bridge modified QTF. This was accomplished by salvaging a ceramic chip from a broken Akiyama Probe, and soldering a piece of a dual inline package Integrated circuit (DIP IC) socket onto it, see Figure 3.9.

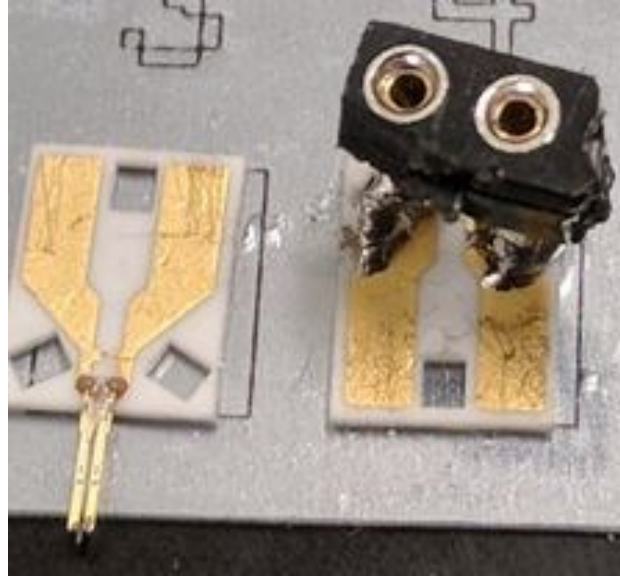


Figure 3.9. Akiyama probe (Left) and custom fabricated QTF mount (Right).

The output signal of the QTF was split into an Agilent 53230A universal frequency counter which sampled the signal at 10 *MHz* and was read using custom LabVIEW software, written by the author, allowing data acquisition at 1 *mHz*. The QTF was placed into a sealed custom holder, fabricated by the author, to allow for environmental control and was maintained at atmospheric pressure during the course of this study. A schematic of the experimental arrangement is shown in Figure 3.10.

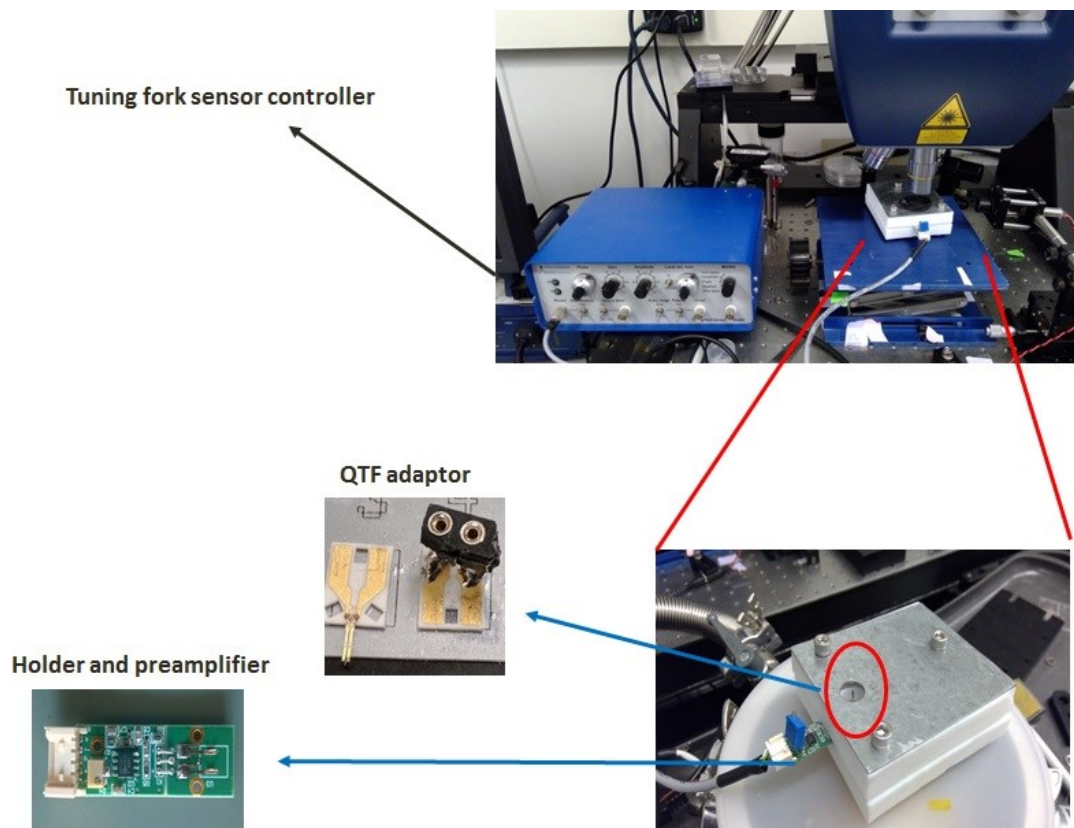


Figure 3.10. Experimental arrangement.

The custom flow cell was constructed using a Polytetrafluoroethylene (PTFE), a.k.a. Teflon, block. As shown in Figure 3.11, the cell was constructed in 2 halves to allow passage of the TFSC holder through the cell wall terminating in the central cylindrical chamber which had 2 conduits for vapor flow into and out of the cell. The primary chamber was sealed using a Zinc Selenide optical window, for IR based studies, to seal the interrogation chamber. All elements of the cell were fitted with Viton gaskets to make a leak-proof test chamber.

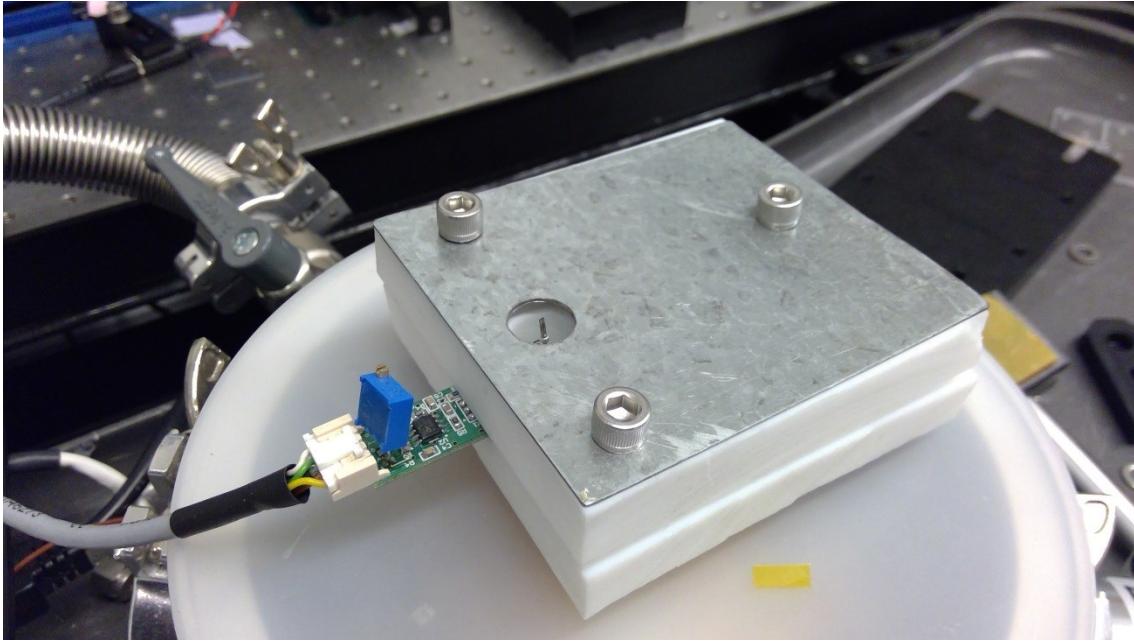


Figure 3.11. Teflon flow cell comprised of two 1/2 inch blocks sandwiched together with a 3/4 inch primary chamber (visible from top) fed through 1/8 inch inlet and outlet ports on the bottom (not visible).

Conclusion

In Chapter 3, all necessary information to reproduce the experimental setup was detailed. In Chapter 4, all of the pieces discussed thus far will be brought to bear allowing for optimization of silicon bridge modified QTFs for the detection of optically mediated thermal variance.

3.3. References

- 1- T. Akiyama, U. Staufer, and N.F.de Rooij, *Self-sensing and self-actuating probe based on quartz tuning fork combined with microfabricated cantilever for dynamic mode atomic force microscopy*, Applied Surface Science, 210 (2003) 18-21
- 2- S. Stucklin, M.R. Gullo, T. Akiyama, M. Schneidiger, *Atomic Force Microscopy for Industry with the Akiyama-Probe System*, International Conference on Nanoscience and nanotechnology (ICONN), (2008)
- 3- T. Akiyama, U. Staufer, and N.F. Rooij, *Symmetrically arranged quartz tuning fork with soft cantilever for intermittent contact mode atomic force microscopy*, Review of Scientific Instruments, Vol 74, No 1, 112-117 (2003)
- 4- P. Datskos, S. Rajic, and I. Datskou, *Photoinduced and thermal stress in silicon microcantilevers*, Applied Physics Letters, Vol 73, No 16, 2319-2321, (1998)
- 5- J. Melcher, J. Stirling, and G. Shaw, *A simple method for the determination of qPlus sensor spring constants*, Beilstein Journal of Nanotechnology, 6, 1733-1742 (2015)

Chapter 4: Response to HeNe laser

While the preceding chapters laid the necessary foundation for the successful implementation of this silicon bridge modified QTF system, Chapter 4 will proceed to put all of the pieces together to validate the mathematical model and demonstrate the system's ability to respond to optical signals while testing multiple devices.

4.1. Optically mediated response: methodology

Prior to investigation of bolometric applications of the silicon bridge modified QTF device, it is first necessary to evaluate the reliability of the theoretical derivations given previously in Chapter 2. Initially, the measured frequency changes are inserted into the dispersion relation, i.e. Equation 2.8, which is then solved for the dimensionless wavenumber (αL)

$$\alpha L = (\alpha_{1,free} L) \sqrt{\frac{f}{f_{1,free}}}. \quad (4.1)$$

Once the wavenumber of interest is found, it is used to calculate the total change in spring constant of the bridging element which can be calculated by rearranging Equation 2.18 to the form

$$k^* = \frac{k_c (\alpha L)^3}{3} \frac{(1 + \cos \alpha L \cosh \alpha L)}{(\sinh \alpha L \cos \alpha L - \sin \alpha L \cosh \alpha L)} \quad (4.2)$$

Whereas the silicon bridging element takes the form of a clamped-clamped bridging structure, it becomes necessary determine how the spring constant changes as a function

of stress. This stressed condition has been previously solved for a clamped-clamped structure, and textbooks provide the solution [1]:

$$k_{with-stress} = \frac{4N}{\frac{L}{2} - 2 \left(\frac{\cosh(\frac{k_0 L}{2}) - 1}{k_0 \sinh(\frac{k_0 L}{2})} \right)} \quad (4.3)$$

where W is the beam width, t is the beam thickness, L is the beam length, $k_0 = \sqrt{12N/EWt}$, and $N = \sigma_0 Wt$. As σ_0 is the total internal stress of the bridging element, it can be expanded to the form: $\sigma_0 = \sigma_{compressive} + \sigma_{thermal} + \sigma_{photo-induced}$. A net compressive stress of the bridge is incurred upon attachment of the bridging element to the QTF structure and does not change, thus all changes of stress within the bridge are either due to photo-induced or thermally mediated changes.

The contribution from thermal stress is given by:

$$d\sigma_{thermal} = \alpha_{Si}(T)E_{Si}(T)dT \quad (4.4)$$

where α_{Si} and E_{Si} are the thermal expansion coefficient and Young's modulus of silicon respectively, and T is the temperature. The temperature dependent thermal expansion coefficient, $\alpha_{Si}(T)$, as given by Watanabe et al. [2], and Young's modulus as a function of temperature, $E_{Si}(T)$, as given by Cho [3], were used in the calculations.

Any contribution due to photo-induced stress, is given as [4,5]:

$$\sigma_{photo-induced} = \left(\frac{1}{3} \frac{d\varepsilon_g}{dP} \Delta n \right) E \quad (4.5)$$

where ε_g is the material's bandgap, $\frac{d\varepsilon_g}{dP}$ is the pressure dependence of the energy bandgap, Δn is the photo-induced excess charge carriers, and E is the Young's modulus. The pressure dependence of the energy bandgap is material dependent, and has been found to be $\frac{d\varepsilon_g}{dP} = -2.9 \times 10^{-24} \text{ cm}^3$ for Silicon [6]. The negative value of $\frac{d\varepsilon_g}{dP}$ indicates that the photo-induced stress is compressive, acting in an opposite direction to the thermal stress.

4.2. Thermal Response test

In order to determine the response of the bridging element to thermal stress, the silicon bridge modified QTF was exposed to preheated compressed air in 2 °C increments and the change in spring constant of the silicon bridging element was calculated. To this end, the experimental configuration was modified such that compressed air was metered using two Atovac mass flow controllers which maintained a constant 100 sccm flow rate. The mass flow controllers were each connected in parallel to the test cell using 1/8 inch Teflon tubing. One conduit was directed into a water bath that was regulated at a constant temperature prior to entry into the test cell, and the other conduit was connected directly to the test cell. A model of the experimental arrangement is shown in Figure 4.1. The temperature inside the test cell was continuously monitored via a K-type thermocouple. Due to the dramatically lower

thermal mass of the bridging element relative to the QTF, the changes in measured frequency upon introduction of heated air to the cell were attributed to heating of the bridging element solely.

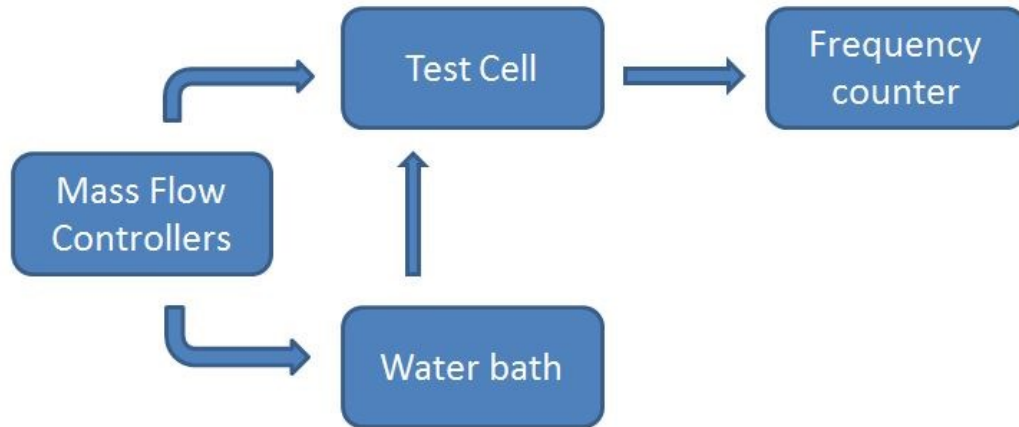


Figure 4.1. Schematic of configuration for experimental verification of silicon bridge modified QTF thermal response.

To evaluate the net change of spring constant for various temperatures, Equations 4.1-4.4 were combined and were solved for a variety of temperatures. The theoretical values are plotted alongside the experimentally obtained values in Figure 4.2. The comparison of experimental and theoretical thermal responses is in very close agreement, thus giving credence to the theoretical model for the determination of temperature of the bridging element.

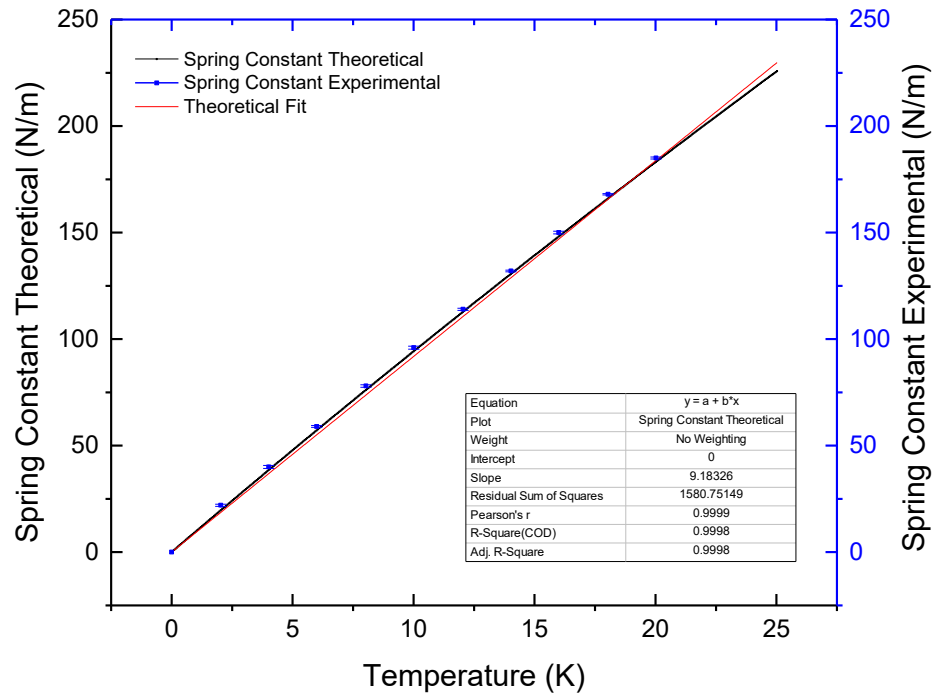


Figure 4.2. Comparison of theoretical (black) and experimental (blue) thermal response of the modified QTF. Reprinted from JE Hawk, MS Ghoraishi, Arindam Phani, and Thomas Thundat, *Exploiting broader dynamic range in Si-bridge modified QTF's for sensitive thermometric applications*, Sensors and Actuators A: Physical, 279, 442-447 (2018).

4.3. Bolometric applications

As an initial proof of concept for the detection of optical signals, the response of Akiyama probes to HeNe laser light emitted from the LDV were tested by directing the beam to the surface normal; however, as there is no model available to describe the processes, the signal response merely indicates that the technique is viable, see Figure 4.3, and the custom modified silicon bridge modified QTFs, with a viable model, were studied.

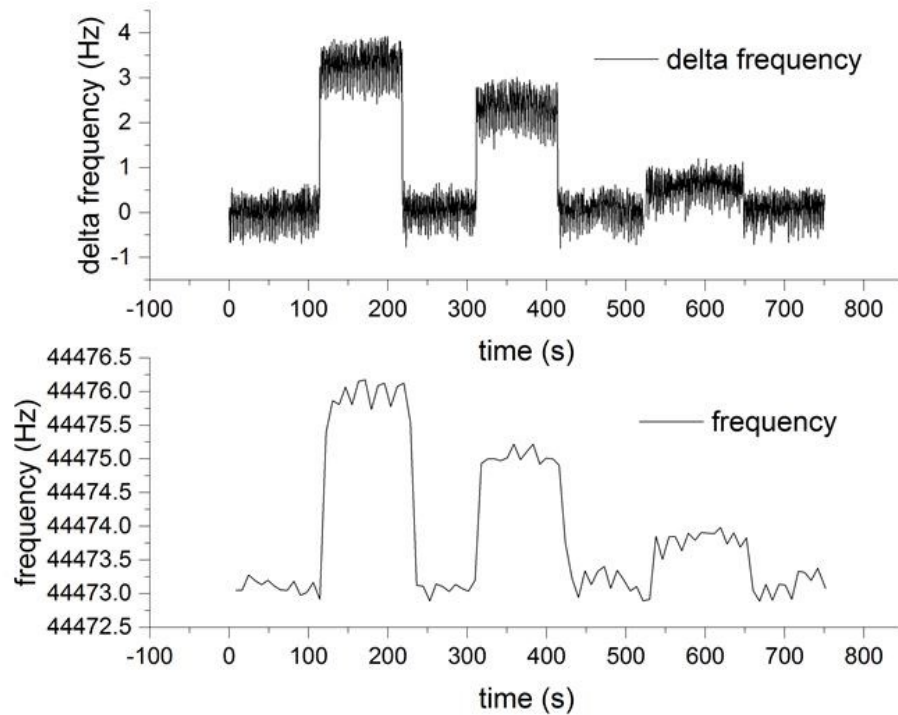


Figure 4.3 Response of an Akiyama probe to HeNe laser light to 332 μW , 219 μW , and 144 μW incident power. (top) raw output from the TFSC (bottom) confirming data acquired using the laser Doppler vibrometer.

In order to demonstrate the applicability of fixed silicon bridge modified QTFs for bolometric sensing applications, the silicon bridge sensing element was illuminated using a HeNe laser. The HeNe laser utilized for this is incorporated into a Polytec MSA-500 Laser Doppler Vibrometer (LDV), and its output can be attenuated via internal neutral density filters. The laser power output for each filter setting was measured using an International Light Technologies (ILT) 1700 Research Radiometer connected to an SED100 detector, and the magnitude of power that would be absorbed by the silicon bridging element was calculated using Fresnel's equation for normal incidence

$$T = 1 - R = 1 - \left| \frac{n_1 - n_2}{n_1 + n_2} \right|^2 \quad (4.6)$$

where T is the transmitted component, R is the reflected component, and n_1 and n_2 are the refractive indices of the two media at the interface. With knowledge of the power transmitted into the silicon bridge, Beer-Lambert's equation was used to determine the power absorbed by the silicon bridge.

$$P_{Trans} = P_{Incident} e^{-\alpha t} \quad (4.7)$$

Where P_{Trans} is the component transmitted through the body, $P_{Incident}$ is the component incident on the body, α is the attenuation coefficient (m^{-1}), and t is the thickness. It should be noted the transmitted component, T, from Equation 4.6 is equivalent to the incident component, $P_{Incident}$, in Equation 4.7. Allowing for five successive reflections, the power absorbed by the silicon bridge was thus calculated. Both the measured power output and the calculated absorbed power are shown in Table 4.1. It should be noted

that, for the silicon bridge thickness used herein, the absorbed power is approximately 24% of the incident power. The remaining 76% of the power is either reflected from the incident surface, or transmitted completely through the bridge.

Table 4.1. Measured power output and absorbed power from the LDV HeNe laser for all internal filters.

	Incident Power	Absorbed Power
P₀	332 μW	78.2 μW
P₁	219 μW	51.9 μW
P₂	144 μW	34.1 μW
P₃	95 μW	23 μW
P₄	63 μW	13 μW
P₅	42 μW	9.9 μW
P₆	27 μW	6.4 μW
P₇	18 μW	4.3 μW

The silicon bridge modified QTF was arranged in the configuration shown in Figure 3.10. In order to prevent any attenuation of the light incident upon the device, the top of the test cell was left open to atmosphere rather than sealed. Although it is well known that any turbulent air flow across the sensing element can, and will, lead to erroneous results due to forced cooling of the sensing element, this deleterious effect was mitigated by the cell design which allowed the silicon bridge modified QTF to be seated

in a recessed position within the test chamber. This was hoped to allow the cell to be open to the atmosphere, yet remain somewhat stable during the course of experimentation; however, initial results proved this to be untenable and necessitated the use of alternate means to seal the test chamber.

The incident laser beam was allowed to fall completely upon the center of the silicon bridge and the QTF's frequency was recorded for eight different absorbed power levels ranging from $78\mu W$ down to $4\mu W$. The HeNe beam spot was observed to have an approximate diameter of $25\mu m$. While it is known that the photo-induced stress will be of a compressive nature, the HeNe beam spot size was less than 2% of the entire silicon beam area, thus it was initially assumed to be negligible.

4.3.1. 40 kHz QTFs

The initial device tested was constructed using a base frequency 40 kHz QTF which, upon attachment of the silicon bridging element, resulted in an increase of operational frequency to 55.8 kHz. The spring constant of the bridging structure was approximately 3100 N/m. As the spring constant of the QTF tines was approximately 2840 N/m, the ratio of k^*/k_c is greater than one, thus obviating the need of the distributed beam model. This platform was tested with an open cell to light from the HeNe laser and repeated 4 times. Figure 4.4 shows representative results for the set of tests clearly demonstrating baseline drift caused by external airflow across the system.

The plots in Figure 4.4 show the raw frequency data acquired, the change in spring constant calculated using Equation 4.2, and the temperature change of the bridge element required to facilitate the change in spring constant using Equation 4.3.

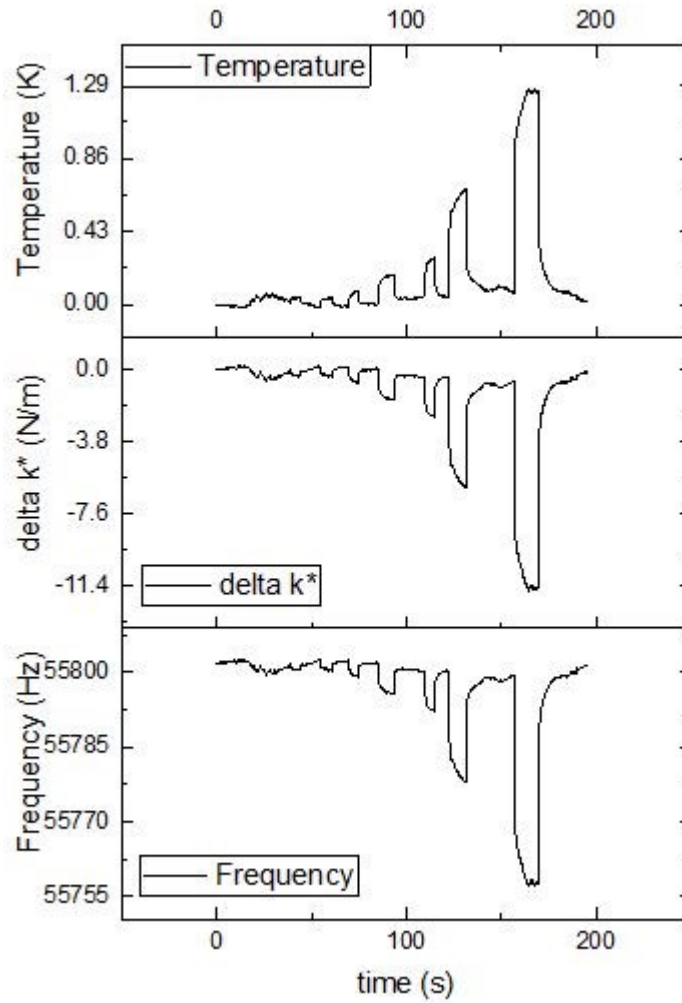


Figure 4.4. Device tested while open to atmosphere, yet recessed in flow cell.

Power levels are (right to left): $78.2 \mu W$, $51.9 \mu W$, $34.1 \mu W$, $23 \mu W$, $13 \mu W$, $9.9 \mu W$, $6.4 \mu W$, and $4.3 \mu W$.

The maximum temperature increase for the highest laser power absorption, $78.2 \mu W$, is shown in Figure 4.5 where it can be observed that the temperature value decreases with each subsequent test. This observation, along with the variation in the base frequency value can possibly be explained by accounting for some fraction of the thermal rise for each pulse to be stored in the thermal capacitance of the attachment medium, cyanoacrylate adhesive, and small changes in the anchoring point due to cracking or separation.

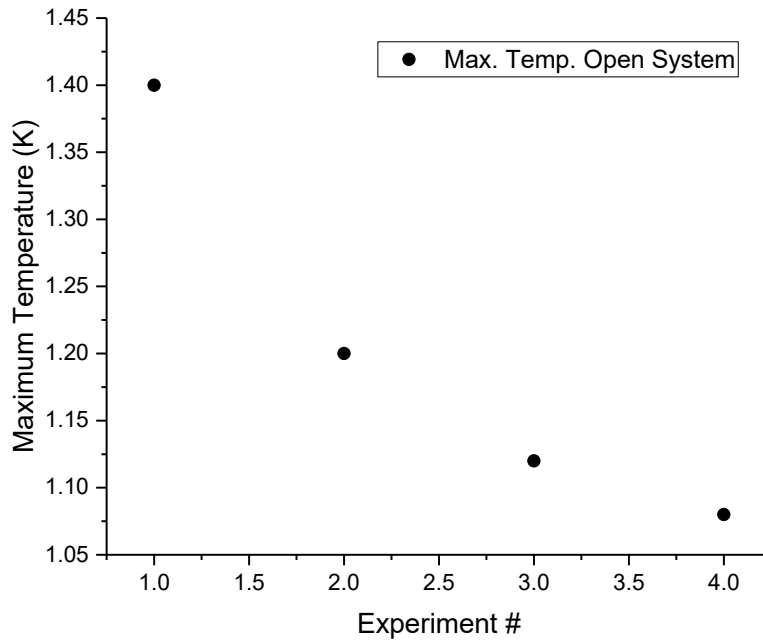


Figure 4.5. Maximum temperature rise for $78.2 \mu W$ absorbed power for the four different open cell tests.

In order to mitigate the baseline frequency fluctuations observed in the previous tests, a quartz microscope slide coverslip was installed to seal the test cell. As the

refractive index of quartz at this frequency is 1.45, only 3% of the incident light is reflected off the surface, thus the incident power impinging onto the silicon bridge was assumed the same as previously calculated. The results are presented in Figure 4.6.

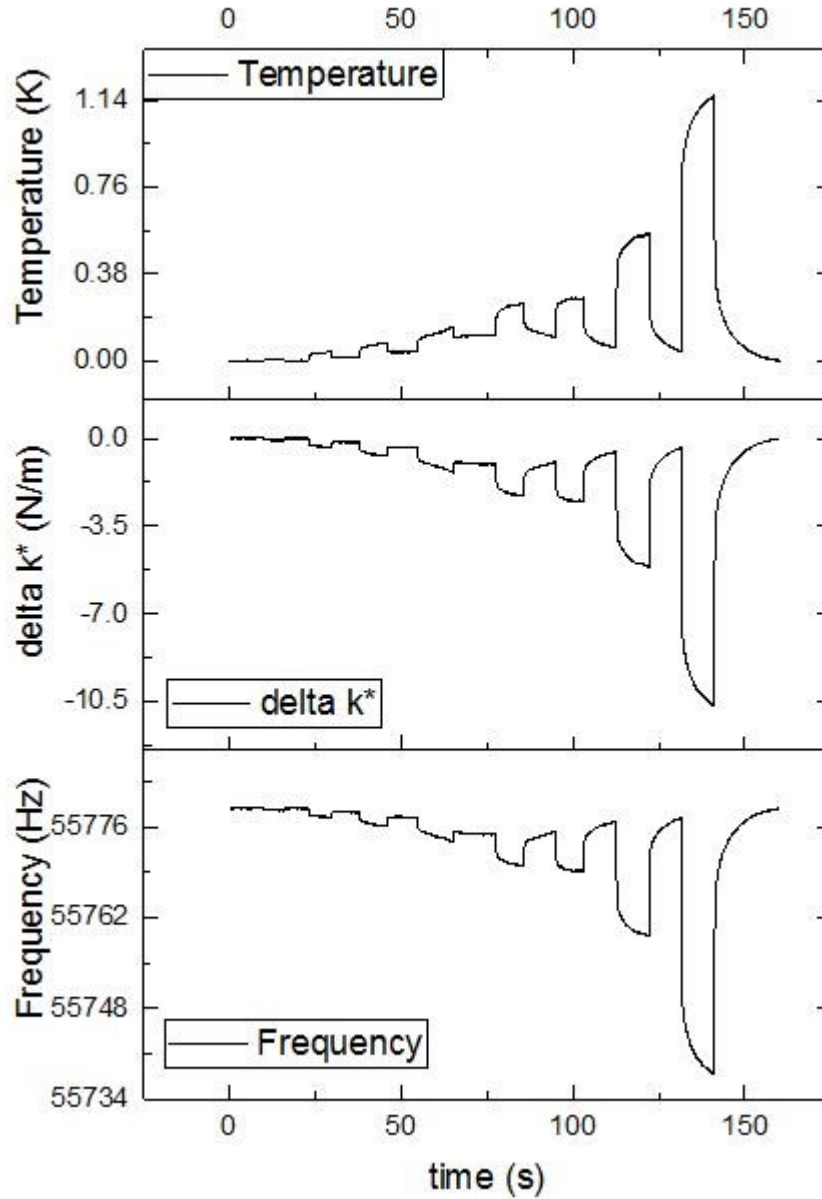


Figure 4.6. Experiment #1, Device tested with Quartz coverslip. Power levels are (right to left): $78.2 \mu W$, $51.9 \mu W$, $34.1 \mu W$, $23 \mu W$, $13 \mu W$, $9.9 \mu W$, $6.4 \mu W$, and $4.3 \mu W$.

The maximum temperature increase for the highest laser power absorption, $78.2 \mu W$, is shown in Figure 4.7 bearing the same hallmark as the open cell arrangement in that there exists a thermal storage in the anchoring material; however, larger deleterious fluctuations were mitigated.

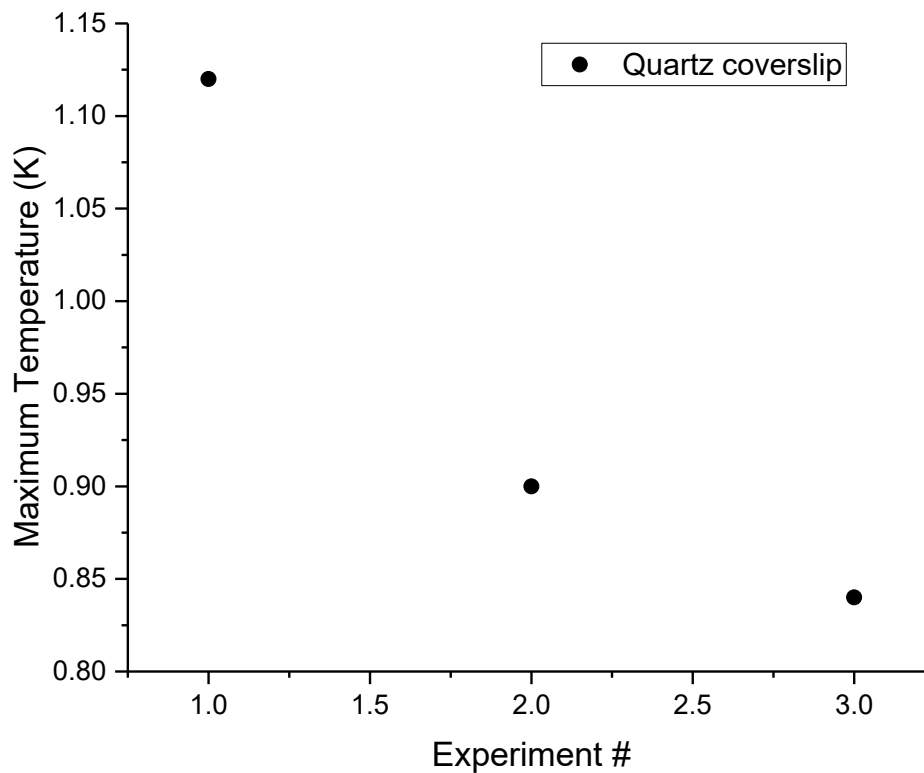


Figure 4.7. Maximum temperature rise for $78.2 \mu W$ absorbed power for three different quartz coverslip covered cell tests.

4.3.2. 32768 Hz QTFs

As is obvious from Equation 4.1 and Equation 4.2, for a given change in spring constant, the magnitude of the change in frequency is inversely proportional to the base frequency of the QTF used, or stated another way, higher base frequencies allow for monitoring smaller changes in spring constant of the bridging element. Thus, alternate platforms were fabricated using base frequency 32768 Hz QTFs with dimensions of 450mm in length, $250\mu\text{m}$ in width, and $600\mu\text{m}$ in thickness with a net spring constant of 11.6 kN/m . The silicon bridges were again affixed to the terminal end of the QTFs using cyanoacrylate adhesive, and as the distance between the tines is $250\mu\text{m}$, the silicon bridging element had a spring constant of approximately 3200 N/m though there is variability between devices as some may have either more or less intrinsic compressive stress incurred upon attachment of the bridging element.

One of the devices tested was sealed with a quartz coverslip in one series of experiments, and using a glass coverslip in another. Each set was run three times with representative results using the quartz coverslip are shown in Figure 4.8, and representative results using the glass coverslip shown in Figure 4.9.

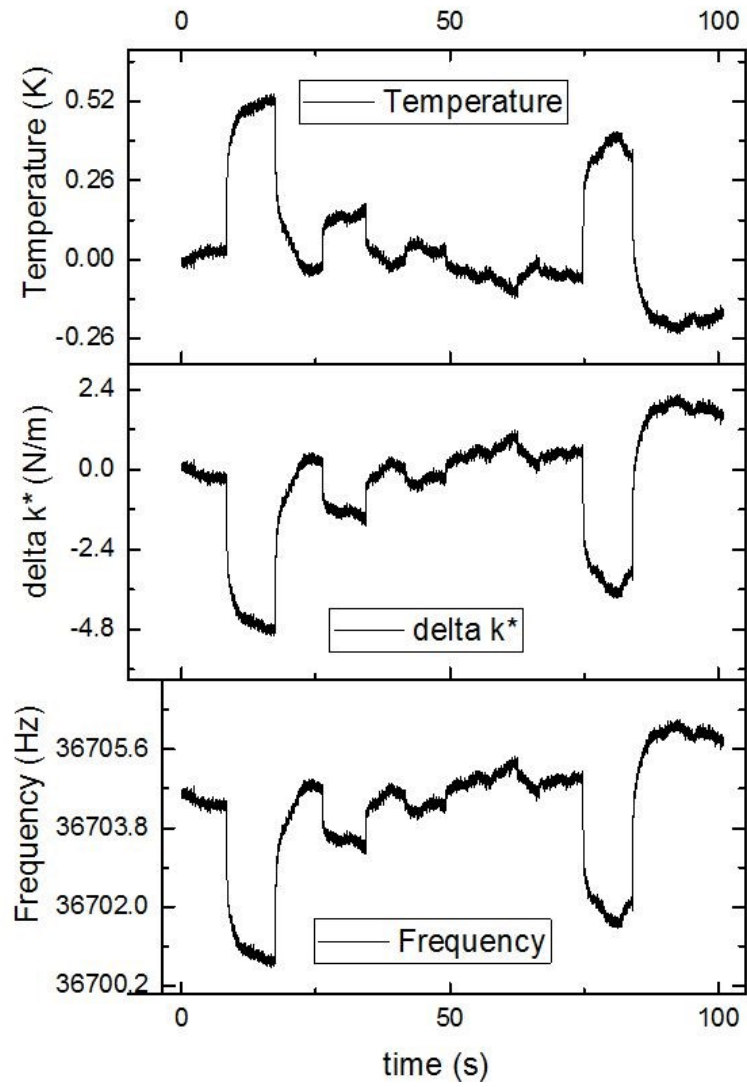


Figure 4.8. Quartz coverslip - Experiment #2 - 32768 base frequency QTF tested with HeNe laser powers of (left to right): $78.2 \mu W$, $51.9 \mu W$, $34.1 \mu W$, $23 \mu W$, and $78.2 \mu W$.

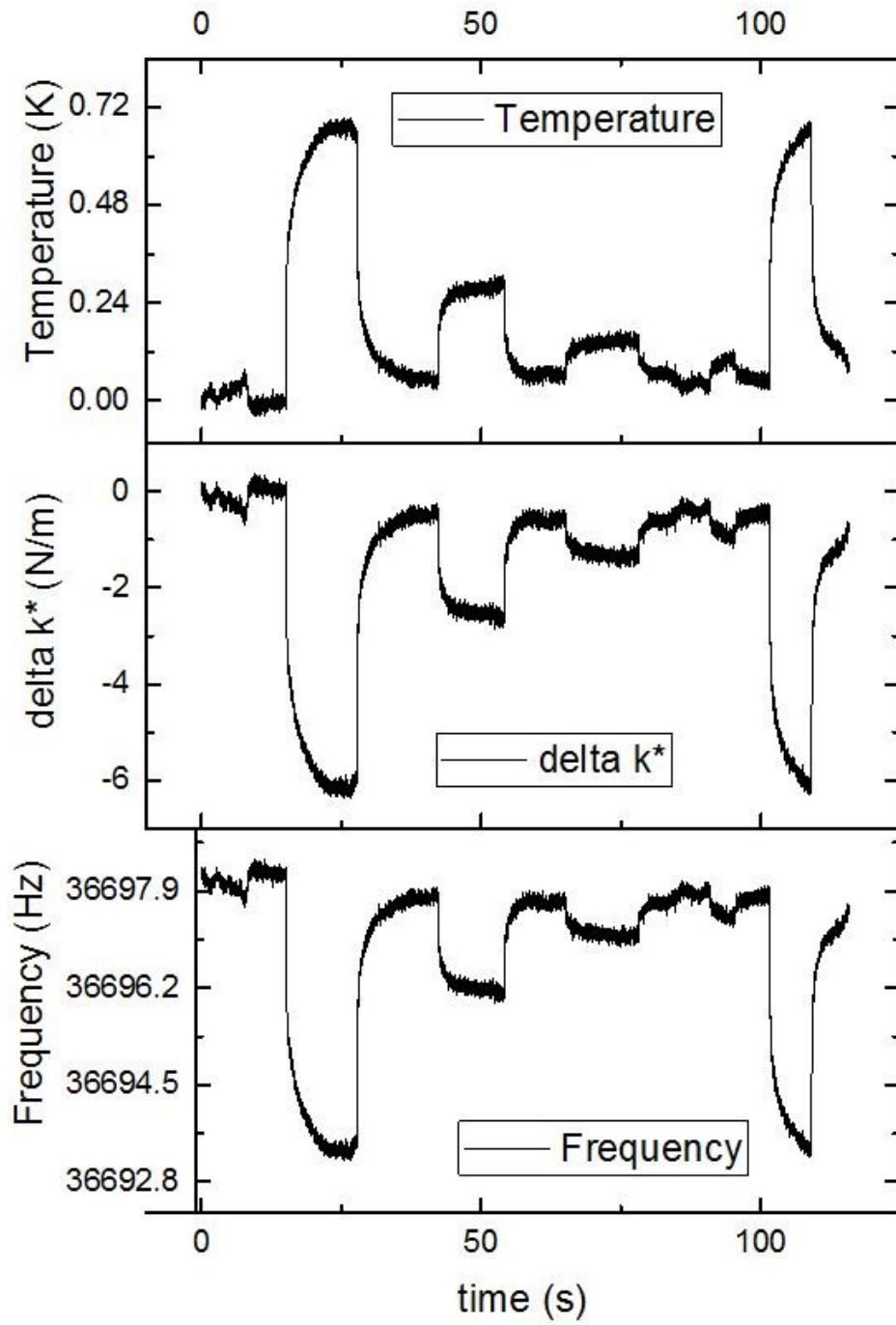


Figure 4.9. Glass coverslip - Experiment #1 - 32768 base frequency QTF tested with HeNe laser powers of (left to right): $78.2 \mu W$, $51.9 \mu W$, $34.1 \mu W$, $23 \mu W$, and $78.2 \mu W$.

The decreased magnitude of the maximum heating is still observed. Also notable is the larger response obtained using the glass coverslip over that obtained using the quartz coverslip. Given that the quartz coverslip is thicker than the glass coverslip, this is readily understandable as the optical power incident upon the silicon bridging element will be more greatly attenuated traversing through the thicker quartz coverslip. Nonetheless, the salient point is the observation that the maximum frequency shift in both cases is less than 5 Hz, thus greatly limiting the responsivity of the device. Due to this, further tests with this device were discontinued.

An alternate 32768 Hz fork of the same dimensions was also modified and tested using a glass coverslip with results shown in Figure 4.10. This device performed slightly better than the previous example, however this device was also unresponsive to lower incident light power levels and only exhibited a 10 Hz frequency shift for maximum power absorption. Testing with this platform was also discontinued.

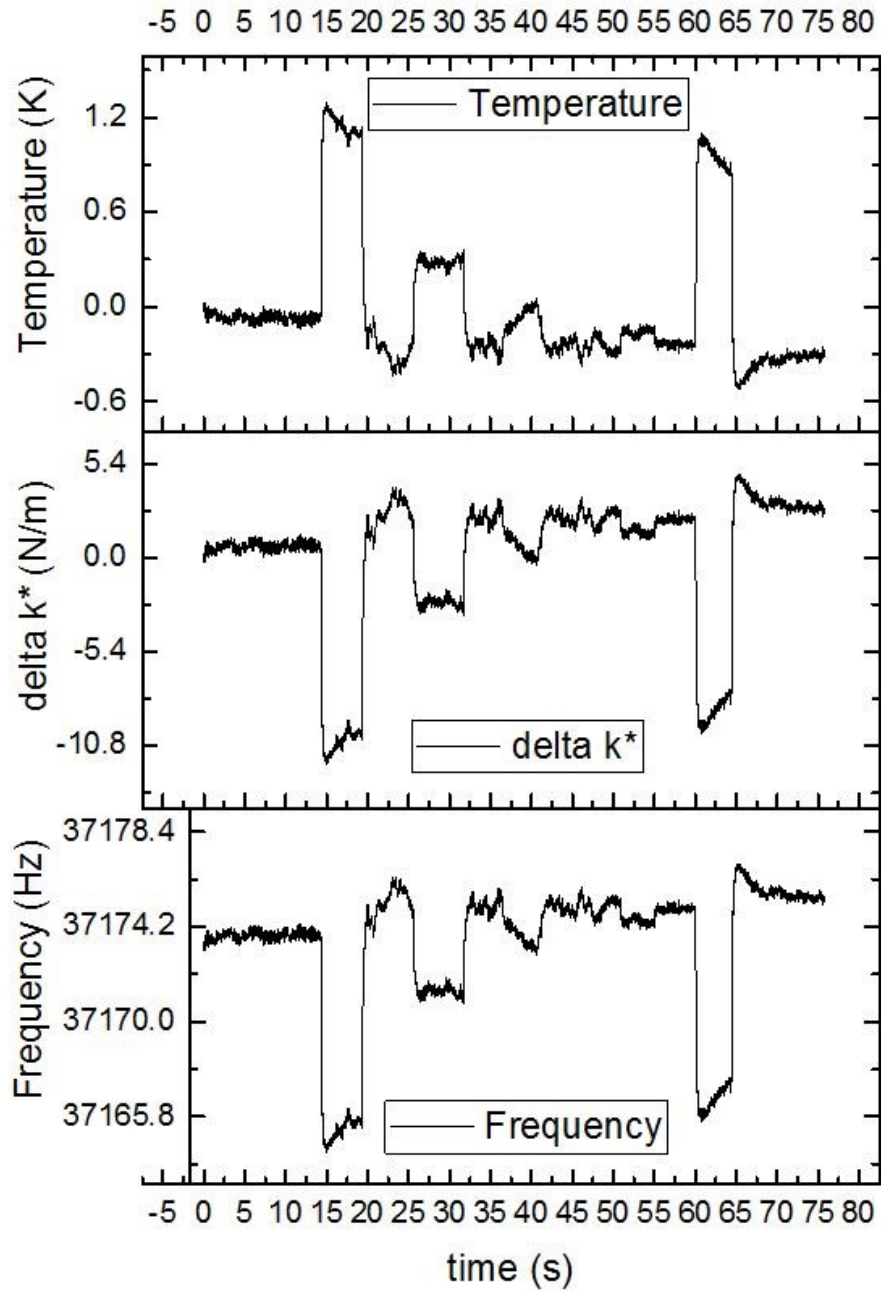


Figure 4.10. Glass coverslip - Experiment #1 - 32768 base frequency QTF tested with HeNe laser powers of (left to right): 78.2 μW , 51.9 μW , 34.1 μW , 23 μW , and 78.2 μW .

4.3.3. Results for Optimized Conditions - 40 kHz QTF

Exploiting the lessons learned with the previously discussed tests, a final 40 kHz base frequency QTF was tested in two final configurations using a glass coverslip to mitigate environmentally induced fluctuations, and the overhead lights were also in either an on, or off, condition. The results with the glass coverslip and lights ON are shown in Figure 4.11 with the maximum temperature attained shown in Figure 4.12. The results with the glass coverslip and lights OFF are shown in Figure 4.13, with the maximum temperature attained shown in Figure 4.14. It appears that the lights, in the “ON” position play a small role in the response of the device. The greater stability exhibited in this series of experiments demonstrates the optimization of the experimental configuration over those conducted previously. As has been mentioned previously, each consecutive test of the device thermally loads the cyanoacrylate adhesive thus reducing the responsivity of each subsequent test; thus the final test was used to calculate the lower limits of the system and is displayed in Figure 4.15, with the lowest incident power, from 4 to 6 seconds, zoomed in and shown in Figure 4.16.

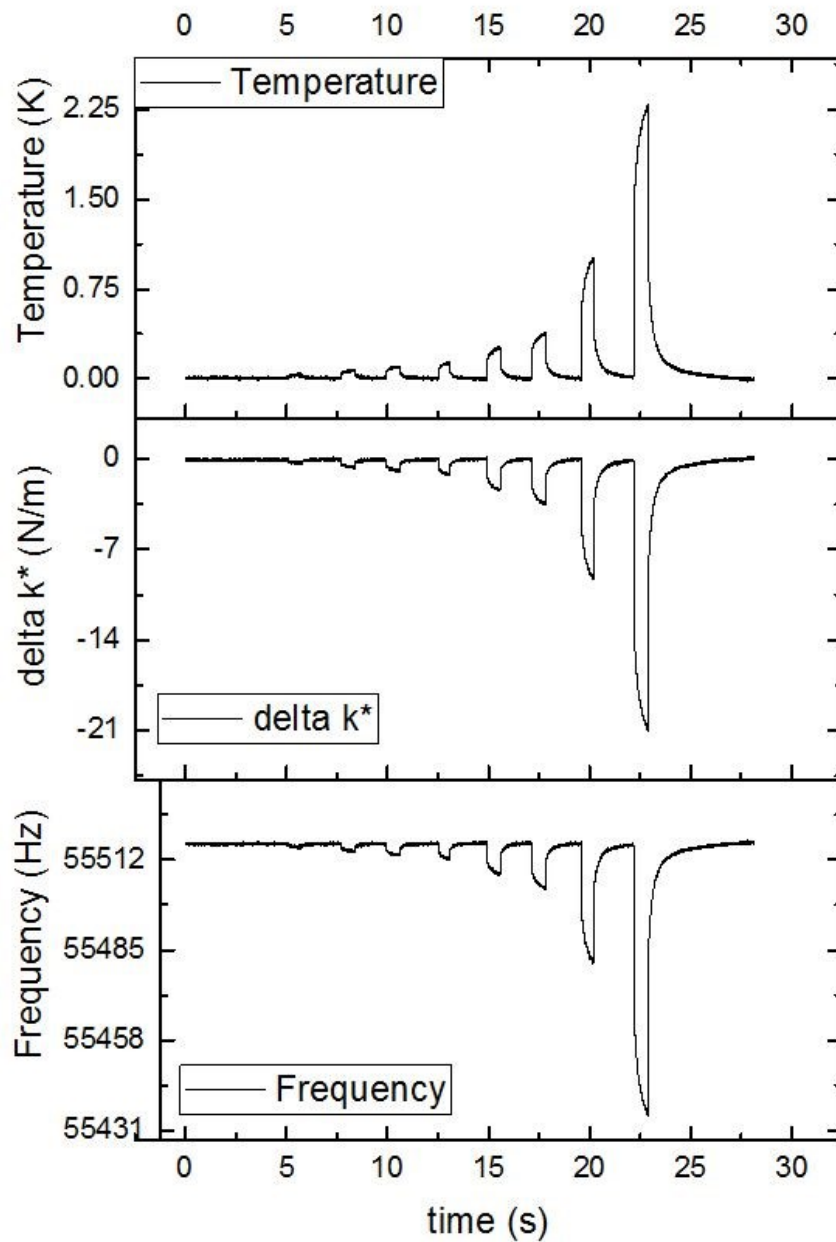


Figure 4.11. Experiment #1 – Glass coverslip – overhead lights ON - Power levels are (right to left): $78.2 \mu W$, $51.9 \mu W$, $34.1 \mu W$, $23 \mu W$, $13 \mu W$, $9.9 \mu W$, $6.4 \mu W$, and $4.3 \mu W$.

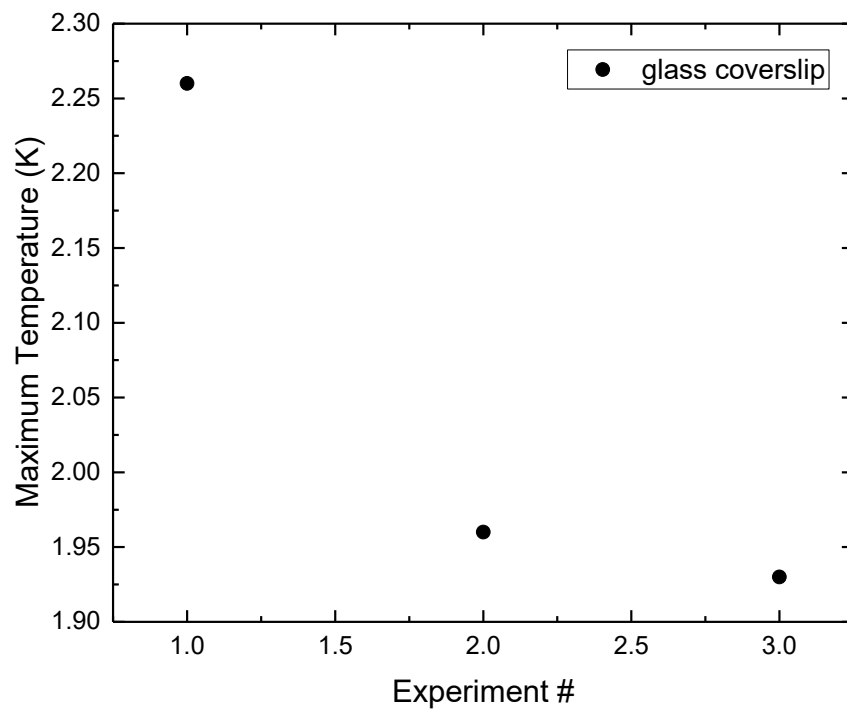


Figure 4.12. Maximum temperature with glass coverslip and overhead lights ON for $78.2 \mu W$ absorbed power

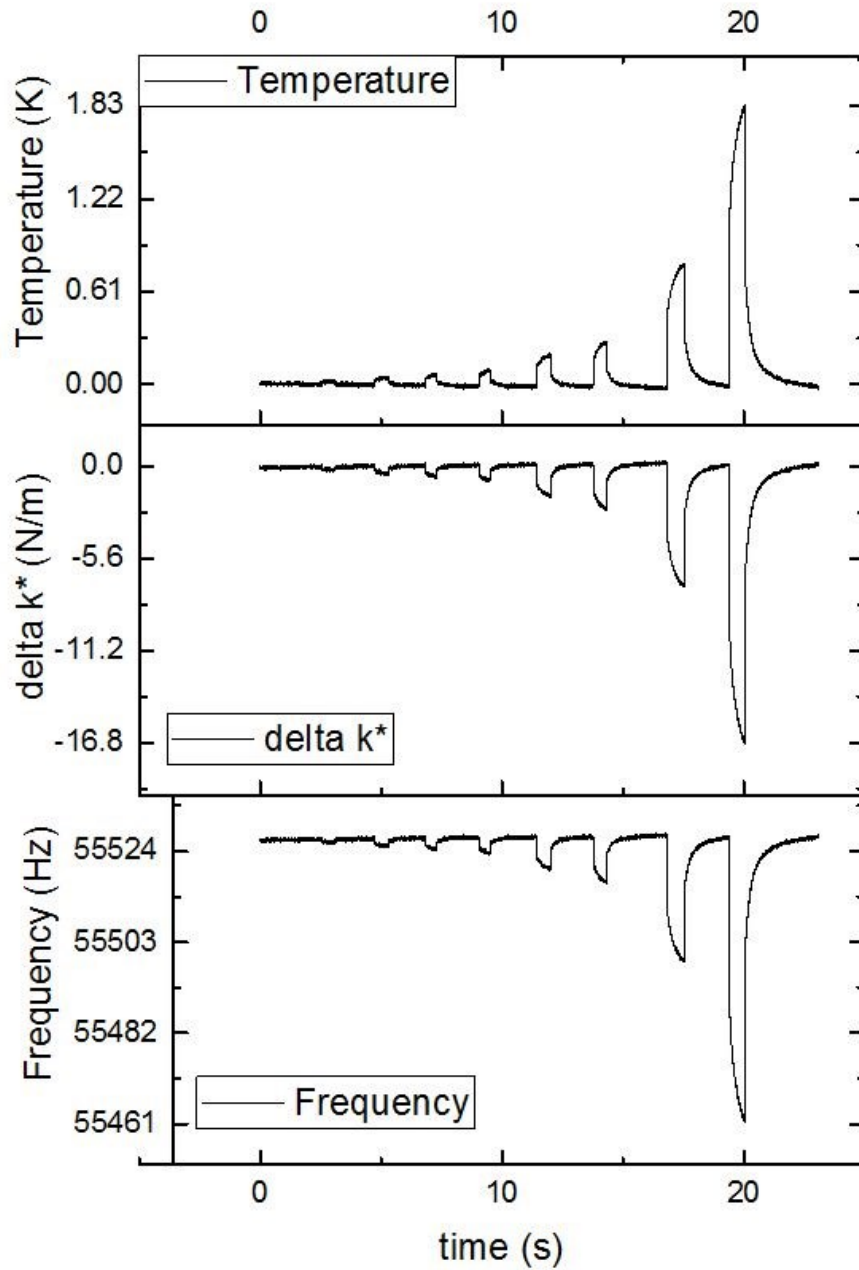


Figure 4.13. Experiment #1 – Glass coverslip – overhead lights OFF - Power levels are (right to left): $78.2 \mu W$, $51.9 \mu W$, $34.1 \mu W$, $23 \mu W$, $13 \mu W$, $9.9 \mu W$, $6.4 \mu W$, and $4.3 \mu W$.

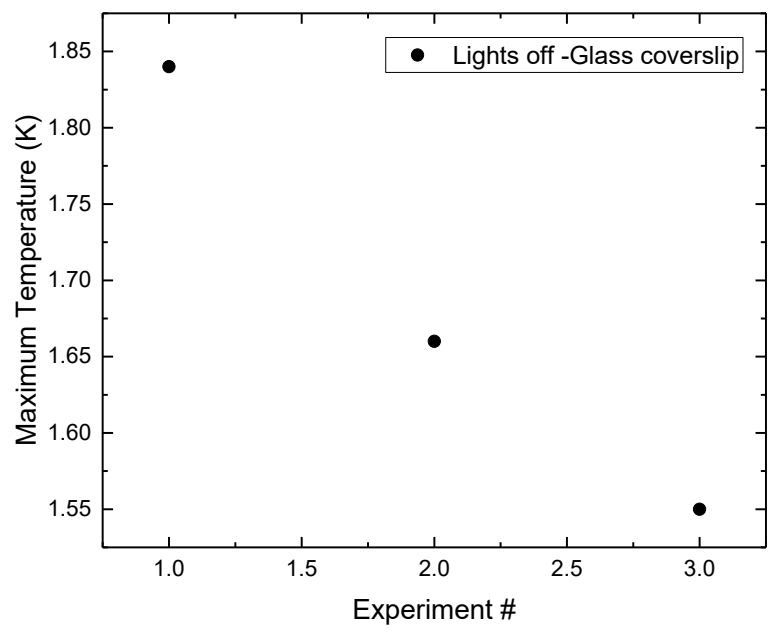


Figure 4.14. Maximum temperature with glass coverslip and overhead lights OFF for $78.2 \mu W$ absorbed power.

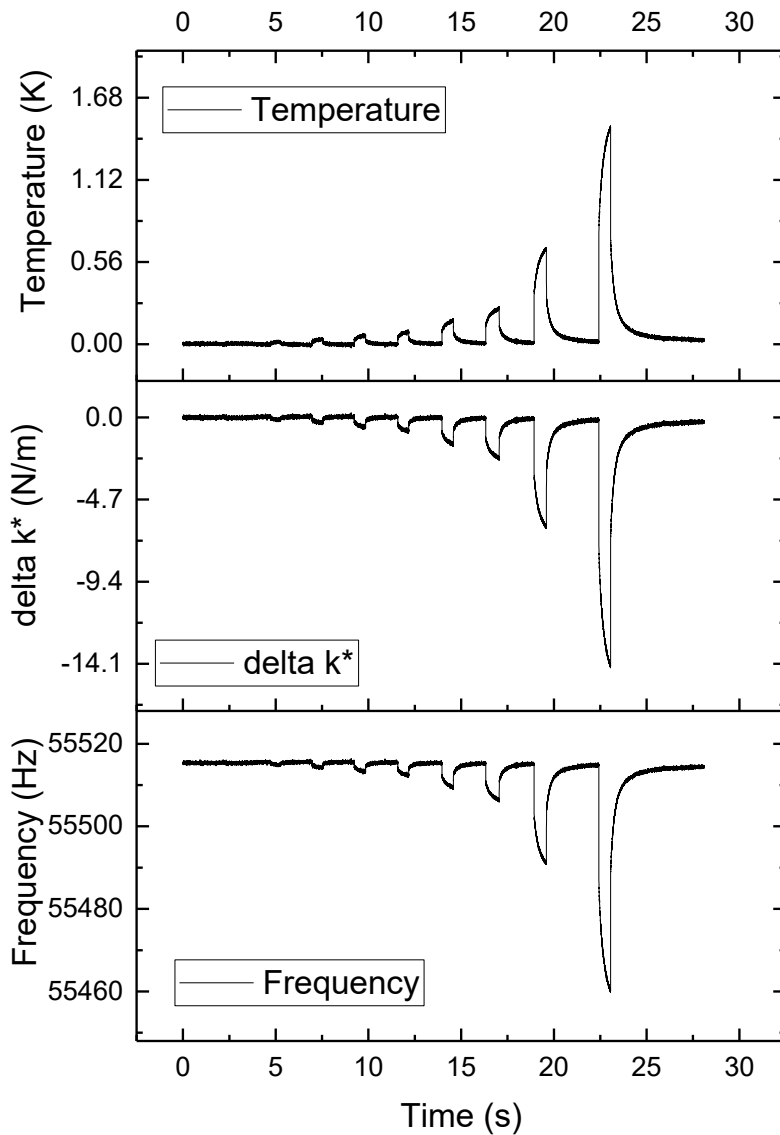


Figure 4.15. Response of a silicon bridge modified QTF to absorbed HeNe laser. Power levels are (right to left): $78.2 \mu W$, $51.9 \mu W$, $34.1 \mu W$, $23 \mu W$, $13 \mu W$, $9.9 \mu W$, $6.4 \mu W$ and $4.3 \mu W$. Reprinted from JE Hawk, MS Ghorraishi, Arindam Phani, and Thomas Thundat, *Exploiting broader dynamic range in Si-bridge modified QTF's for sensitive thermometric applications*, Sensors and Actuators A: Physical, 279, 442-447 (2018).

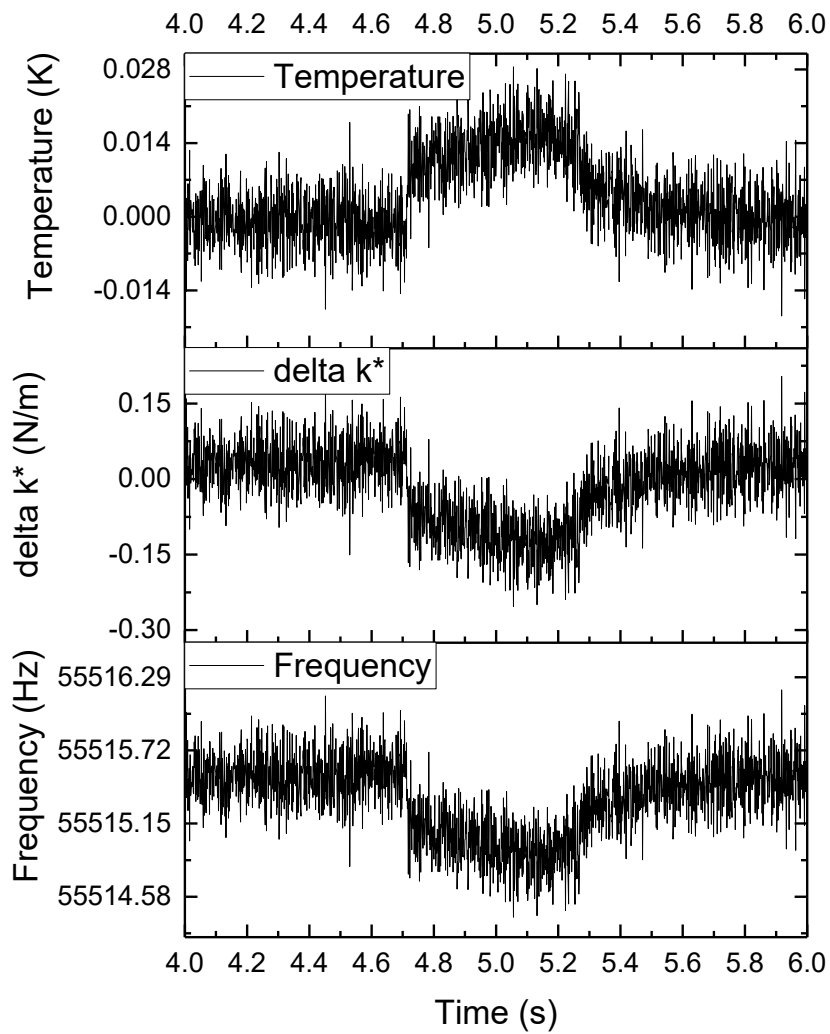


Figure 4.16. Zoomed in portion of Figure 4.19. Response of a silicon bridge modified QTF to HeNe laser at $4.3 \mu W$. Reprinted from JE Hawk, MS Ghoraishi, Arindam Phani, and Thomas Thundat, *Exploiting broader dynamic range in Si-bridge modified QTF's for sensitive thermometric applications*, *Sensors and Actuators A: Physical*, 279, 442-447 (2018).

Fitting of the response in Figure 4.16 shows that the time constant $\tau = C/G = 0.027s$, where C is the thermal capacitance of the sensing element and G is the thermal conductance of the primary heat loss mechanism. Figures of Merit for this modified QTF platform were calculated from Figure 4.16 and are defined as

$$\mathfrak{R} = \frac{Signal}{P_0}$$

$$NEP = \frac{SignalNoise}{\mathfrak{R}}$$

$$D^* = \frac{\sqrt{\beta} \sqrt{A_D}}{NEP},$$

where P_0 is the absorbed power of the element, β is the signal bandwidth, defined as $\beta = 1/2\pi\tau$, and A_D is the device sensing area. Responsivity (\mathfrak{R}), Noise Equivalent Power (NEP), and Specific Detectivity (D^*) were found to be $23kN/m \cdot W$, $8.5 \times 10^{-7} W$, and $4.5 \times 10^4 cm\sqrt{Hz}/W$ respectively. The minimum detectable change in temperature of the bridge sensing element is found by meeting the Rose criterion, which states that a signal to noise ratio of five is necessary to distinguish features [7]. With the signal to noise ratio calculated as the quotient of the signal mean value and the standard deviation of the noise of Figure 4.16, the minimum detectable temperature change is calculated to be $2 mK$.

A previous demonstration of optical signal detection of 635 nm light using a modified QTF was conducted by Tsow and Tao [8] using a single polymeric strand of PS+SC-F105, as discussed in Chapter 1, with a typical radius on the order of a few

micrometers and pulled between the tines of a QTF. Their results are shown in Figure 4.17. for comparison. Whereas they estimated the laser power absorbed by their polymer wire to be 1.1 nW , three orders of magnitude lower than that which is employed here, the sensor response time is markedly slower than that which was obtained using the silicon bridge modified QTF.

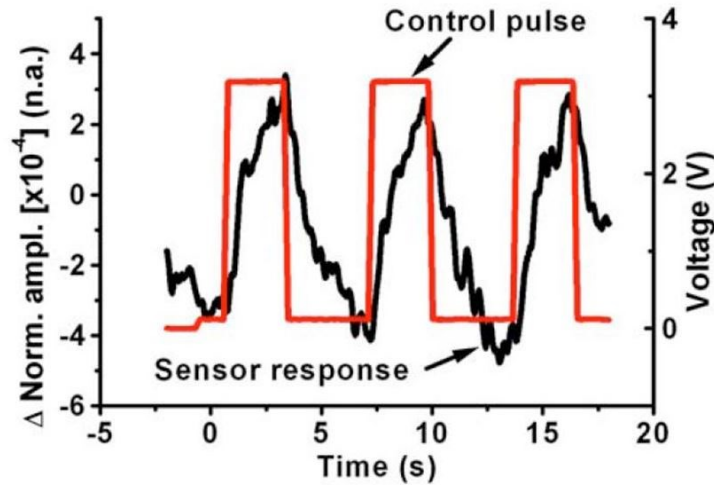


Figure 4.17. Response of PS+SC-F105 polymer to 635 nm incident light (Black) as shown by Tsow and Tao [8] where QTF amplitude of oscillation was used as a proxy for frequency. The red line indicates the laser voltage pulse. Reprinted from, F. Tsow, N. Tao, *Microfabricated Tuning Fork Temperature and Infrared Sensor*, Applied Physics Letters, 90, 174102 (2007), with the permission of AIP Publishing

4.4. Improving Optical fill factor

For typical polymeric strands attached to an unmodified QTF, the optical fill factor, defined as the ratio of a pixel's light sensitive area to its total area, would be only 0.2%. Additional polymer strands, each in parallel, would be required in order to increase the optical fill factor and could quickly lead to inapplicability of the Hookean model, while only offering a maximum fill factor of 33%. However, examination of Figure 2.7 reveals that the addition of more strands, yielding up to $k^*/k_c \approx 0.02$, will only lead to a 1% decrease in sensitivity. This leads to the conclusion that in order to increase device responsivity, df , in pulled polymer QTF devices, the inclusion of additional strands, such that the sensitivity remains high, should be beneficial. To the best of the author's knowledge, this has not yet been tested and is the first time shown here. The silicon bridge modified QTF used in this study provides a 13% fill factor and more readily lends itself to bulk scale production employing stress engineering techniques in the fabrication of the bridging element for increased uniformity between elements, e.g. as demonstrated for piezoelectric micro machined ultrasonic transducers [9]. Through judicious choice of bridging design, the fill factor for silicon bridging elements could be increased to nearly 100%. Further improvements to the sensitivity of the device can be significantly achieved by evacuating the test cell chamber and increasing the thermal isolation of the silicon bridge element from the QTF tines and attaching material in order to reduce heat transfer from the sensing element.

Conclusion

In this chapter, the salient features of the mathematical model were laid out allowing for calculation of thermal variance of the silicon bridging element and were compared with the experimentally induced changes. Both were found to be in close agreement. Further, as the resolution of changes in the stiffness are seen to be directly proportional to the device frequency, multiple devices of differing frequencies were tested and a final optimized 40 kHz device was shown with a temperature resolution of 2mK. In closing, a means to improve the responsivity and optical fill factor of polymeric stranded QTF sensors was discussed by the addition of strands in parallel.

4.5. References

- 1- S.P. Timoshenko, *History of strength of materials*, McGraw-Hill New York (1953).
- 2- H. Watanabe, N. Yumada, and M. Okija, *Linear Thermal Expansion Coefficient of Silicon from 293 to 1000 K*, International Journal of Thermophysics, **25** (2004) 221
- 3- C. Cho, *Characterization of Young's Modulus of Silicon Versus Temperature using a "Beam Deflection" Method with a Four-Point Bending Fixture*, Current Applied Physics, **9** (2009) 538-545
- 4- R.G. Stearns and G.S. Kino, *Effect of electronic strain on photoacoustic generation in silicon*, Applied Physics Letters, 47, 10 (1985)
- 5- P. Datskos, S. Rajic, and I. Datskou, *Photoinduced and thermal stress in silicon microcantilevers*, Applied Physics Letters, Vol 73, No 16, 2319-2321, (1998)
- 6- R.C. Weast, *Handbook of Chemistry and Physics*, 59th ed. Chemical Rubber Company, Boca Raton, FL (1972)
- 7- A.E. Burgess, *The Rose model, revisited*, J. Opt. Soc. Am. A, Vol 16, No 3, 633-646 (1999)
- 8- F. Tsow, N. Tao, *Microfabricated Tuning Fork Temperature and Infrared Sensor*, Applied Physics Letters, 90, 174102 (2007)
- 9- S. Akhbari, F. Sammoura, C. Yang, A. Heidari, D. Horsely, and L. Lin, *Self-Curved Diaphragms by Stress Engineering for Highly Responsive PMUT*, 28th IEEE international Conference on Micro Electro Mechanical Systems, (2015) 837-840)

Chapter 5: Atmospheric sensing–IR fingerprinting

Previous chapters have demonstrated the viability of measuring small changes in temperature using silicon modified QTFs whether through direct heating caused by electromagnetic radiation or from thermal transport from the immediate environment. Both types of heating of the silicon modified QTF, direct and indirect, can readily be induced by exploiting infrared spectroscopic techniques and will be explored in the following chapter. In short, Infrared spectroscopy is the study of the interaction of infrared light with matter.

There are several experimental techniques that are used for the measurement of infrared spectra, Fourier Transform Infrared (FTIR) being the one of most prevalent [1], though this technique will not be discussed here except in passing. Other techniques that bear great resemblance, and in fact rely on similar operational principles as the silicon bridge modified QTF discussed herein, are photothermal cantilever deflection spectroscopy (PCDS) and quartz enhanced photoacoustic spectroscopy (QEPAS).

5.1. Microcantilever based - PCDS

The operational principle of PCDS is fundamentally simple in nature. Infrared light is emitted from a suitable source and, if the light intensity is low, focused using suitable optics onto a standard bimaterial atomic force microscopy cantilevered beam whose position is continually monitored by low power laser light which is reflected off of the

beam onto a suitable position sensitive device (PSD). The output of the PSD is passed into a spectrum analyzer and a lock-in amplifier. The infrared light emitted from the source is modulated using an optical chopping device of some sort. In the instance shown in Figure 5.1 a mechanical chopper is utilized; however, more modern light sources offer the ability to electrically modulate the source using a function generator. In either instance, the modulation signal is passed to the lock-in amplifier as the reference frequency. If the investigated sample absorbs light at the given frequency, it will generate heat which will be detected by deflection of the bimaterial CL beam. A typical experimental setup of PCDS is shown in Figure 5.1.

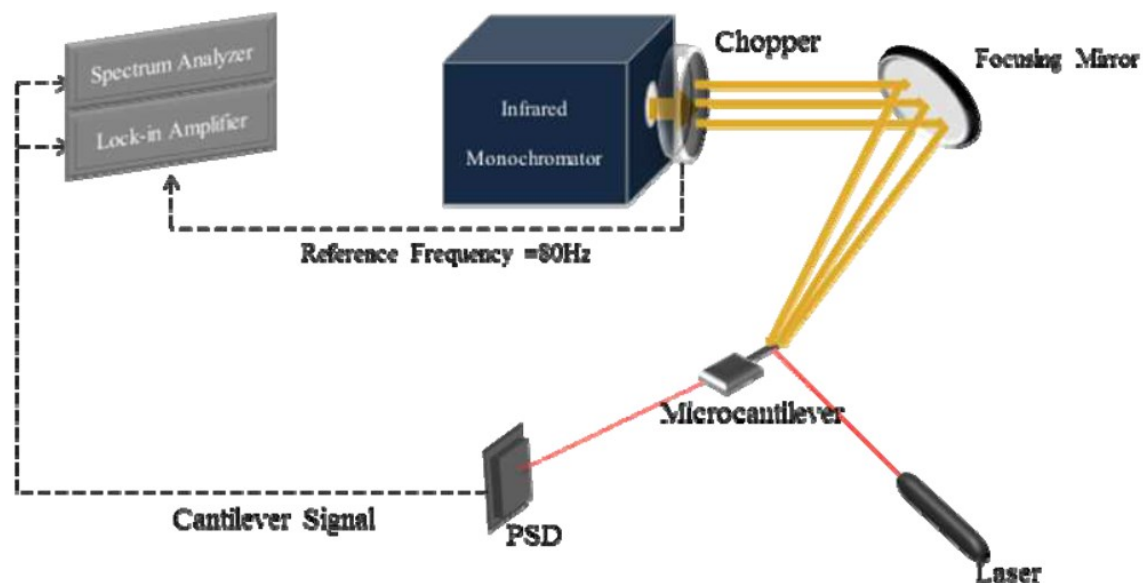


Figure 5.1. Typical PCDS experimental setup as shown by Kim et al. [4] Reprinted with permission from, S. Kim, D. Lee, R. Thundat, M. Bagheri, S. Jeon, and T. Thundat, *Photothermal cantilever deflection spectroscopy*, ECS Transactions, 50 (12) 459-464 (2012). Copyright [2012], The Electrochemical Society

PCDS has been employed to obtain spectra of a variety of samples ranging from vapor phase detection of a nerve gas simulant, dimethyl methyl phosphonate (DMMP) [2], and the explosives, pentaerythritol tetranitrate (PETN), cyclotrimethylene trinitramine (RDX), and trinitrotoluene (TNT) [3], to single stranded DNA [4], and even polymers like poly(methyl methacrylate) (PMMA) [5]. Most recently, PCDS was employed for methane gas sensing [6]. PCDS has been demonstrated as a versatile and sensitive means to obtain mid infrared spectra of a wide range of samples, yet it succumbs to the same potentially deleterious obstacles which befall many CL based systems, namely the requisite optical beam alignment for monitoring of the CL beam itself, and the bulky extraneous equipment required for data acquisition. PCDS is an exemplary laboratory-based system; however, it will require significant investigation and expenditure to relocate the platform for operation in the field.

5.2. Quartz Tuning Fork based

An alternate technique which can be exploited in order to obtain infrared spectra of a sample is photoacoustic spectroscopy (PAS). PAS was first reported in 1881 by Alexander Graham Bell [7], J. Tyndall [8], and W.C. Rontgen [9] when it was observed that acoustic waves were generated when light impinged upon a sample. Once generated, this acoustic wave can be monitored using a simple listening device or

speaker. In 2002, Kosterev et al. [10] replaced the speaker with a QTF and quartz enhanced photoacoustic spectroscopy (QEPAS) was born.

5.2.1. Quartz Enhanced Photoacoustic Spectroscopy - QEPAS

The operational mechanism of QEPAS is fundamentally simple, as light of a given frequency is absorbed by the gas sample, the excited molecules will either relax to their ground state via emission of a photon or through a non-radiative process. These processes will produce a localized heating of the gas, which will result in a change of the local pressure. By modulating the intensity of the incident light, this localized heating and pressure wave can then be used to drive the QTF into oscillation [11]. In their initial disclosure, Kosterev et al. tested a variety of beam configurations which are shown in Figure 5.2 and, using the arrangement shown in b) of the same Figure, monitored the Q branch of the $2\nu_3$ overtone of methane gas shown in Figure 5.3 at concentrations of 6.7% and 0.17% respectively.

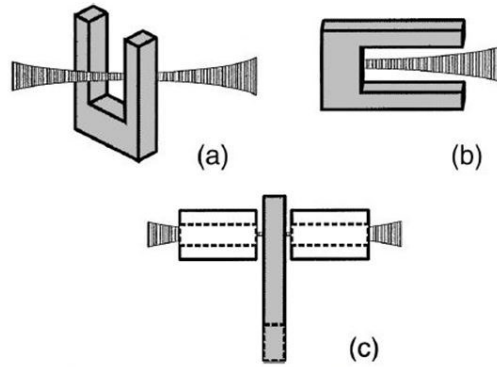


Figure 5.2. QEPAS configurations. (a) The laser is passed between the tines of the QTF. (b) The laser impinges onto the QTF. (c) The laser is directed through an acoustic resonator tube. As shown by Kosterev et al. [10] Reprinted with permission from A.A. Kosterev, Yu. A. Bakhirkin, R.F. Curl, and F.K. Tittel, *Quartz-Enhanced Photoacoustic Spectroscopy*, *Optics Letters*, Vol 27 No 21, 1902-1904 (2002), OSA Publishing

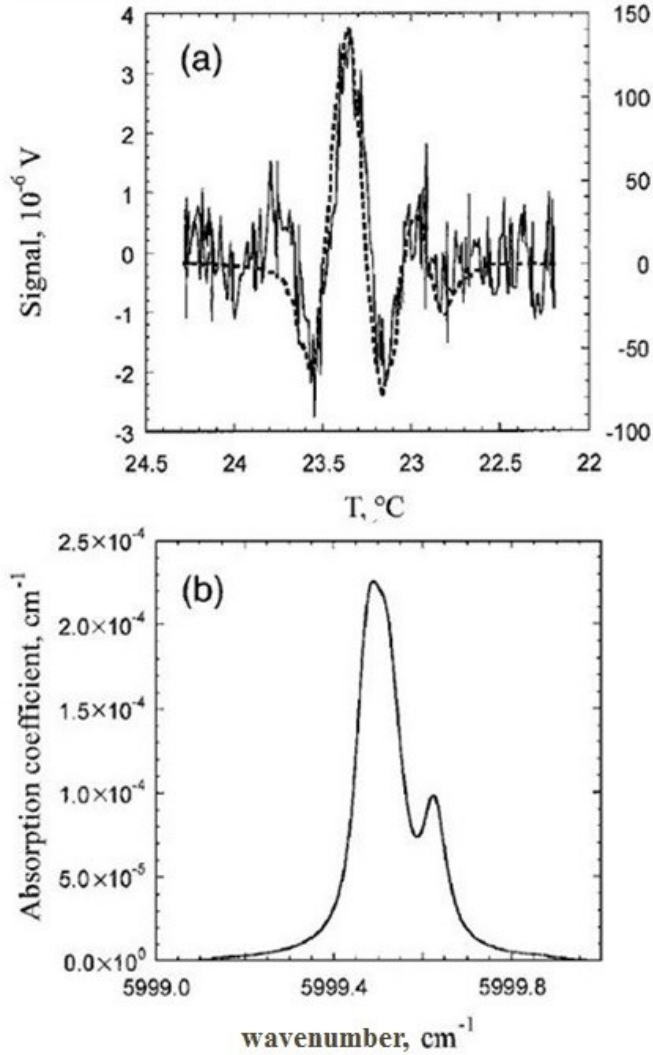


Figure 5.3. Spectral data of the $2\nu_3$ methane line using QEPAS. (a) Dashed curve depicts 6.7% (right axis) and the solid curve depicts 0.17% (left axis) methane concentrations. The total cell pressure is 375 Torr. The x-axis is temperature of the laser used which controls the laser output frequency (b) Simulated methane absorption at 0.17% concentration using HITRAN'96 data. As shown in [10] Reprinted with permission from A.A. Kosterev, Yu. A. Bakhirkin, R.F. Curl, and F.K. Tittel, *Quartz-Enhanced Photoacoustic Spectroscopy*, Optics Letters, Vol 27 No 21, 1902-1904 (2002), OSA Publishing

The use of an acoustic resonator tube has increased the sensitivity of QEPAS, and it has been demonstrated to detect parts per billion (ppb) levels of Carbon Monoxide and Nitrous Oxide [12], Nitric Oxide [13], and more recently ppb levels of ammonia [14], and finally this platform has been fashioned into a portable Carbon Dioxide sensor [15]. Irrespective of the employment scheme chosen for QEPAS, the measured signal strength, S , of the QTF will be a function of the concentration of the sample gas, C , power of the exciting laser, P , the absorption cross section of the sample at the given optical frequency, σ , the Quality factor of the QTF, Q , and the frequency of the QTF resonator, f , and can be expressed as [16]:

$$S \approx \frac{C\sigma PQ}{f}. \quad (\text{Equation 5.1})$$

5.2.2. Standoff Photoacoustic Spectroscopy

A similar approach to QEPAS was undertaken in 2008 by Van Neste et al.; however, they removed the QEPAS constraint that the vapor phase sample must be in intimate contact with the QTF. In their approach, a beam of IR light was reflected off of a potentially contaminated surface and the reflected signal was directed onto one of the tines of the QTF. This approach allows for standoff capabilities in which the QTF effectively observes the inverse of a standard IR spectrum. Succinctly put, if the sample species absorbs the incident radiation, there will be a reduction of light which falls upon, and thus drives, the QTF into oscillation as the light is modulated at the resonant

frequency of the QTF. By monitoring the amplitude of the QTF, the inverse of the IR absorption spectrum is readily obtained. This technique, shown in Figure 5.4, was used to detect tributyl phosphate (TBP), and explosives residues of cyclotrimethylenetrinitramine (RDX), trinitrotoluene (TNT), and pentaerythritol tetranitrate (PETN) at distances up to 20 meters [17- 20].

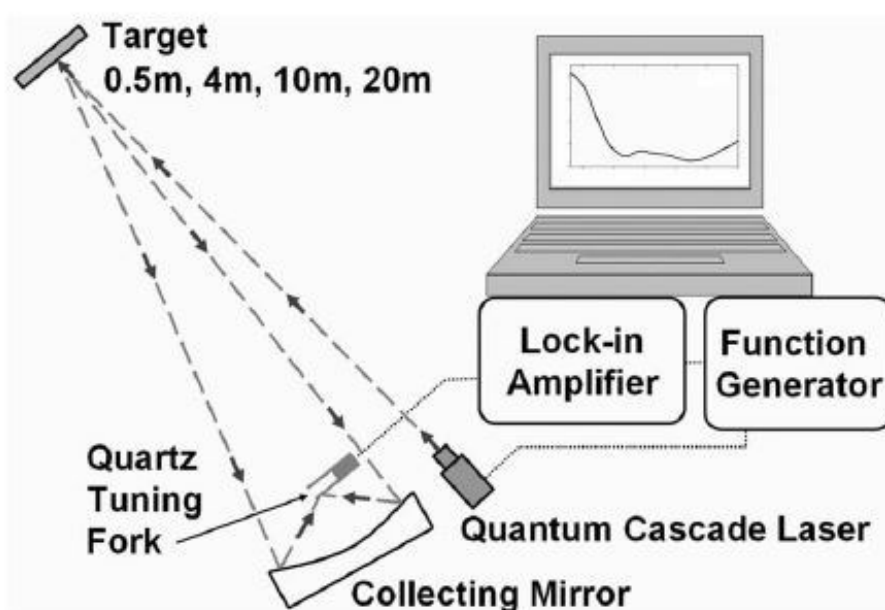


Figure 5.4. Standoff Photoacoustic Spectroscopy as shown in [17]. Reprinted from, C.W. Van Neste, L.R. Senesac, and T. Thundat, *Standoff photoacoustic spectroscopy*, Applied Physics Letters, 92, 234102 (2008), with the permission of AIP Publishing.

Though not directly discussed in these publications, private communication with C.W. Van Neste has confirmed this author's suspicion that the QTF response can be increased with the addition of a broadband IR absorber, i.e. candle black, onto the tines

of the QTF. In a manner similar to QEPAS, the measured signal strength, S , of the QTF will be a function of the concentration of the adsorbed sample, C , power of the exciting laser, P , the absorption cross section of the sample at the given optical frequency, σ_{sample} , the Quality factor of the QTF, Q , the frequency of the QTF resonator, f , and the absorption coefficient of the IR absorber on the QTF, α_{QTF} , and can be expressed as

$$S \approx \frac{\sigma_{QTF} P Q}{C \alpha_{sample} f}. \quad (\text{Equation 5.2})$$

Both methodologies above, QEPAS and Standoff Photoacoustic Spectroscopy, are the only techniques the author is currently aware of that exploit the QTF for spectroscopic applications, however both of these use the QTF in an unmodified format. Of the literature to date, only one attempt has been made for the detection of IR signals using a modified QTF when Tsow and Tao [21] observed the response of a polymer strand modified QTF to thermal radiation emitted from a soldering iron, see Figure 5.5. Needless to say, their observation was of a broadband IR response and not frequency selective as required for spectroscopic applications.

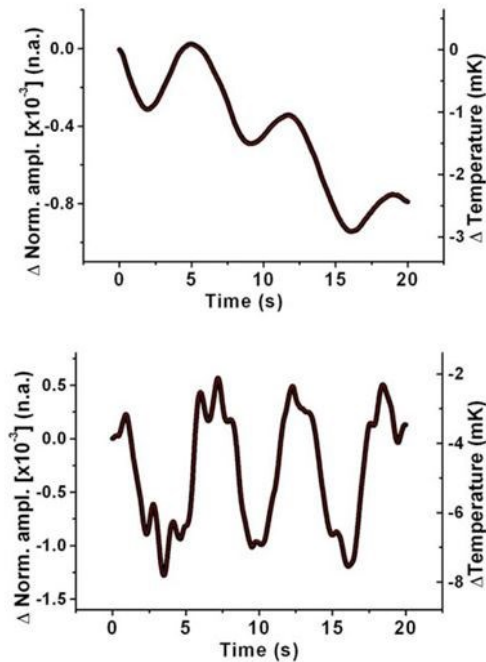


Figure 5.5. Response of a poly(N-isopropylacrylamide) polymer strand modified QTF as shown in [21]. Response to 98 °C soldering iron at 25 cm (top) and 110 °C soldering iron at 25 cm (bottom). Reprinted from, F. Tsow, N. Tao, *Microfabricated Tuning Fork Temperature and Infrared Sensor*, Applied Physics Letters, 90, 174102 (2007), with the permission of AIP Publishing.

5.2.3. Silicon bridge modified QTFs

As has been previously discussed, silicon bridge modified QTFs, as used in this work, are highly sensitive to thermal variance and thus readily lend themselves to the investigation of IR spectra. Indeed, it was observed during the course of this present study that a silicon bridge modified QTF is capable of operation in two distinct modes where either a net cooling or a net heating of the element is observed while still recording appropriate IR spectral responses. To allow for direct comparison of the

modified QTF's response to that obtained previously by Rahimi et al. using a PCDS system, methane gas at various concentrations was studied.

In order to investigate the infrared response of the modified QTF, the system was arranged in a similar manner as that for bolometric sensing using HeNe laser light. The experimental setup is outlined in Figure 5.6.

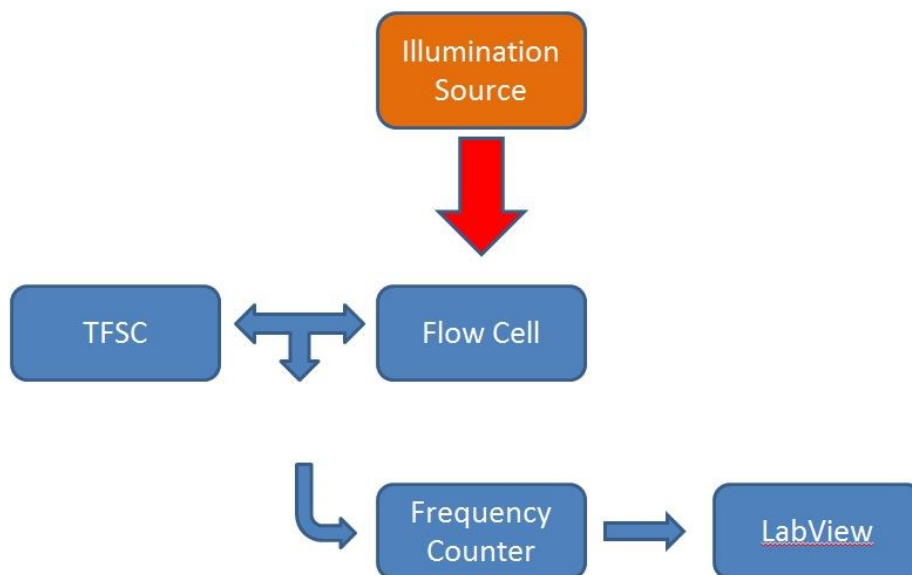


Figure 5.6. Experimental setup for infrared spectral data acquisition.

Two tanks of Methane gas, at concentrations of 1000 ppm and 2.5 volume % respectively, were obtained from Praxair Canada and were proportionally mixed using Attovac Mass Flow Controllers which maintained a constant total gas flow of 100 scfm. The illumination source was a Daylight Solutions Quantum Cascade Laser (QCL) which produces infrared light in the range of 1145 cm^{-1} to 1410 cm^{-1} (8733 nm to 7092 nm) and is conducive to investigating the response of the ν_4 spectral line of methane centered at 1306 cm^{-1} (7656 nm). A modified QTF was housed within the custom flow

cell and the QCL light was directed, as closely as possible, such that it impinged on the surface normal of the silicon bridging element

The fundamental operational principle of the silicon bridge modified QTF sensor, as demonstrated in Chapter 4, is the detection of thermal variance which expresses itself as a change in the net internal stress of the silicon bridging element. As was also seen in Chapter 4, the light emitted from the QCL, which then impinges upon the bridging element, will attenuate as it propagates through the element in accordance with Beer-Lambert's law, thus leading to a heating of the element due to the absorption of the optical energy and the subsequent increase in thermal stress. In the same manner as with the HeNe laser, this heating results in a net decrease in the measured QTF frequency, as is predicted. As the photon energy at these frequencies is below the band gap of the silicon, there is no photo-induced stress for this set of experiments.

5.2.3.1. Long optical path

In order to determine the viability of utilizing the device as a platform to conduct infrared spectroscopic measurements, the flow cell was modified such that the optical path length could be increased. To this end, a 5.0 cm lens tube was purchased from Thor Labs and fitted on one end with a Zinc Selenide window. Zinc Selenide is optically transparent to infrared light at the frequencies used throughout this experiment. Modification of the flow cell arrangement is shown in Figure 5.7.

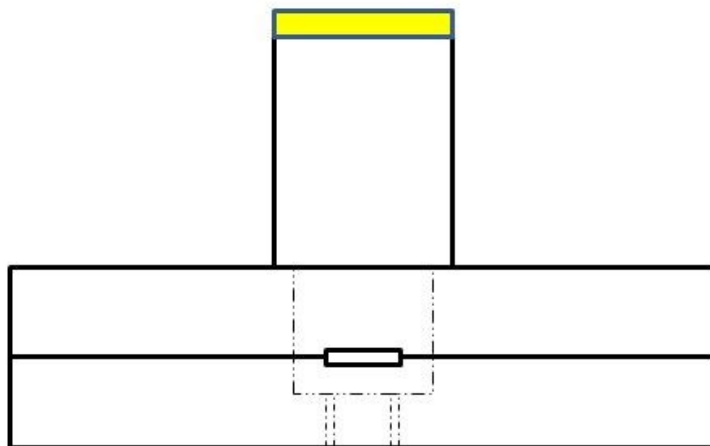


Figure 5.7. Modified custom flow cell with 5.0 cm optical tube with Zinc Selenide window (yellow)

As was pointed out in Chapter 4, the Beer-Lambert equation can be expressed as $A = \ln\left(\frac{P_{Incident}}{P_{Trans}}\right) = \sigma LN$ and is readily apparent to be a linear function of both number of molecules per unit volume and optical path length. By stepping the QCL through the Q-branch of the methane ν_4 peak in the range of 1294 cm^{-1} to 1316 cm^{-1} (7727.98 nm to 7598.78 nm) in increments of 0.25 cm^{-1} ($\approx 1\text{ nm}$), and repeating this procedure for various concentrations, it becomes possible to perform a linear fit of the absorbance response at each wavenumber for each concentration. The slope of the best fit line will give the absorption cross-section at each wavenumber, provided that the sensing element yields a linear response. This necessary linearity of response of the silicon bridge modified QTF to thermal variances was shown in Figure 4.2 of Chapter 4,

In the long optical path mode of operation, the silicon bridging element behaves much in the same manner as a light intensity detector. By maintaining a constant optical power directed through the sample and impinging on the silicon bridge, any diminution of the optical signal and concomitant cooling of the silicon bridge, indicates absorption of the optical signal by the vapor sample. Figure 5.8 shows the decrease in the frequency of the silicon bridge modified QTF from 56300 Hz to the methane concentration dependent levels ranging from 54250 Hz to 54350 Hz upon excitation with the QCL, as well as one set of the responses of the modified QTF for various concentrations of methane for comparison of the same ν_4 response that was previously shown by Rahimi et al. using photothermal cantilever deflection spectroscopy shown in Figure 5.9 [6].

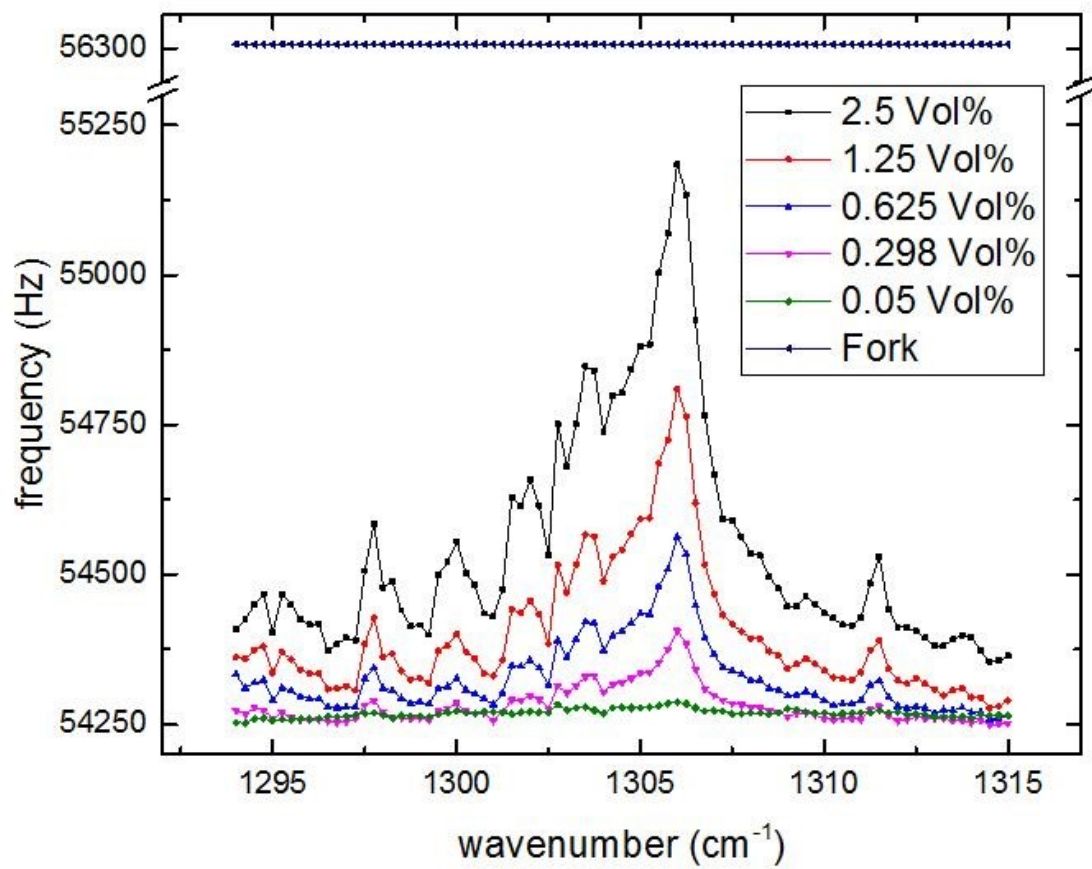


Figure 5.8. Long optical path (5.3 cm) frequency response of a silicon bridge modified QTF for various concentrations of methane.

For comparison to the data presented by Rahimi et al. [6], the wavelengths are (left to right) 7598.78 nm to 7727.98 nm

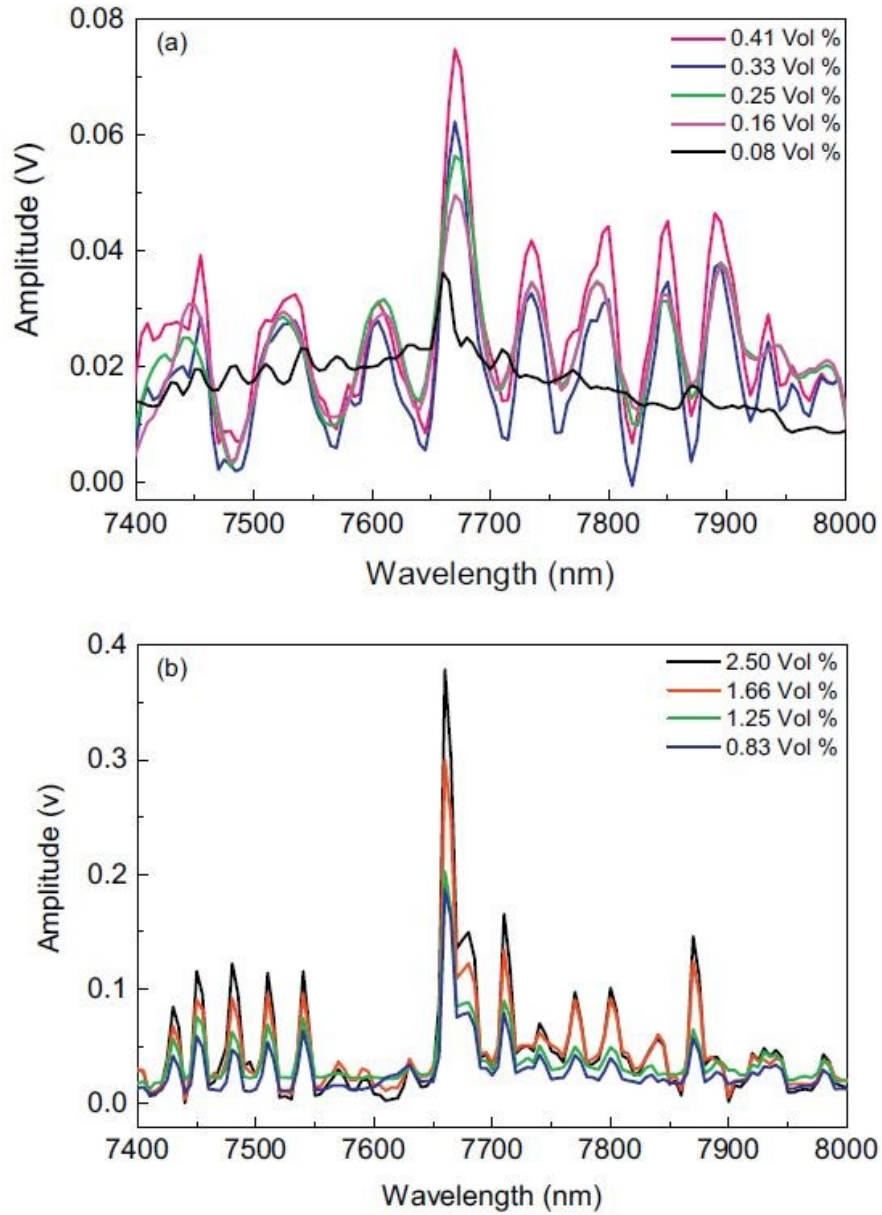


Fig. 4. PCDS spectrum of methane. (a) 0.08–0.41 vol%. (b) 0.83–2.5 vol%.

Figure 5.9. Methane spectrum as obtained by Rahimi et al. [6], the largest central response is at Q branch at 7656 nm (1306 cm^{-1}). Reprinted with permission from M. Rahimi, I. Chae, J.E. Hawk, S.K. Mitra, and T. Thundat, *Methane sensing at room temperature using photothermal cantilever deflection spectroscopy*, *Sensors and*

Actuators B:Chemical, 221 (2015) 564-569

The mid IR spectrum of methane gas was obtained for a range of concentrations from 2.5 Vol% down to 0.006 Vol%, and plotted as a function of excitation wavenumber. Scans at each concentration were repeated three times; however the responses below 0.05 Vol% were too small and were excluded from some figures which follow. The net change in frequency, after subtraction of the IR background illumination heating, is shown in Figure 5.10 with error bars and in Figure 5.11 without error bars for clarity.

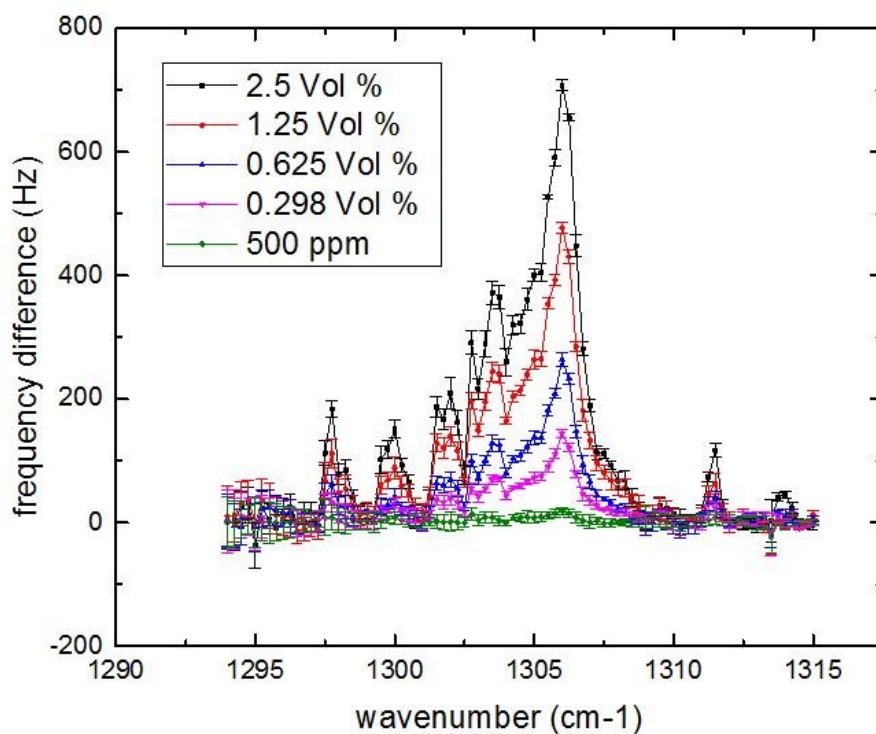


Figure 5.10. 5.3 cm optical path. Frequency difference after subtraction of IR background for various concentrations of methane gas for each wavenumber. With error bars.

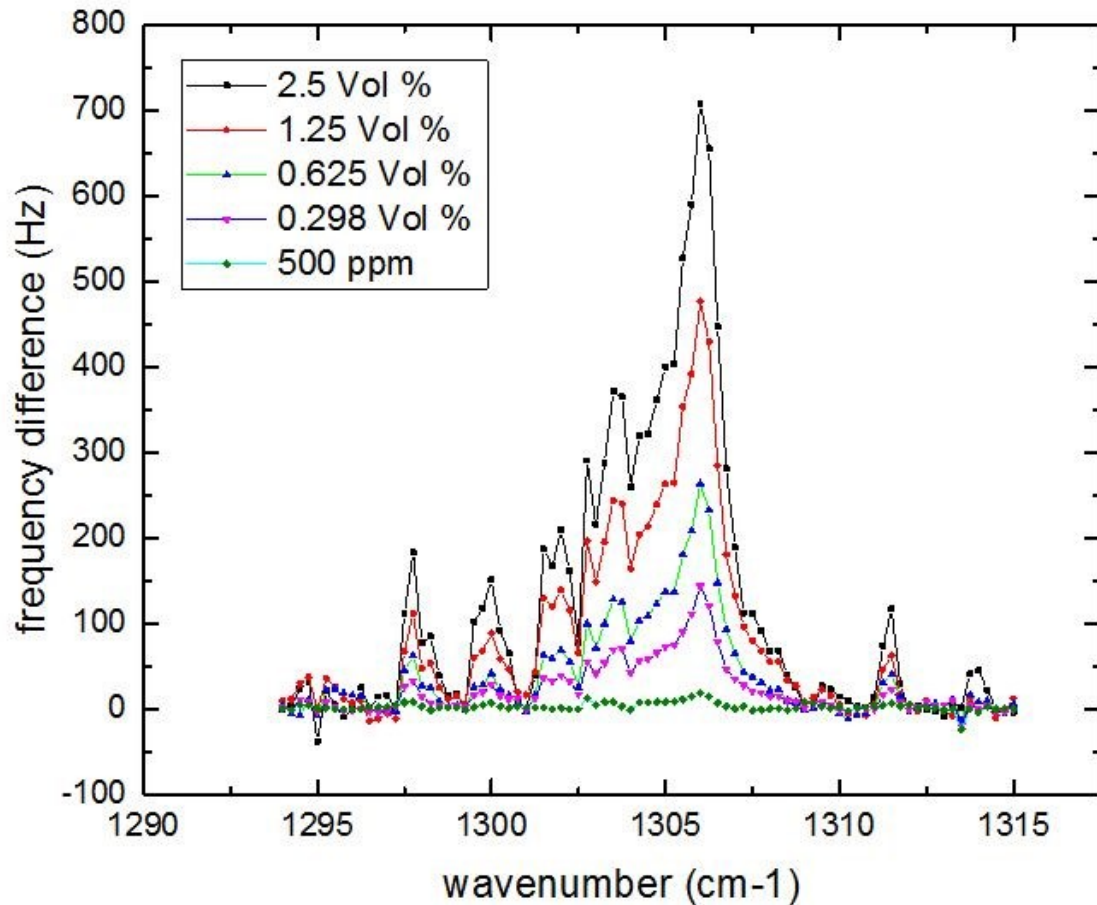


Figure 5.11. 5.3 cm optical path. Frequency difference after subtraction of IR background for various concentrations of methane gas for each wavenumber. Without error bars.

The changes in the silicon bridge's spring constant, derived in the same manner as the preceding chapter, are shown in Figure 5.12, with the 0.05 Vol % shown in Figure 5.13 demonstrating a net "stiffening" of the bridging element. The amount of heating that would be required to cause each respective change in stiffness of the bridging element is shown in Figure 5.14 for all methane concentrations tested; with the 0.05 Vol% concentration response shown in Figure 5.15 for clarity. For the sake of

completeness, the temperature response of the lowest concentrations is shown in Figure 5.16.

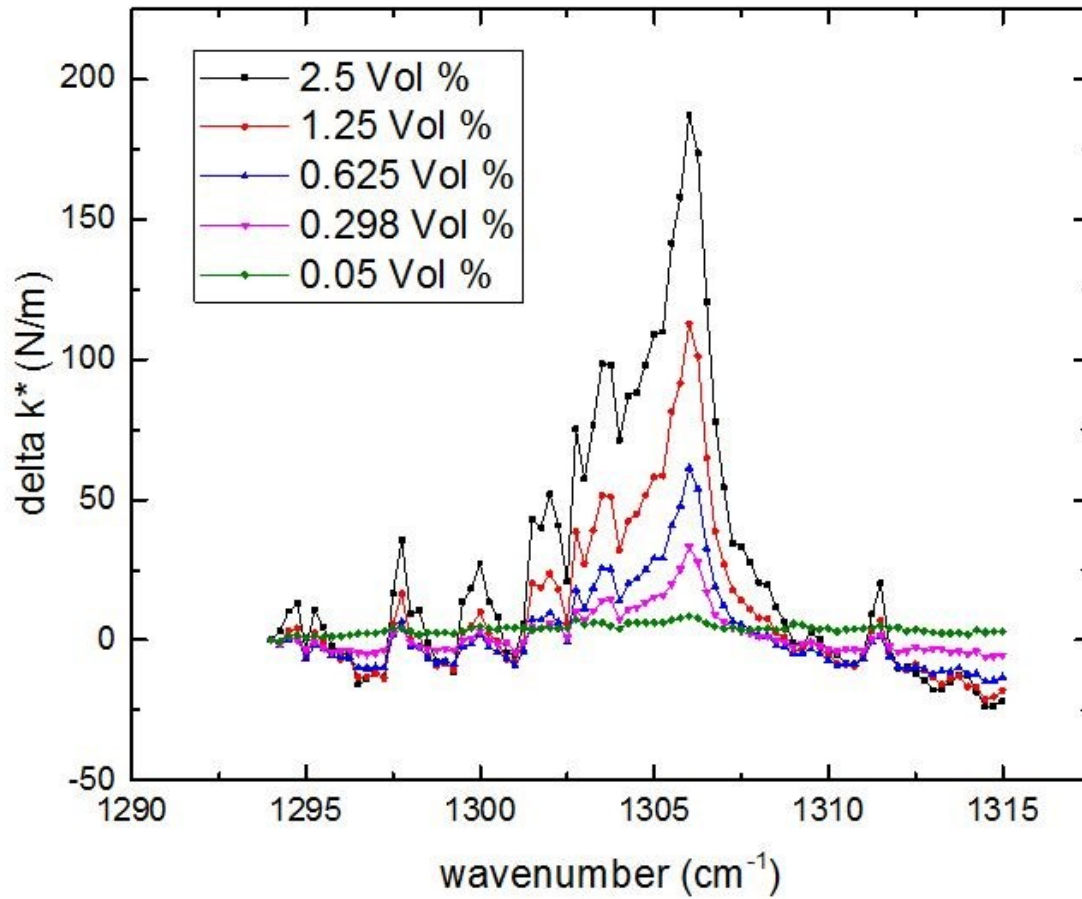


Figure 5.12. 5.3 cm optical path. Change in spring constant as a function of wavenumber for various concentrations of methane gas.

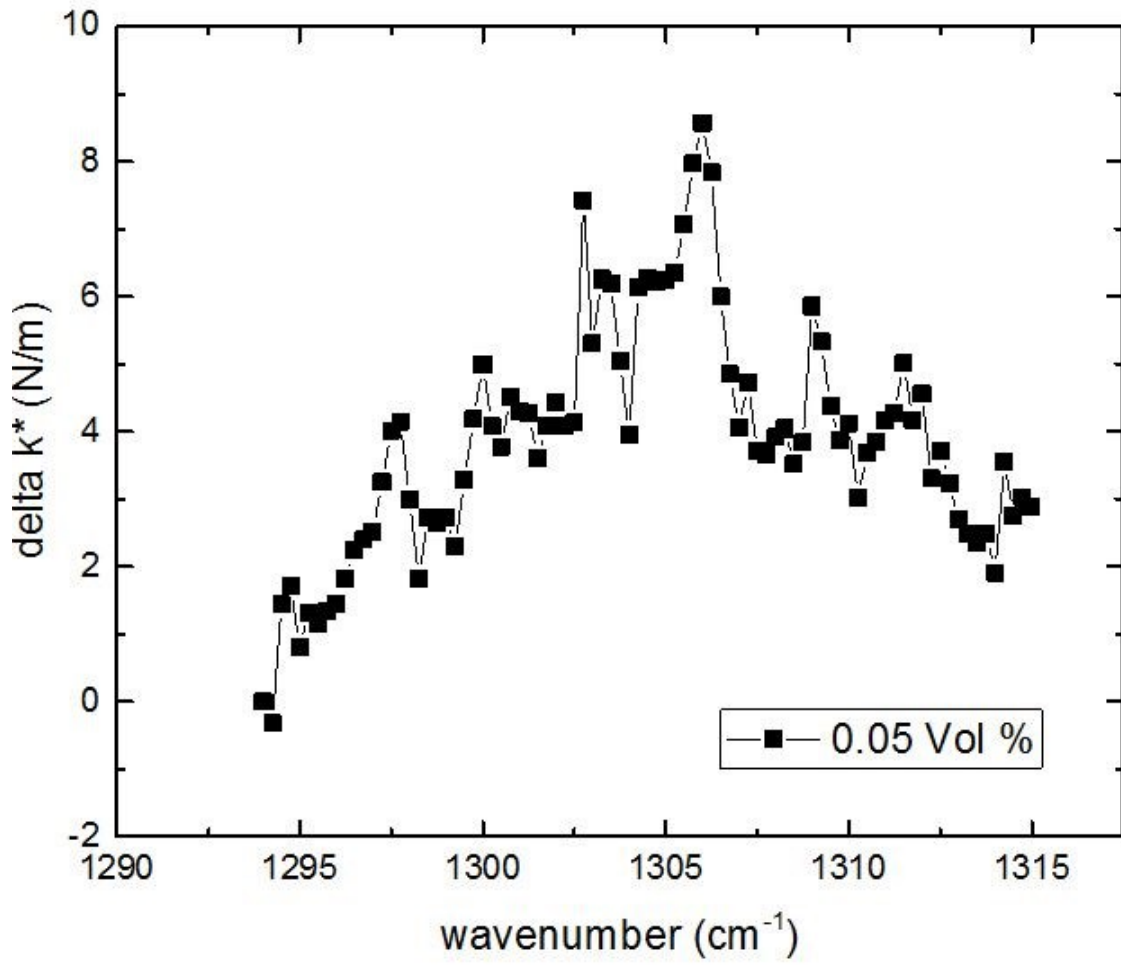


Figure 5.13. 5.3 cm optical path. Change in spring constant as a function of wavenumber for 0.05 Vol% concentration of methane gas.

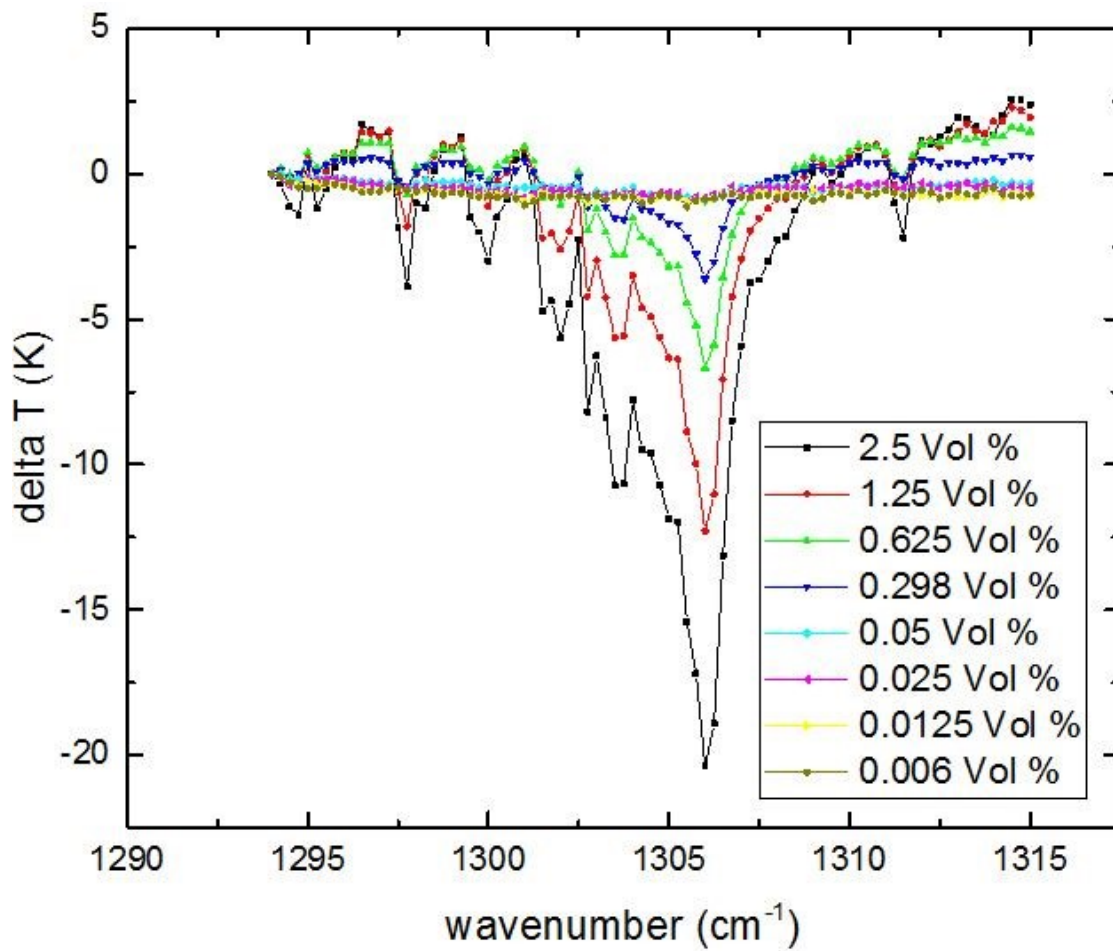


Figure 5.14. 5.3 cm optical path. Change in temperature as a function of wavenumber for various concentrations of methane gas.

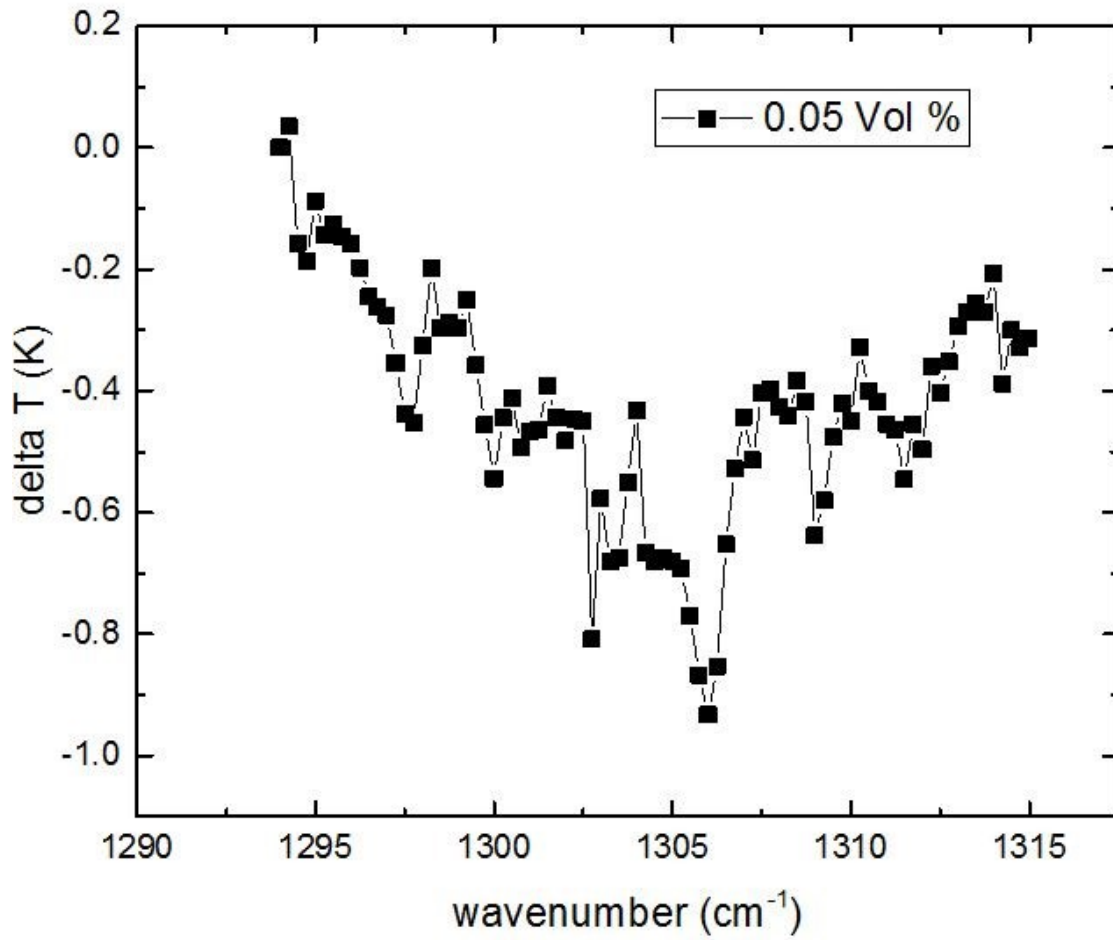


Figure 5.15. 5.3 cm optical path. Change in temperature as a function of wavenumber for 0.05 Vol% concentrations of methane gas.

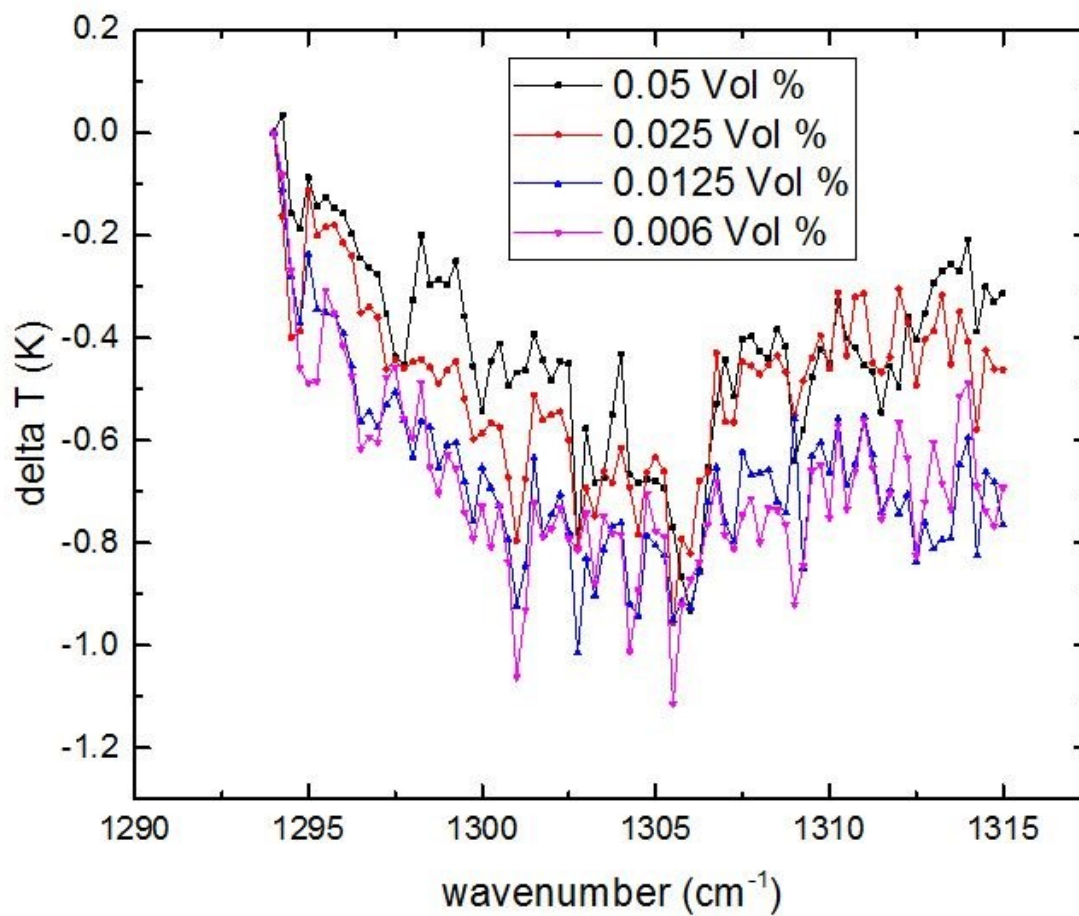


Figure 5.16. 5.3 cm optical path. Change in temperature as a function of wavenumber for lowest concentrations of methane gas tested.

Verification of the linearity of response of the silicon bridge modified QTF is redundantly confirmed by exploiting the Beer-Lambert relation for calculation of the absorption cross section. However, the raw frequency data alone is not sufficient to allow for its immediate calculation, as the change in spring constant scales as a function of frequency squared. It thus becomes necessary to convert the frequency data to spring constant of the bridging element. Once the necessary conversions are performed, it is a

simple matter, as shown in Figure 5.17, to obtain the absorption cross-section shown in Figure 5.18, which can be compared to a reference standard available from Pacific Northwest National Laboratory (PNNL) shown in Figure 5.19.

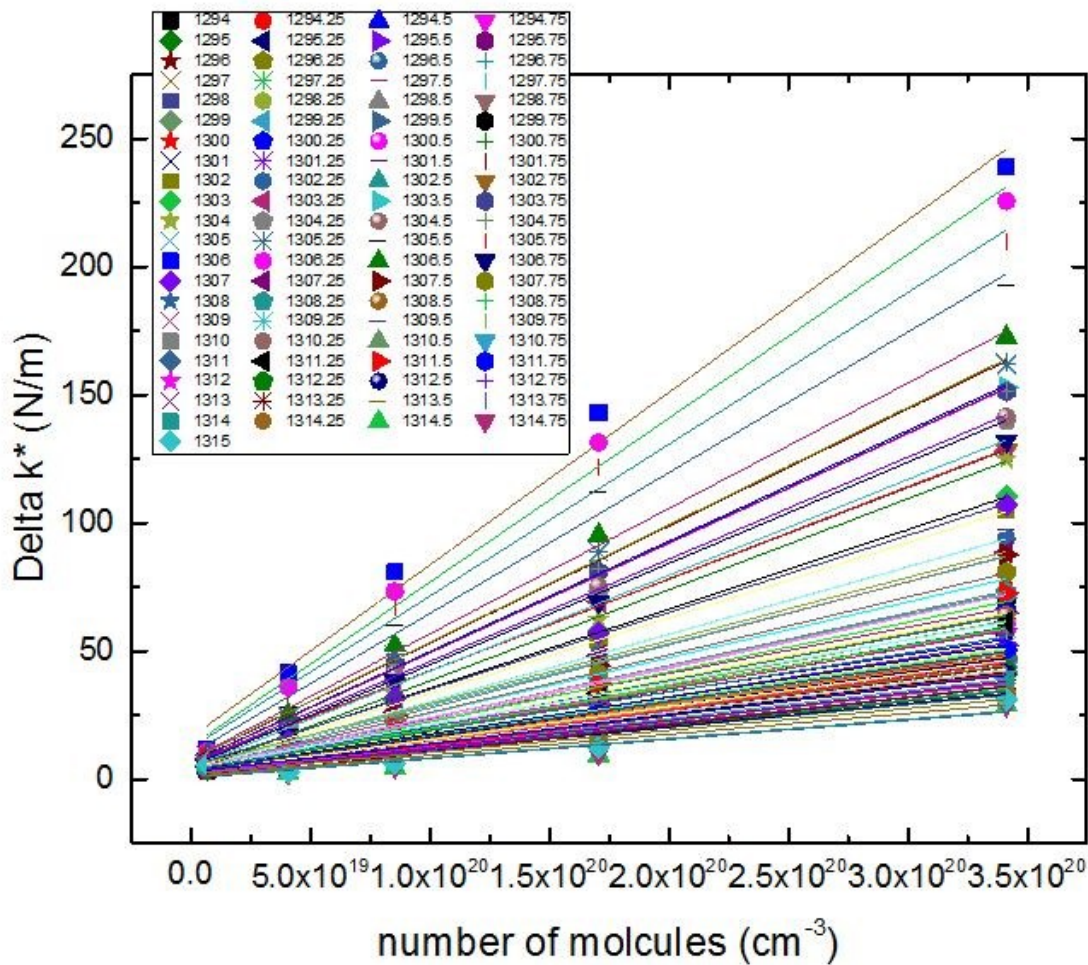


Figure 5.17. Fitting of change in spring constant for various concentrations of methane gas, in terms of the number of molecules per cm³. The slope at each wavenumber is the absorption cross-section for that wavenumber.

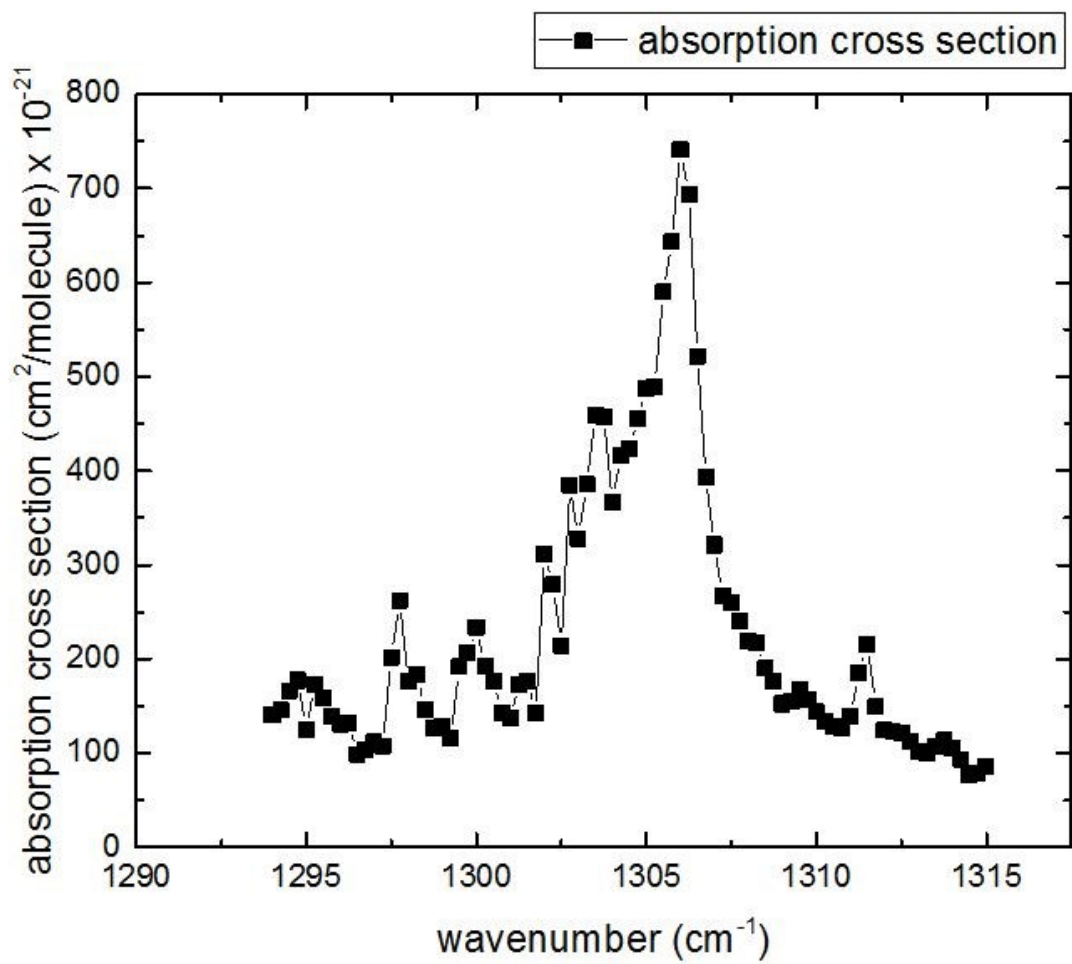


Figure 5.18. Absorption cross-section of methane gas as measured using a silicon bridge modified QTF.

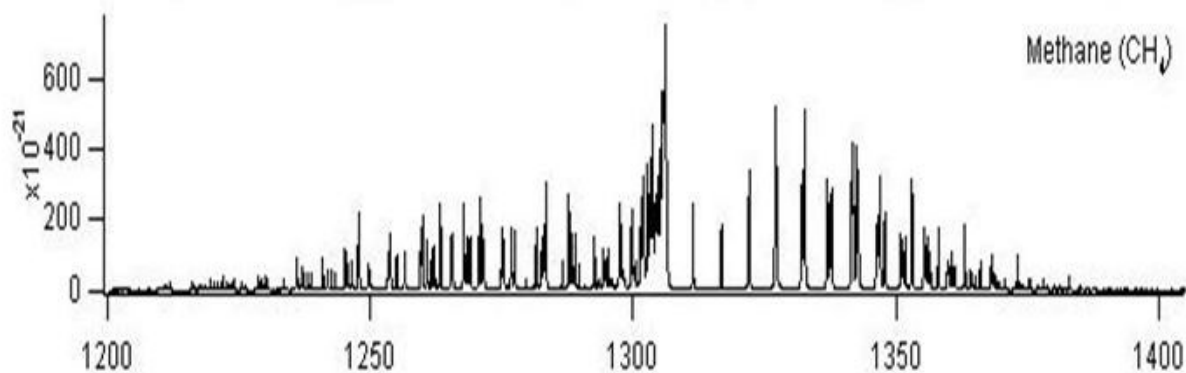


Figure 5.19. Absorption cross-section data obtained from Pacific Northwest National Laboratory (PNNL)

As can be seen by comparison of Figure 5.8 and Figure 5.9, the response of the silicon bridged QTF, for the 5.3 cm optical path length demonstrated, shows a slightly better lower limit of detection than that reported using PCDS. However, this lower detection limit can be easily improved by simply increasing the length of the sample chamber.

5.2.3.2. Short optical path

An alternate mode of operation was also investigated utilizing an optically short path length through the methane gas. The configuration was modified from the previous arrangement by removing the lens tube and directly affixing the Zinc Selenide window to the top of the custom flow cell. This allowed the optical path length to be reduced to approximately 3 mm, shown in Figure 5.20, and the silicon bridge modified QTF response is detailed in Figure 5.21.

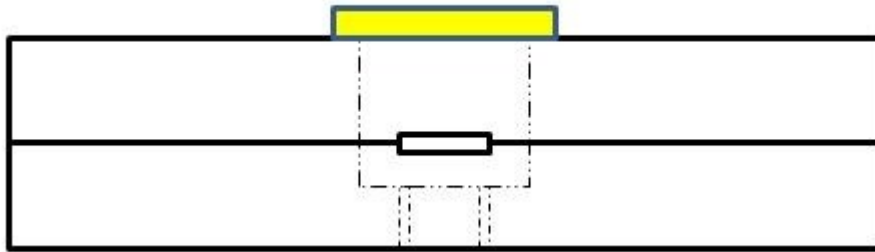


Figure 5.20. Modified custom flow cell with Zinc Selenide window (yellow) affixed directly on top. Optical path length is approximately 3 mm.

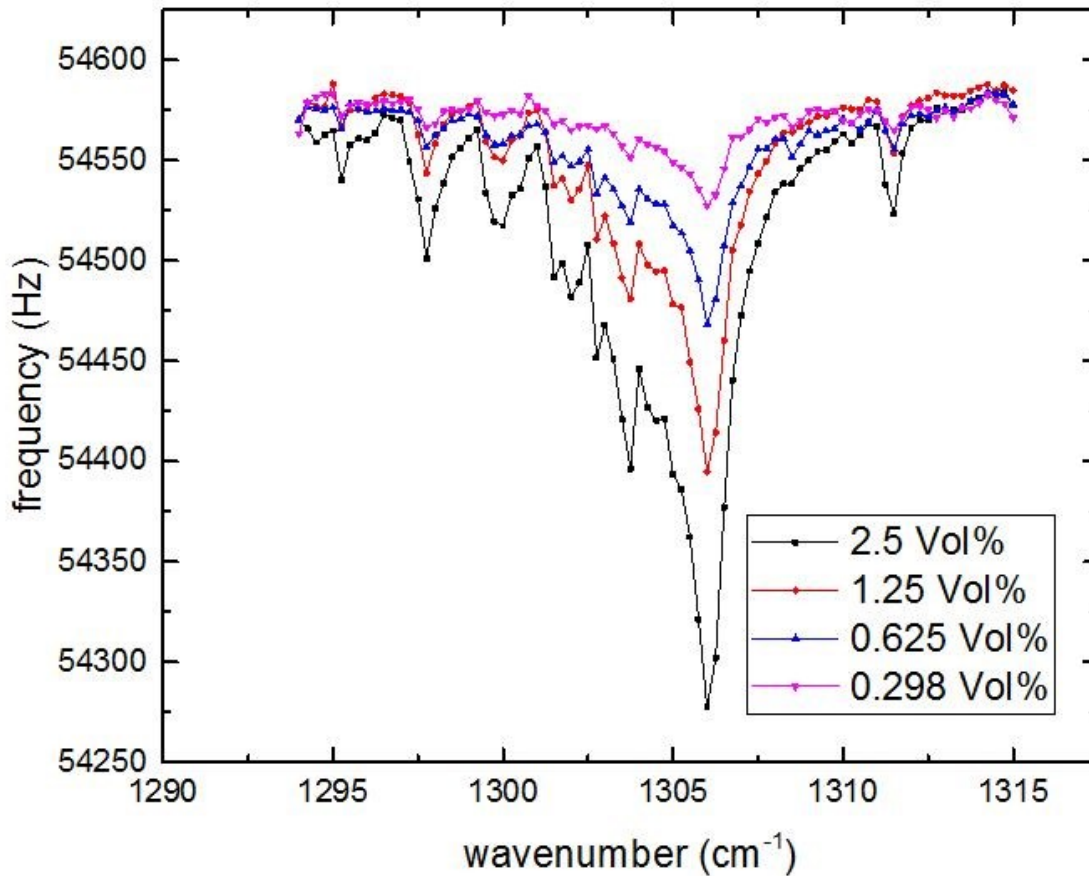


Figure 5.21. Short optical path frequency response of Silicon modified QTF for various concentrations of methane.

Methane concentrations were tested ranging from 2.5 Vol% down to 0.298 Vol% and the net shift in frequency below the background IR induced heating are shown in Figure 5.22 with error bars, and in Figure 5.23 without error bars for clarity. The calculated change in spring constant and temperature are shown in Figure 5.24 and Figure 5.25 respectively.

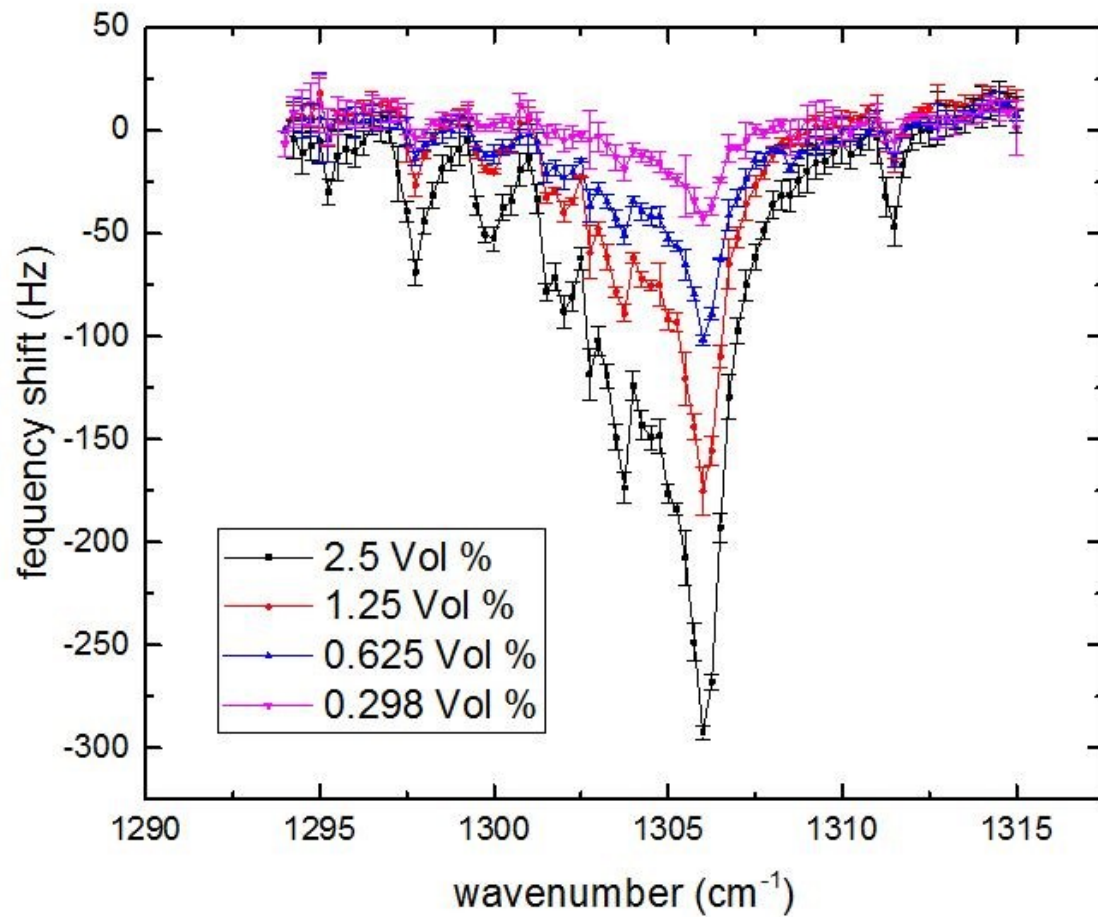


Figure 5.22. Measured frequency shift below the IR background for each wavenumber for various concentrations of methane gas. With error bars.

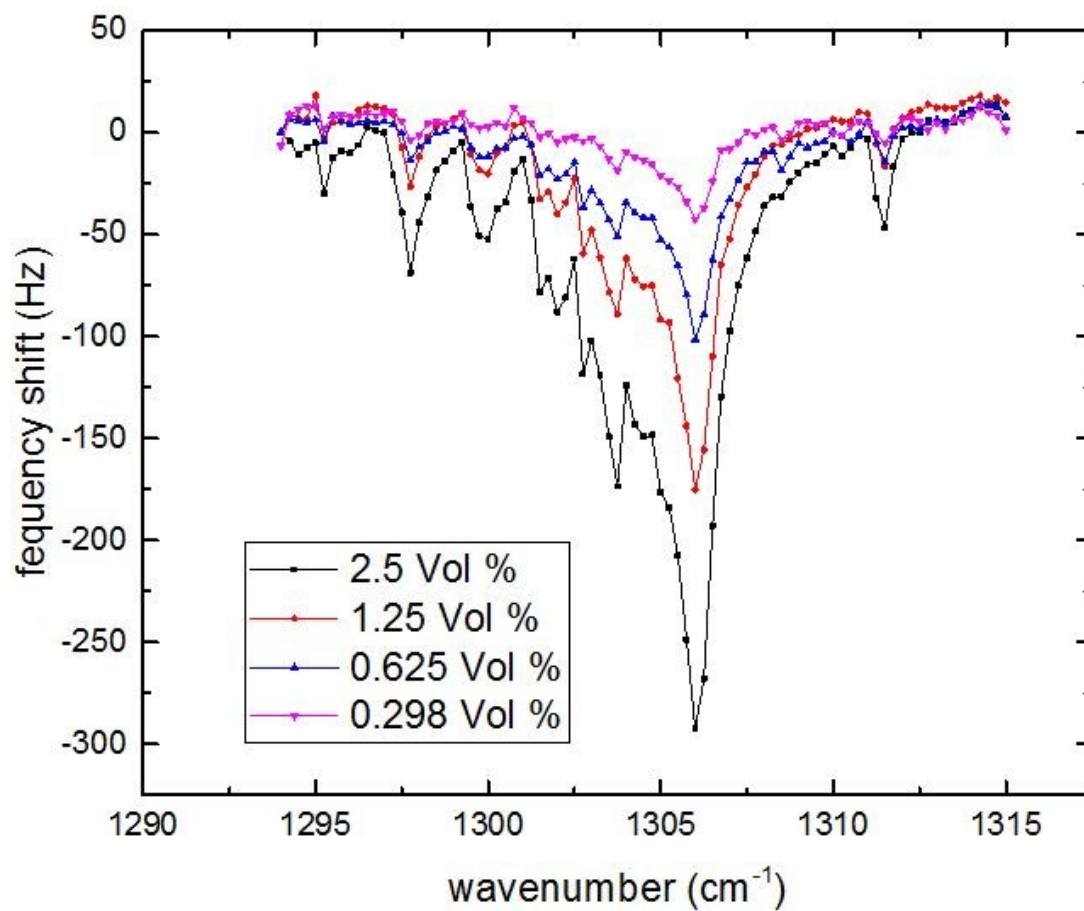


Figure 5.23. Measured frequency shift below the IR background for each wavenumber for various concentrations of methane gas. Without error bars for clarity.

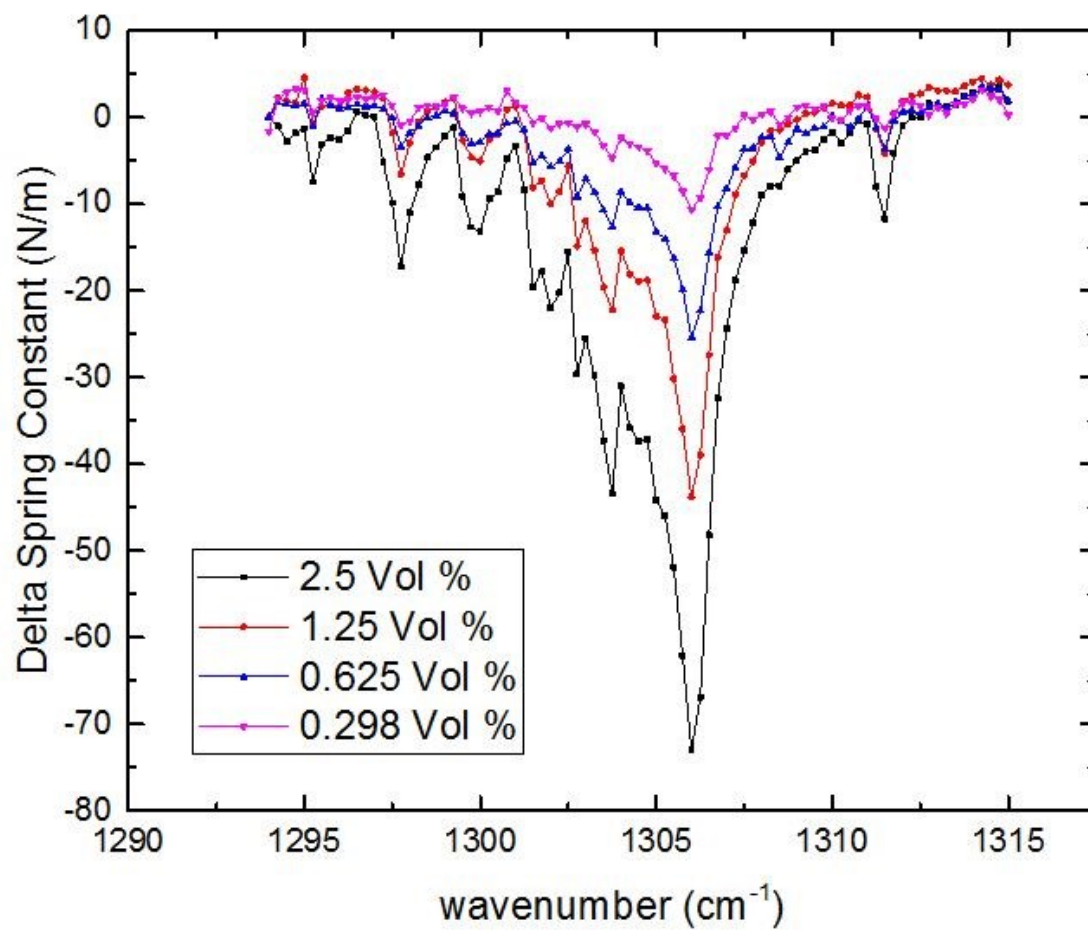


Figure 5.24. Change in spring constant of the bridging element for various concentrations of methane gas as a function of IR wavenumber.

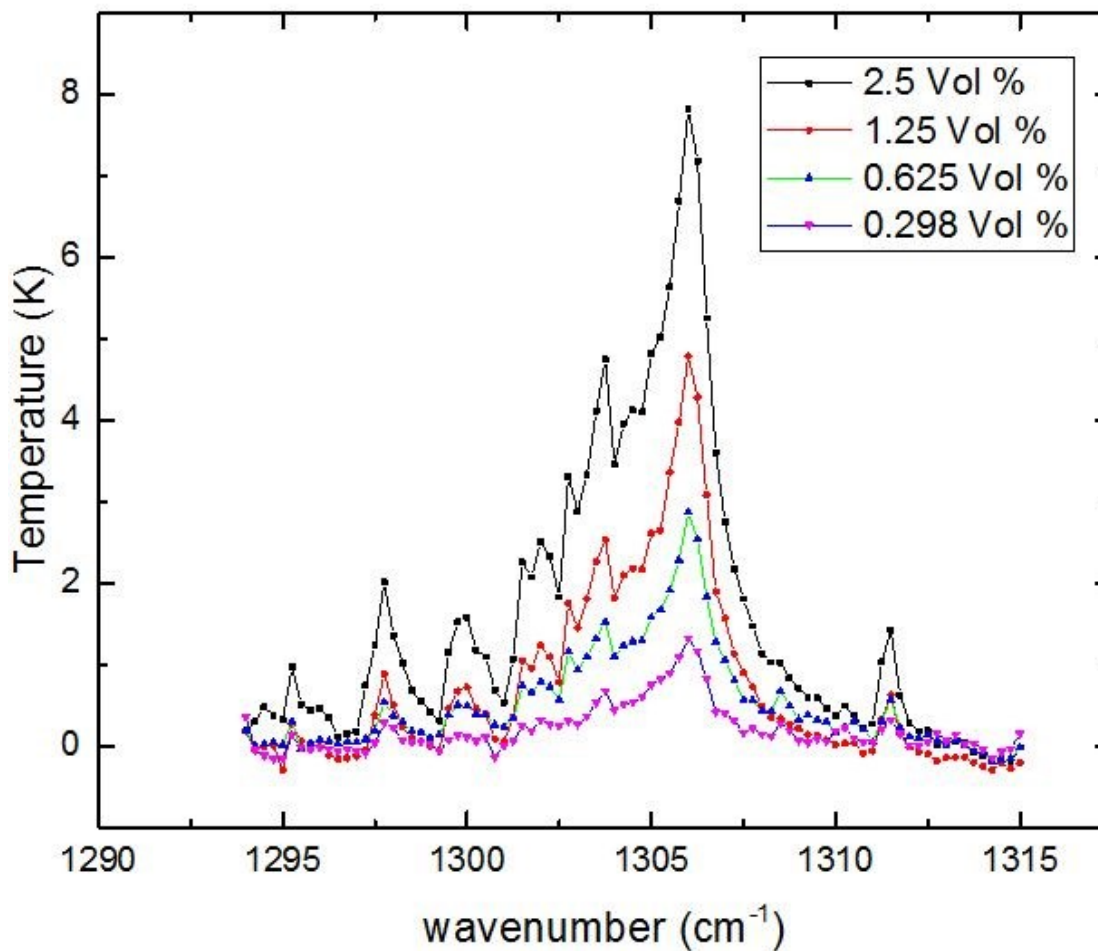


Figure 5.25. Change in temperature of the bridging element for various concentrations of methane gas as a function of IR wavenumber.

As can be observed by inspection of Figure 5.21, there is a net decrease in frequency response of the silicon bridge modified QTF indicative of the thermally induced stress causing a reduction in the spring constant of the bridging element due to heating from the vapor sample. This short path length is commensurate with the detection scheme employed by PCDS, as the optical path lengths employed therein are typically small, on the order of a few *mm*. Unsurprisingly, the results obtained by

Rahimi et al. are superior to those obtained using a silicon bridge modified QTF, employed in this configuration, as they utilized an optimal metal/substrate thickness ratio and employed a longer, clamped-free, cantilevered beam ($500\mu m$). However, these results reveal a simple means which could be employed in order to increase the lower limit of detection of PCDS, when investigating vapor phase samples, even further through judicious choice of experimental arrangement.

5.3. Akiyama probes

For the sake of completeness, Akiyama probes were also used to measure the IR spectrum of methane. The full ν_4 absorption line, to include the P, Q, and R branches, are shown in Figure 5.26, and the Q branch is shown in Figure 5.27. As there is no model applicable for this system, it can only be inferred that the net decrease in frequency indicates a net heating of the Akiyama probe. Of interest, though, is noting that the complete scan in Figure 5.26 took only twelve minutes to acquire and all of the scans were conducted at concentrations lower than that obtained by PCDS.

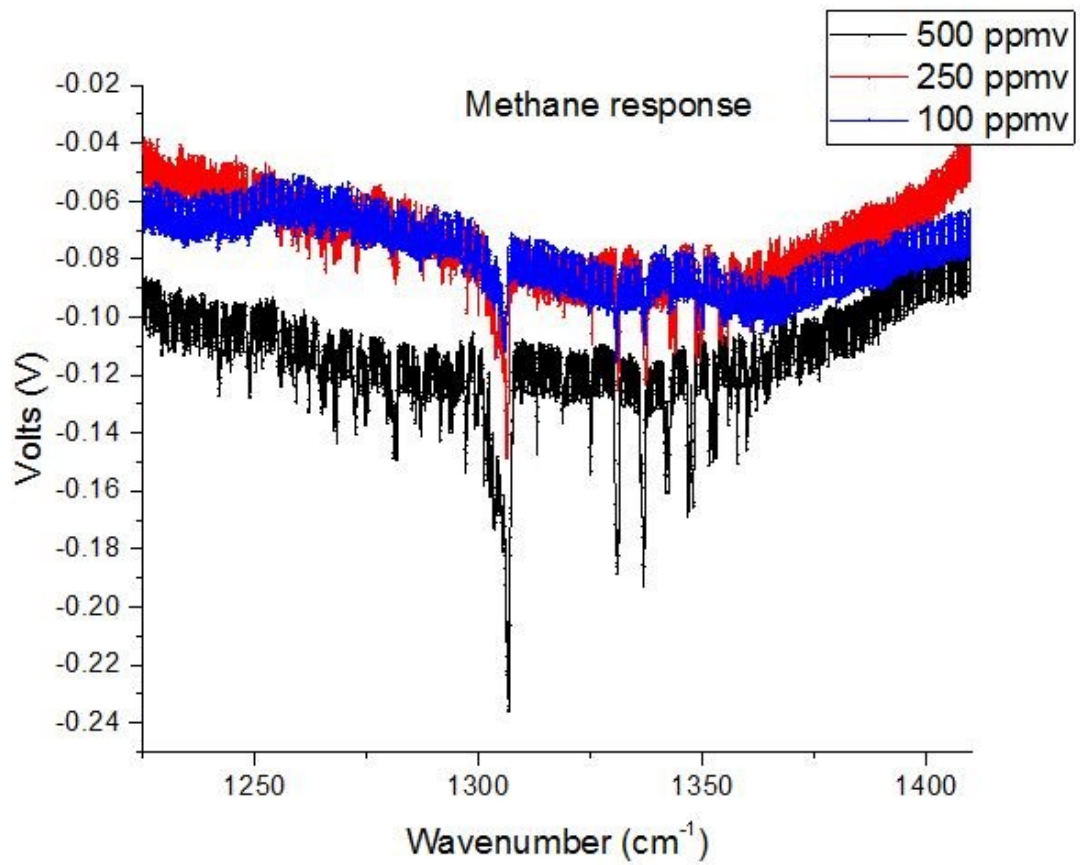


Figure 5.26. IR spectrum of P, Q, and R branch of the methane ν_4 absorption line as acquired using an Akiyama probe.

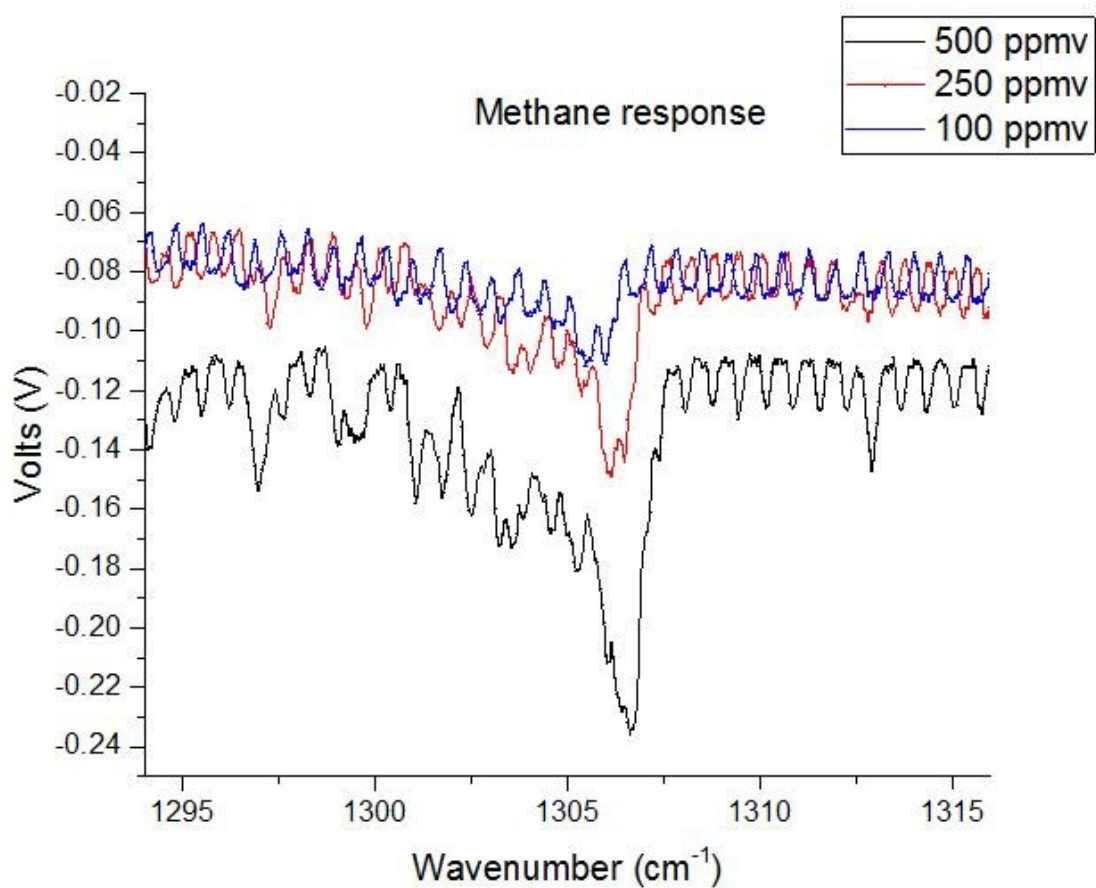


Figure 5.27. IR spectrum the Q branch of the methane ν_4 absorption line as acquired using an Akiyama probe

5.4. Potential improvement for PCDS

As PCDS operation depends on exploiting bimaterial beam deflection, it is apparent that IR illumination can be employed in one of two distinct arrangements, i.e. IR illumination directed towards the metal layer, or towards the substrate layer. When investigating solid materials applied directly onto the cantilevered beam, IR illumination and the sample under study must, obviously, be on the same side. This was demonstrated using PMMA on the gold side of the lever [22] and fluorescent latex spheres on the substrate side of the lever [23].

If vapor phase samples are studied however, the choice of which side is IR illuminated can possibly affect the limits of detection. Gold is typically chosen as the metallic coating for the bimetallic beams employed in PCDS due to its relative inertness and resistance to chemical corrosion [24]; however, the addition of a gold layer inhibits the penetration of IR into the body of the cantilevered beam due to the >99 % reflectivity of gold in the $2\ \mu\text{m}$ through $32\ \mu\text{m}$ wavelength regions [25]. If IR illumination were directed to the gold coated side, this would restrict the response of PCDS to the monitoring of the thermal rise in the local vicinity of the cantilevered beam due to the vapor sample's absorption of IR light.

If, however, IR illumination is directed to the cantilevered beam substrate, the results from the silicon bridge modified QTF indicate that it is possible to either monitor the local heating, when an optically short path length is chosen, or monitor the net

cooling of the beam, if a longer optical path is chosen. As can be observed from inspection of Figure 5.9 and Figure 5.21, PCDS has a greater thermal sensitivity than the silicon bridge modified QTF, thus implementing PCDS in a Beer-Lambert type arrangement should increase the lower limits of detection of the system.

5.5. References

1. C.P.S. Hsu, Chapter 15, *Handbook of Instrumental Techniques for Analytical Chemistry*, Frank Settle, Ed, Prentice Hall (1997)
2. D. Lee, S. Kim, I. Chae, S. Jeon, and T. Thundat, *Nanowell-Patterned TiO₂ Microcantilevers for Calorimetric Sensing*, Applied Physics Letters, 104, 141903 (2014)
3. A.R. Krause, C. Van Neste, L. Senesac, T. Thundat, and E. Finot, *Trace explosive detection using photothermal deflection spectroscopy*, Journal of Applied Physics, 103, 094906 (2008)
4. S. Kim, D. Lee, R. Thundat, M. Bagheri, S. Jeon, and T. Thundat, *Photothermal cantilever deflection spectroscopy*, ECS Transactions, 50 (12) 459-464 (2012)
5. M. Yun, S. Kim, D. Lee, N. Jung, I. Chae, S. Jeon, and T. Thundat, *Photothermal deflection spectroscopy of a photosensitive polymer*, Applied Physics Letters, 100, 204103 (2012)
6. M. Rahimi, I. Chae, J.E. Hawk, S.K. Mitra, and T. Thundat, *Methane sensing at room temperature using photothermal cantilever deflection spectroscopy*, Sensors and Actuators B:Chemical, 221 (2015) 564-569
7. A.G. Bell, *Upon the production of sound by radiant energy*, Philos. Mag. 11, 510 (1881)
8. J. Tyndall, *Action of an intermittent beam of radiant heat upon gaseous matter*, Proc. Roy. Soc. London 31,307 (1881)

9. W.C. Rontgen, *On tones produced by the intermittent irradiation of a gas*, Philos. Mag. 11, 308 (1881)
10. A.A. Kosterev, Yu. A. Bakhirkin, R.F. Curl, and F.K. Tittel, *Quartz-Enhanced Photoacoustic Spectroscopy*, Optics Letters, Vol 27 No 21, 1902-1904 (2002)
11. P. Patimisco, G. Scamarcio, F.K. Tittel, and V. Spagnolo, *Quartz-Enhanced Photoacoustic Spectroscopy: A Review*, Sensors, 14, 6165-6206 (2014)
12. Y. Ma, R. Lewicki, M. Razeghi, and F.K. Tittel, *QEPAS based ppb-level detection of CO and N₂O using a high power CW DFB-QCL*, Optics Express, Vol 21 No 1 (2013)
13. L. Dong, V. Spagnolo, R. Lewicki, and F.K. Tittel, *Ppb-level detection of nitric oxide using an external cavity quantum cascade laser based QEPAS sensor*, Optics Express, Vol 19 No 24 (2011)
14. Y. Ma, Y. He, Y. Tong, X. Yu, and F.K. Tittel, *Ppb-level detection of ammonia based on a power amplified laser and a low resonance frequency quartz tuning fork*, Optics Express, Vol 25 No 23 (2017)
15. Z. Wang, Q. Wang, J. Yuet-Ling Ching, J. Che-Yuen Wu, G. Zhang, and W. Ren, *A Portable low power QEPAS-based CO₂ isotope sensor using a fiber coupled interband cascade laser*, Sensors and Actuators B: Chemical, 246 pg 710-715 (2017)
16. S. Schilt, A.A. Kosterev, and F.K. Tittel, *Performance evaluation of a near infrared QEPAS based ethylene sensor*, Applied Physics B, 95 813-824 (2009)

17. C.W. Van Neste, L.R. Senesac, and T. Thundat, *Standoff photoacoustic spectroscopy*, Applied Physics Letters, 92, 234102 (2008)
18. C.W. Van Neste, L.R. Senesac, and T. Thundat, *Standoff Spectroscopy of Surface Absorbed Chemicals*, Anal. Chem, 81, 1952-1956 (2009)
19. C.W. Van Neste, M.E. Morales-Rodriguez, L.R. Senesac, S.M. Mahajan, and T. Thundat, *Quartz crystal tuning fork photoacoustic point sensing*, Sensors and Actuators B: Chemical, 150, 402-405 (2010)
20. M.E. Morales-Rodriguez, C.W. Van Neste, L.R. Senesac, S.M. Mahajan, and T. Thundat, *Ultra Violet Decomposition of Surface Adsorbed Explosives Investigated with Infrared Standoff Spectroscopy*, Sensors and Actuators B: Chemical, 161, 961-966 (2012)
21. F. Tsow and N.J. Tao, *Microfabricated tuning fork temperature and infrared sensor*, Applied Physics Letters, 90, 174102, (2007)
22. M. Yun, S. Kim, D. Lee, Namchul Jung, I. Chae, S. Jeon, and T. Thundat, *Photothermal cantilever deflection spectroscopy of a photosensitive polymer*, Applied Physics Letters, 100, 204103 (2012)
23. J.R. Barnes, R.J. Stephenson, C. N. Woodburn, S. J. O'Shea, M.E. Welland, T. Rayment, J.K. Gimzewski, and Ch. Gerber, *A femtojoule calorimeter using micromechanical sensors*, Review of Scientific Instruments, 65, 3793, (1994)
24. H. Hieber and K. Pape, *Ageing of Thin Gold Films*, Gold Bulletin, 15, 3, 90-100, (1982)

25. J. M. Bennett and E. J. Ashley, *Infrared Reflectance and Emittance of Silver and Gold Evaporated in Ultrahigh Vacuum*, NAVWEPS Report 8752, U.S. Naval Ordnance Test Station, China Lake, CA (1965)

Chapter 6: Conclusion

In this work, a distributed beam model has been investigated to monitor optically mediated thermal variations in silicon bridging elements affixed to the terminal ends of a quartz tuning fork. Whether this heating is incurred directly or indirectly, the model investigated appears to yield viable results. The results here clearly indicate that a new paradigm is achievable, where, rather than monitoring axial stress in soft polymers, it is possible to use larger, more rigid, elements allowing for a significantly greater responsive area.

Further, the model investigated is valid for a larger range of terminal attachment stiffness changes than the heretofore used point-mass Hookean model. Investigation of this model, as well as closer inspection of the point-mass model, has allowed for speculation of a simple means to improve sensor responsivity of simple polymer stranded systems. The attachment of multiple polymer stands in parallel between the QTF tines would act as a simple mechanical gain, allowing for a reduction in the lower limits of detection. This method, coupled with the previously disclosed methodologies, could enhance the utility of this simple and robust platform.

The system employed also demonstrates a means to exploit thermal variance for a greatly simplified system to monitor infrared fingerprints and airborne chemical species. Of the compared techniques (QEPAS, and Standoff photoacoustic), each of these systems requires modulation of the light source at the resonance frequency, or some fraction thereof, of the QTF in order to actively drive the fork into resonance. Indeed, both of these approaches show an inverse relationship between sensor response and

QTF frequency. This new, more simplified approach removes the restriction for the modulation rate of the laser source, as well as revealing a proportional relationship between sensor response and QTF frequency.

The modified QTFs used in this study have also demonstrated lower levels of detection over those reported using PCDS, with the unmodified Akiyama probe yielding even lower levels of detection than either the silicon bridge modified QTF or PCDS while simultaneously demonstrating a much faster scan time than PCDS. Investigations of variable optical path length also reveal a potential means to increase the lower limits of detection of PCDS by exploiting the Beer-Lambert relation rather than direct monitoring of the local heat variance due to IR absorption.

Chapter 7: Future work

One of the unrealized goals of this current work was to demonstrate the capability of this system to be used in a standoff detection scheme. To this end, carbon nanotubes were thermally grown onto silicon bridging elements for use as a broadband IR detector to enable the system to operate in a fashion similar to that of Standoff Photoacoustic, i.e. monitor the inverse of a typical IR spectrum. Unfortunately, of the ten devices fabricated, none would properly resonate. The current hypothesis is that the attachment of the silicon bridging element resulted in a straight element that did not properly allow for the “out-of-plane” oscillation required. In short, the lateral spring constant was too great to allow for oscillation of the tines. Either improved bridging design or attachment methodologies should enable full device operation.

As was discussed in chapter 4, rather than restricting the device to primarily monitoring thermally induced stress changes, it should also be possible to monitor the photo-induced stress, i.e. the generation of excess charge carriers when the photon energy is equal to, or greater than, the band-gap of the bridging element. Arrangements are currently underway to investigate the behavior of this response to allow for true bolometric response of the system.

Previous studies using microfabricated microcantilever beams have demonstrated that surface stress changes can manifest as changes in the spring constant of the beam. Of the systems investigated thus far, Na^+ ions interacting with a SiN beam have demonstrated an increase in the stiffness of the beam increasing the resonance frequency of the structure by up to 1.3 kHz. It would be interesting to see if a similar

response could be monitored using this modified QTF structure. It is expected; however, that the nature of the interaction would need to be chemisorption rather than physisorption due to the strength of such interactions, this would unfortunately preclude reversibility of the response.

References

Chapter 1

1. G. Binnig, C.F. Quate, and Ch. Gerber, *Atomic Force Microscope*, Phys Rev Lett, Vol 56 number 9 pg 930-933 (1986).
2. G. Meyer, N M. Amer, *Erratum: Novel optical approach to atomic force microscopy*, Appl. Phys. Lett. 53, 1045 (1988), Appl Phys Lett, 53(24) 12, (1988) pg 2400-2402.
3. P. Gunther, U. Ch. Fischer, and K. Dransfield, *Scanning Near-Field Acoustic Microscopy*, Applied Physics B, 48, 89-92 (1989).
4. K. Karrai and R. Grober, *Piezoelectric tip-sample distance control for near field optical microscopes*, Appl Phys Lett, 66 (14) pg 1842-1844 (1995).
5. T.R. Albrecht, P. Grutter, D. Horne, and D. Rugar, *Frequency modulation detection using high-Q cantilevers for enhanced force microscopy sensitivity*, J. Appl. Phys, 69 (2) (1991)
6. H. Edwards, L. Taylor, and W. Duncan, *Fast, high-resolution atomic force microscopy using a quartz tuning fork as actuator and sensor*, J. Appl. Phys., 82 (3), (1997).
7. Frenz J. Giessibl, *High-speed force sensor for microscopy and profilometry utilizing a quartz tuning fork*, Appl Phys Lett, Volume 73 number 26, 3956-3958 (1998).
8. T. Akiyama, U. Staufer, and N.F.de Rooij, *Self-sensing and self-actuating probe based on quartz tuning fork combined with microfabricated cantilever for*

- dynamic mode atomic force microscopy*, Applied Surface Science, 210 (2003) 18-21.
9. P.J. Shaver, *Bimetal Strip Hydrogen Gas Detectors*, Rev. Sci. Instr., 40, 901-905 (1969).
 10. E.H. Taylor, W.C. Waggener, *Measurement of Adsorption Forces*, J. Phys. Chem., 83: 1361-1362 (1979).
 11. R.V. Jones, *The Detection of Thermal Radiation Using Linear Expansion*, Proceedings of the Royal Society of London. Series A, Mathematical and Physical Sciences, 249: 100 (1959).
 12. L.A. Pinnaduwege, V. Boiadjiev, J.E. Hawk, and T. Thundat, *Sensitive detection of plastic explosives with self-assembled monolayer-coated microcantilevers*, Applied Physics Letters 83 (7) 1471-1473 (2003).
 13. L.A. Pinnaduwege, J.E. Hawk, V. Boiadjiev, and T. Thundat, *Use of Microcantilevers for the Monitoring of Molecular Binding to Self-Assembled Monolayers*, Langmuir 19 (19) 7841-7844 (2003).
 14. L.A. Pinnaduwege, T. Thundat, J.E. Hawk, D.L. Hedden, P.F. Britt, E.J. Houser, S. Stepnowski, R.A. McGill, D. Bubb, *Detection of 2,4-dinitrotoluene using microcantilevers*, Sensors and Actuators B: Chemical, 99 (2-3) 223-229 (2004).
 15. M. Rahimi, I. Chae, J.E. Hawk, S.K. Mitra, T. Thundat, *Methane sensing at room temperature using photothermal cantilever deflection spectroscopy*, Sensors and Actuators B: Chemical, 221, 564-569 (2015).
 16. Y. Deng, C. Chen, X. Qin, X. Xian, T.L. Alford, H. W. Choi, F. Tsow, and E.S. Forzani, *Aging effect of a molecularly imprinted polymer on a quartz tuning fork*

- for detection of volatile organic compounds*, Sensors and Actuators B: Chemical, 211 (2015) 25-32.
17. Y. Deng, N. Liu, F. Tsow, X. Xian, and E. Forzani, *Adsorption Thermodynamic Analysis of a Quartz Tuning Fork Based Sensor for Volatile Organic Compounds Detection*, ACS Sensors, 2 (2017) 1662-1668.
 18. S. Boussaad and N.J. Tao, *Polymer Wire Chemical Sensor Using a Microfabricated Tuning Fork*, NanoLetters, Vol 3 No 8, 1173-1176 (2003).
 19. M. Ren, E.S. Forzani, and N. Tao, *Chemical Sensor Based on Microfabricated Wristwatch Tuning Forks*, Anal. Chem., 77, 2700-2707 (2005).
 20. F. Tsow, N. Tao, *Microfabricated Tuning Fork Temperature and Infrared Sensor*, Applied Physics Letters, 90, 174102 (2007).
 21. F. Tsow, E.S. Forzani, and N.J. Tao, *Frequency-Coded Chemical Sensors*, Anal. Chem., 80, 606-611 (2008).
 22. F. Tsow, E. Forzani, A. Rai, R. Wang, R. Tsui, S. Mastroianni, C. Knobbe, A.J. Gandolfi, and N.J. Tao, *A Wearable and Wireless Sensor System for Real-Time Monitoring of Toxic Environmental Volatile Organic Compounds*, IEEE Sensors Journal, Vol 9, No 12, (2009).
 23. R. Wang, F. Tsow, X. Zhang, J. Peng, E.S. Forzani, Y. Chen, J.C. Crittenden, H. Destailats, and N. Tao, *Real-Time Ozone Detection Based on a Microfabricated Quartz Crystal Tuning Fork Sensor*, Sensors, 9, 5655-5663 (2009).
 24. A. Rai, F. Tsow, S. Nassirpour, J. Bankers, M. Spinatsch, M.P. He, E.S. Forzani, and N.J. Tao, *Selective detection of sulfur derivatives using microfabricated*

- tuning fork-based sensors*, Sensors and Actuators B: Chemical, 140, (2009) 490-499.
25. M. Yun, S. Lee, C. Yim, N. Jung, T. Thundat, and S. Jeon, *Suspended polymer nanobridge on a quartz resonator*, Applied Physics Letters, 103, 053109 (2013).
26. S. Lee, M. Yun, S. Jeon, *A tunable microresonator sensor based on a photocrosslinking polymer nanowire*, Applied Physics Letters, 104, 053506 (2014).
27. M. Yun, E. Lee, K. Cho, and S. Jeon, *Enhanced sensitivity of a microfabricated resonator using a graphene-polystyrene bilayer membrane*, Applied Physics Letters, 105, 173116 (2014).
28. S. Hwang, W. Kim, H. Yoon, and S. Jeon, *Performance Enhancement of a Microfabricated Resonator Using Electrospun Nanoporous Polymer Wire*, ACS Sensors, (2017) 2, 1355-1358.
29. S.A. Sampson, K.S. Date, S.V. Panchal, A. Ambrale, and S.S. Datar, *Investigation of QTF based gas sensors*, Sensors and Actuators B: Chemical, 216 (2015) 586-594.
30. S.A. Sampson, S.V. Panchal, K.S. Date and S.S. Datar, *QTF Based Methanol Sensors*, Proceedings of the 2015 2nd International Symposium on Physics and Technology of Sensors, 8-10th March, 2015, Pune, India.
31. S.A. Sampson, S.V. Panchal, A. Mishra, S. Banerjee, and S.S. Datar, *Quartz tuning fork based portable sensor for vapor phase detection of ethanol by using aniline-doped microwires*, Microchim Acta, (2017) 184, 1659-1667.

Chapter 2

1. S. Boussaad and N.J. Tao, *Polymer wire chemical sensor using a microfabricated tuning fork*, NanoLetters, Vol 3 No 8 , 1173-1176 (2003).
2. M. Yun, S. Lee, C. Yim, N. Jung, T. Thundat, and S. Jeon, *Suspended polymer nanobridge on a quartz resonator*, Applied Physics Letters, 103, 053109 (2013).
3. J.A. Turner, S. Hirsekorn, U. Rabe, W. Arnold, *High-frequency response of atomic-force microscope cantilevers*, J Appl Phys, 82:966 (1997).
4. S.P. Timoshenko, *On the correction factor for shear of the differential equation for transverse vibrations of bars of uniform cross-section*, Philosophical Magazine, p. 744 (1921).
5. S.P. Timoshenko, *On the transverse vibrations of bars of uniform cross-section*, Philosophical Magazine, p. 125 (1922).
6. S.P. Timoshenko, *History of strength of materials*, McGraw-Hill New York (1953).
7. S.M. Han, H. Benaroya and T. Wei, *Dynamics of transversely vibrating beams using four engineering theories*, Journal of Sound and Vibration, 225(5), 935-988 (1999).
8. W.D. Means, *Hookean Behavior. In: Stress and Strain*. Springer, New York, NY (1976).
9. J. Melcher, J. Stirling, and G. Shaw, *A simple method for the determination of qPlus sensor spring constants*, Beilstein Journal of Nanotechnology, 6, 1733-1742 (2015)

10. F. J. Giessibl, *Forces and frequency shifts in atomic-resolution dynamic-force microscopy*, Physical Review B, Vol 56, number 24, 16010-16015 (1997)
11. Y. Lei, T. Murmu, M.I. Friswell, *Dynamic characteristics of damped viscoelastic nonlocal Euler-Bernoulli beams*, European Journal of Mechanics A/Solids, 42, 125-136 (2013)
12. E. Volterra, E.C. Zachmanoglou, *Dynamics of Vibrations*, Charles E. Merrill Books Inc, Columbus, Ohio, 1965.
13. W. Weaver, S.P. Timoshenko, D.H. Young, *Vibration Problems in Engineering*, John Wiley, New York (1990).
14. F.W. Stokey, *Vibration of Systems Having Distributed Mass and Elasticity*. In: *Harris CM, Crede CE (eds) Shock and Vibration Handbook*, McGraw-Hill, New York, Chapter 7 (1976).
15. T. Thundat, E.A. Wachter, S.L. Sharp, R.J. Warmack, *Detection of Mercury Vapor Using Resonating Microcantilevers*, Appl Phys Lett, 66, 1695 (1995)
16. M.J. Madou, *Fundamentals of Microfabrication: The Science of Miniaturization*, Second Edition, CRC Press, (1997).
17. G.Y. Chen, T. Thundat, E.A. Wachter, and R.J. Warmack, *Adsorption-Induced Surface Stress and Its Effects on Resonance Frequency of Cantilevers*, J. Appl. Phys., vol. 77, pp. 3618-3622, (1995).
18. K. Yamanaka and S. Nakano, *Ultrasonic atomic force microscope with overtone excitation*, Jpn J Appl Phys, 35, 3787 (1996).

19. U. Rabe, K. Janser, and W. Arnold, *Vibrations of free and surface-coupled atomic force microscope cantilevers: Theory and experiment*, Rev Sci Instr 67, 3281 (1996).
20. J.A. Turner and J.S. Wiehn, *Sensitivity of flexural and torsional vibration modes of atomic force microscope cantilevers to surface stiffness variations*, Nanotechnology 12, 322 (2001).

Chapter 3

1. T. Akiyama, U. Staufer, and N.F. de Rooij, *Self-sensing and self-actuating probe based on quartz tuning fork combined with microfabricated cantilever for dynamic mode atomic force microscopy*, Applied Surface Science, 210 (2003) 18-21
2. S. Stucklin, M.R. Gullo, T. Akiyama, M. Schneidiger, *Atomic Force Microscopy for Industry with the Akiyama-Probe System*, International Conference on Nanoscience and nanotechnology (ICONN), (2008)
3. T. Akiyama, U. Staufer, and N.F. Rooij, *Symmetrically arranged quartz tuning fork with soft cantilever for intermittent contact mode atomic force microscopy*, Review of Scientific Instruments, Vol 74, No 1, 112-117 (2003)
4. P. Datskos, S. Rajic, and I. Datskou, *Photoinduced and thermal stress in silicon microcantilevers*, Applied Physics Letters, Vol 73, No 16, 2319-2321, (1998)
5. J. Melcher, J. Stirling, and G. Shaw, *A simple method for the determination of qPlus sensor spring constants*, Beilstein Journal of Nanotechnology, 6, 1733-1742 (2015)

Chapter 4

1. S.P. Timoshenko, *History of strength of materials*, McGraw-Hill New York (1953).
2. H. Watanabe, N. Yumada, and M. Okija, *Linear Thermal Expansion Coefficient of Silicon from 293 to 1000 K*, *International Journal of Thermophysics*, **25** (2004) 221
3. C. Cho, *Characterization of Young's Modulus of Silicon Versus Temperature using a "Beam Deflection" Method with a Four-Point Bending Fixture*, *Current Applied Physics*, **9** (2009) 538-545
4. R.G. Stearns and G.S. Kino, *Effect of electronic strain on photoacoustic generation in silicon*, *Applied Physics Letters*, 47, 10 (1985)
5. P. Datskos, S. Rajic, and I. Datskou, *Photoinduced and thermal stress in silicon microcantilevers*, *Applied Physics Letters*, Vol 73, No 16, 2319-2321, (1998)
6. R.C. Weast, *Handbook of Chemistry and Physics*, 59th ed. Chemical Rubber Company, Boca Raton, FL (1972)
7. A.E. Burgess, *The Rose model, revisited*, *J. Opt. Soc. Am. A*, Vol 16, No 3, 633-646 (1999)
8. F. Tsow, N. Tao, *Microfabricated Tuning Fork Temperature and Infrared Sensor*, *Applied Physics Letters*, 90, 174102 (2007)
9. S. Akhbari, F. Sammoura, C. Yang, A. Heidari, D. Horsely, and L. Lin, *Self-Curved Diaphragms by Stress Engineering for Highly Responsive PMUT*, 28th IEEE international Conference on Micro Electro Mechanical Systems, (2015) 837-840)

Chapter 5

1. C.P.S. Hsu, Chapter 15, *Handbook of Instrumental Techniques for Analytical Chemistry*, Frank Settle, Ed, Prentice Hall (1997)
2. D. Lee, S. Kim, I. Chae, S. Jeon, and T. Thundat, *Nanowell-Patterned TiO₂ Microcantilevers for Calorimetric Sensing*, Applied Physics Letters, 104, 141903 (2014)
3. A.R. Krause, C. Van Neste, L. Senesac, T. Thundat, and E. Finot, *Trace explosive detection using photothermal deflection spectroscopy*, Journal of Applied Physics, 103, 094906 (2008)
4. S. Kim, D. Lee, R. Thundat, M. Bagheri, S. Jeon, and T. Thundat, *Photothermal cantilever deflection spectroscopy*, ECS Transactions, 50 (12) 459-464 (2012)
5. M. Yun, S. Kim, D. Lee, N. Jung, I. Chae, S. Jeon, and T. Thundat, *Photothermal deflection spectroscopy of a photosensitive polymer*, Applied Physics Letters, 100, 204103 (2012)
6. M. Rahimi, I. Chae, J.E. Hawk, S.K. Mitra, and T. Thundat, *Methane sensing at room temperature using photothermal cantilever deflection spectroscopy*, Sensors and Actuators B:Chemical, 221 (2015) 564-569
7. A.G. Bell, *Upon the production of sound by radiant energy*, Philos. Mag. 11, 510 (1881)
8. J. Tyndall, *Action of an intermittent beam of radiant heat upon gaseous matter*, Proc. Roy. Soc. London 31,307 (1881)
9. W.C. Rontgen, *On tones produced by the intermittent irradiation of a gas*, Philos. Mag. 11, 308 (1881)

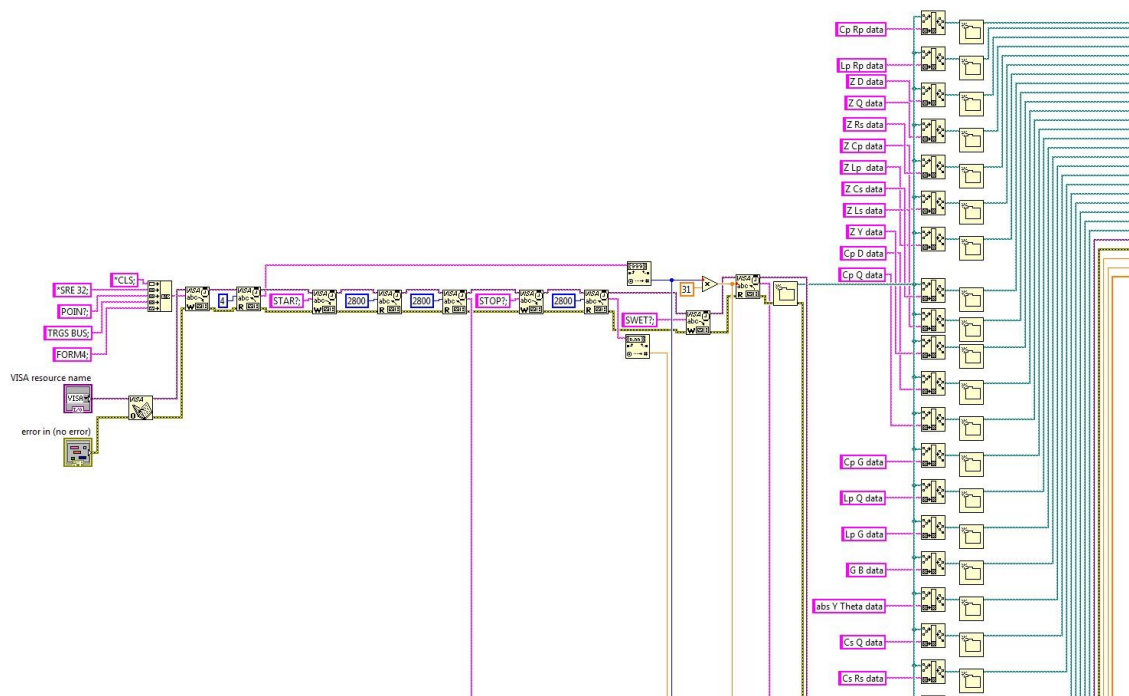
10. A.A. Kosterev, Yu. A. Bakhrkin, R.F. Curl, and F.K. Tittel, *Quartz-Enhanced Photoacoustic Spectroscopy*, Optics Letters, Vol 27 No 21, 1902-1904 (2002)
11. P. Patimisco, G. Scamarcio, F.K. Tittel, and V. Spagnolo, *Quartz-Enhanced Photoacoustic Spectroscopy: A Review*, Sensors, 14, 6165-6206 (2014)
12. Y. Ma, R. Lewicki, M. Razeghi, and F.K. Tittel, *QEPAS based ppb-level detection of CO and N₂O using a high power CW DFB-QCL*, Optics Express, Vol 21 No 1 (2013)
13. L. Dong, V. Spagnolo, R. Lewicki, and F.K. Tittel, *Ppb-level detection of nitric oxide using an external cavity quantum cascade laser based QEPAS sensor*, Optics Express, Vol 19 No 24 (2011)
14. Y. Ma, Y. He, Y. Tong, X. Yu, and F.K. Tittel, *Ppb-level detection of ammonia based on a power amplified laser and a low resonance frequency quartz tuning fork*, Optics Express, Vol 25 No 23 (2017)
15. Z. Wang, Q. Wang, J. Yuet-Ling Ching, J. Che-Yuen Wu, G. Zhang, and W. Ren, *A Portable low power QEPAS-based CO₂ isotope sensor using a fiber coupled interband cascade laser*, Sensors and Actuators B: Chemical, 246 pg 710-715 (2017)
16. S. Schilt, A.A. Kosterev, and F.K. Tittel, *Performance evaluation of a near infrared QEPAS based ethylene sensor*, Applied Physics B, 95 813-824 (2009)
17. C.W. Van Neste, L.R. Senesac, and T. Thundat, *Standoff photoacoustic spectroscopy*, Applied Physics Letters, 92, 234102 (2008)
18. C.W. Van Neste, L.R. Senesac, and T. Thundat, *Standoff Spectroscopy of Surface Absorbed Chemicals*, Anal. Chem, 81, 1952-1956 (2009)

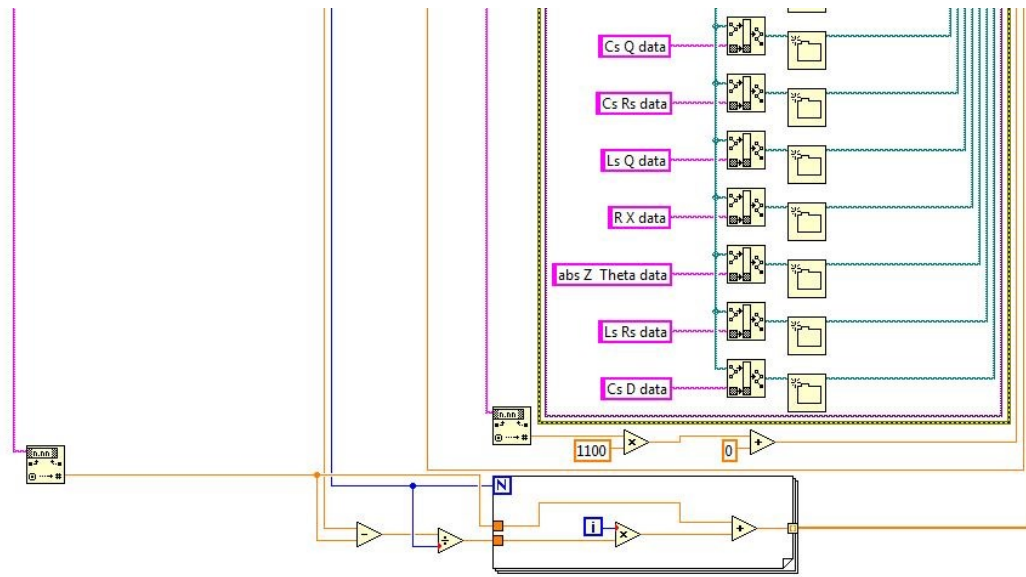
19. C.W. Van Neste, M.E. Morales-Rodriguez, L.R. Senesac, S.M. Mahajan, and T. Thundat, *Quartz crystal tuning fork photoacoustic point sensing*, Sensors and Actuators B: Chemical, 150, 402-405 (2010)
20. M.E. Morales-Rodriguez, C.W. Van Neste, L.R. Senesac, S.M. Mahajan, and T. Thundat, *Ultra Violet Decomposition of Surface Adsorbed Explosives Investigated with Infrared Standoff Spectroscopy*, Sensors and Actuators B: Chemical, 161, 961-966 (2012)
21. F. Tsow and N.J. Tao, *Microfabricated tuning fork temperature and infrared sensor*, Applied Physics Letters, 90, 174102, (2007)
22. M. Yun, S. Kim, D. Lee, Namchul Jung, I. Chae, S. Jeon, and T. Thundat, *Photothermal cantilever deflection spectroscopy of a photosensitive polymer*, Applied Physics Letters, 100, 204103 (2012)
23. J.R. Barnes, R.J. Stephenson, C. N. Woodburn, S. J. O'Shea, M.E. Welland, T. Rayment, J.K. Gimzewski, and Ch. Gerber, *A femtojoule calorimeter using micromechanical sensors*, Review of Scientific Instruments, 65, 3793, (1994)
24. H. Hieber and K. Pape, *Ageing of Thin Gold Films*, Gold Bulletin, 15, 3, 90-100, (1982)
25. J. M. Bennett and E. J. Ashley, *Infrared Reflectance and Emittance of Silver and Gold Evaporated in Ultrahigh Vacuum*, NAVWEPS Report 8752, U.S. Naval Ordnance Test Station, China Lake, CA (1965)

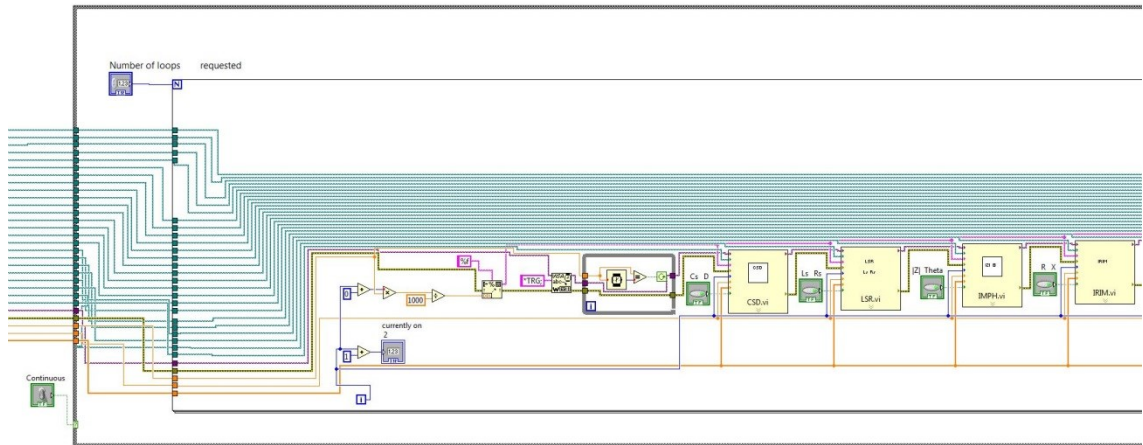
Appendix

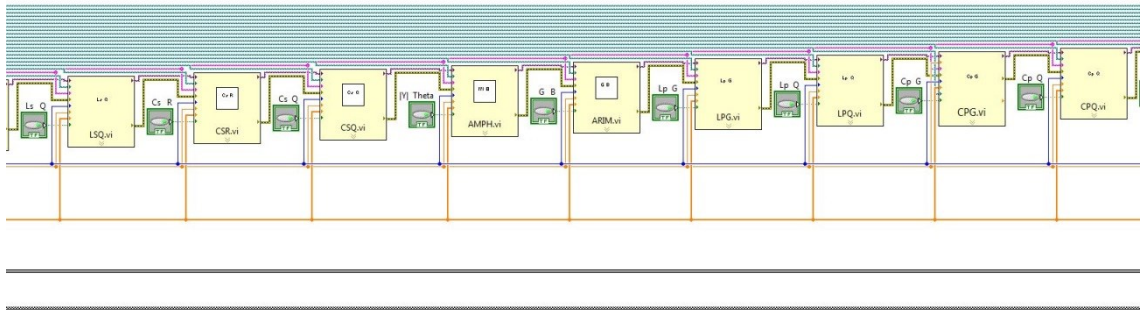
LabView computer code was written by the author to facilitate ease of control and data acquisition for a variety of devices during the course of experimentation. The code for each device is presented below. The author also wrote Matlab code for modelling and other calculations, as presented below.

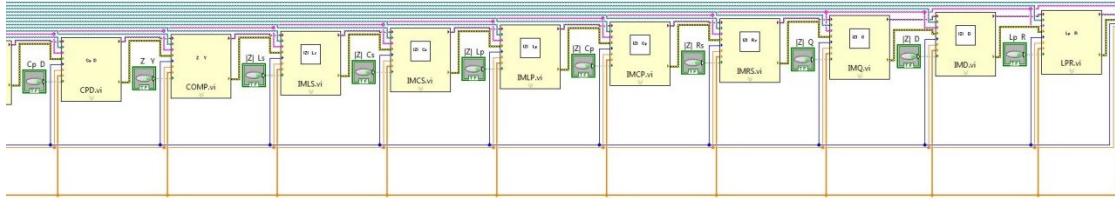
Agilent 4294A Impedance Analyzer

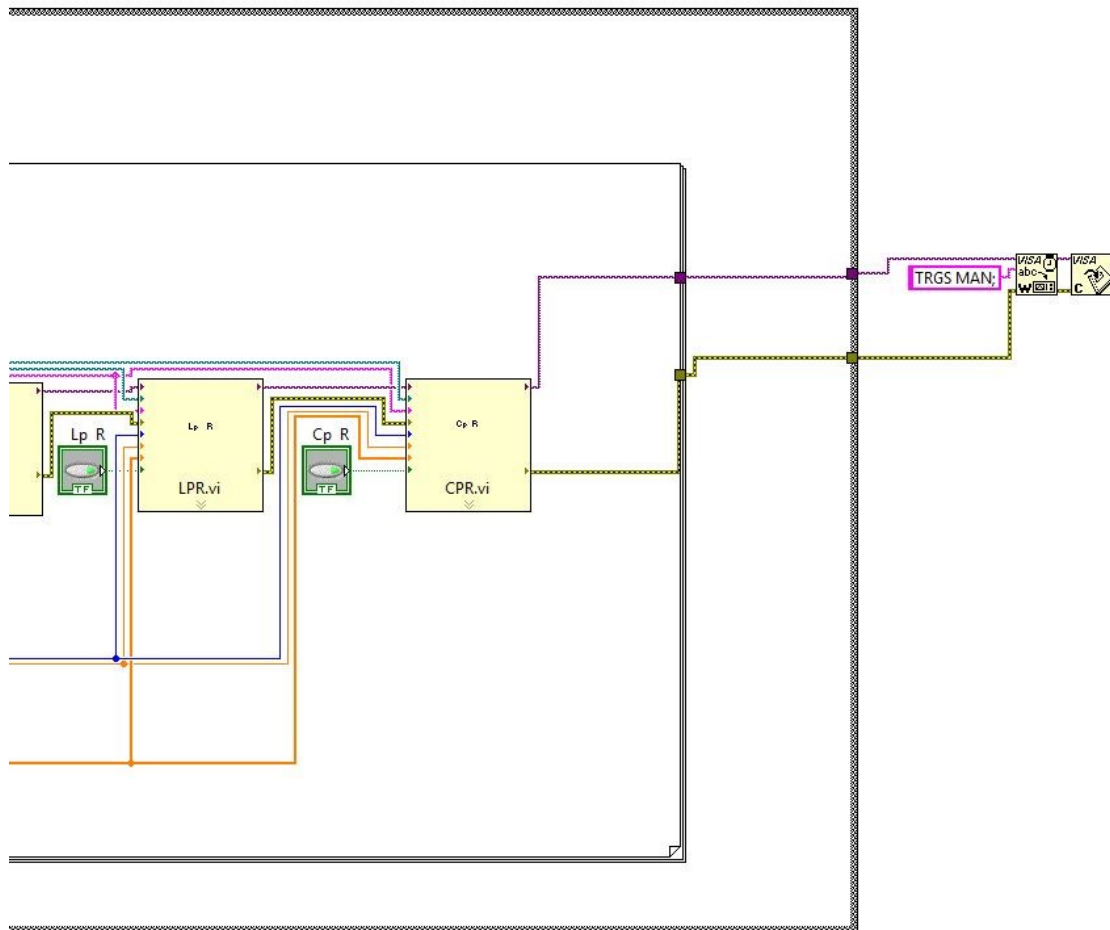


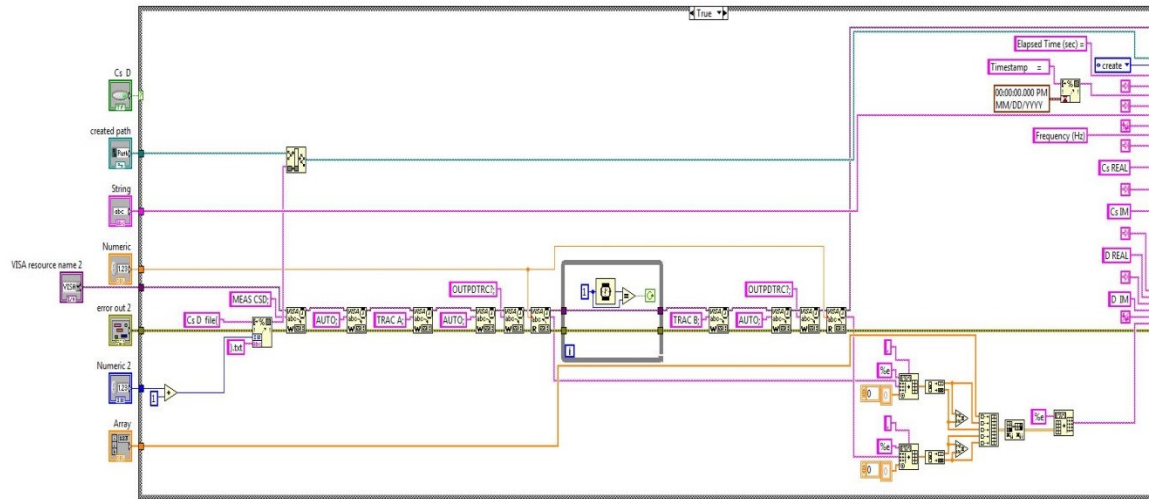


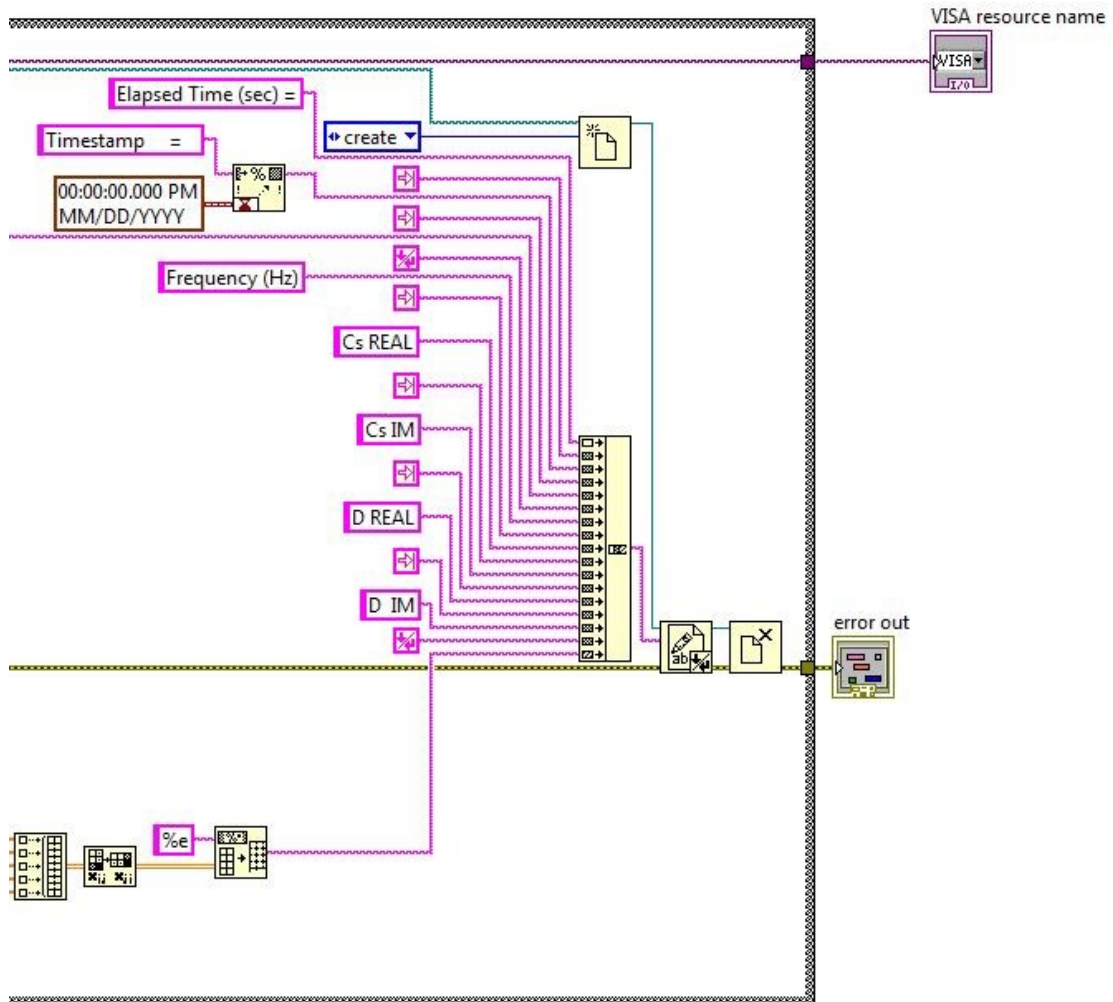


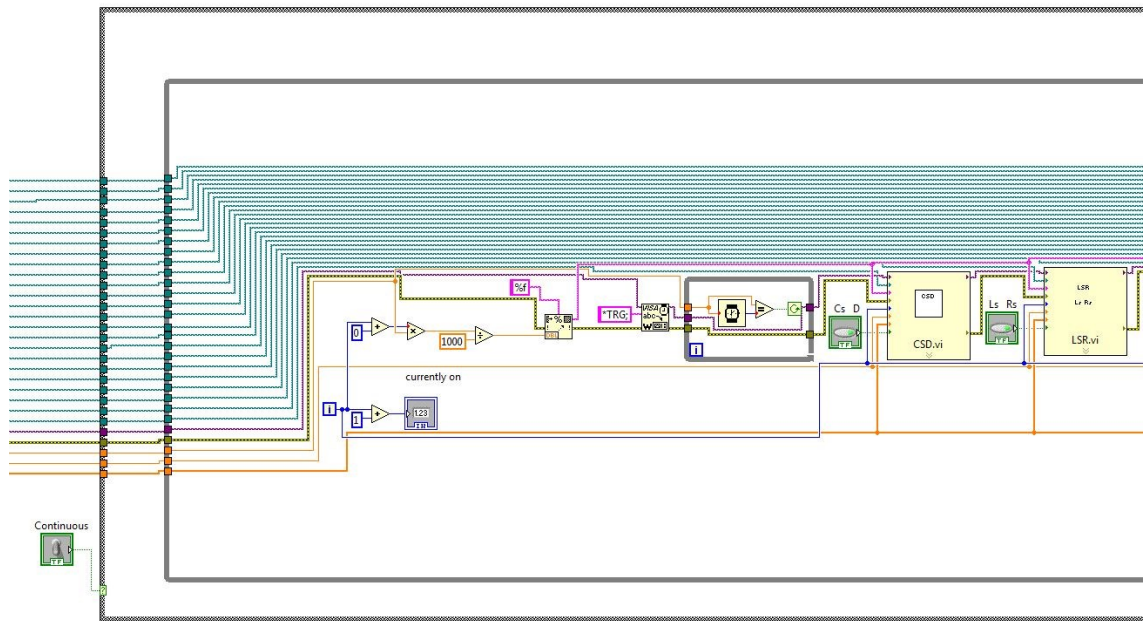


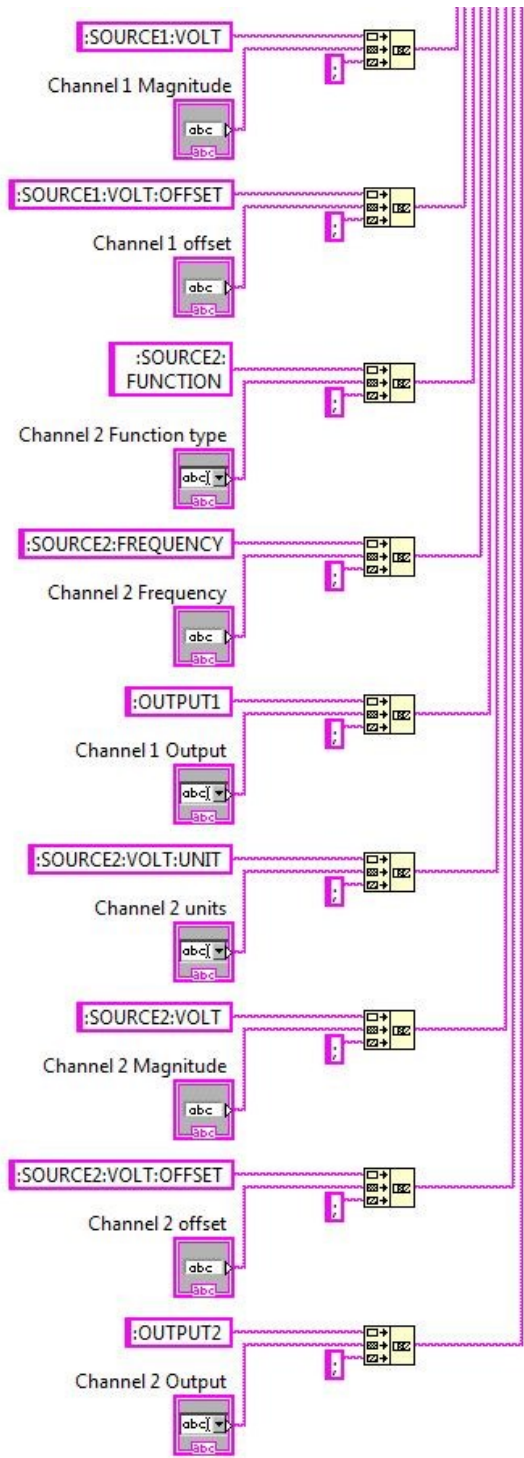


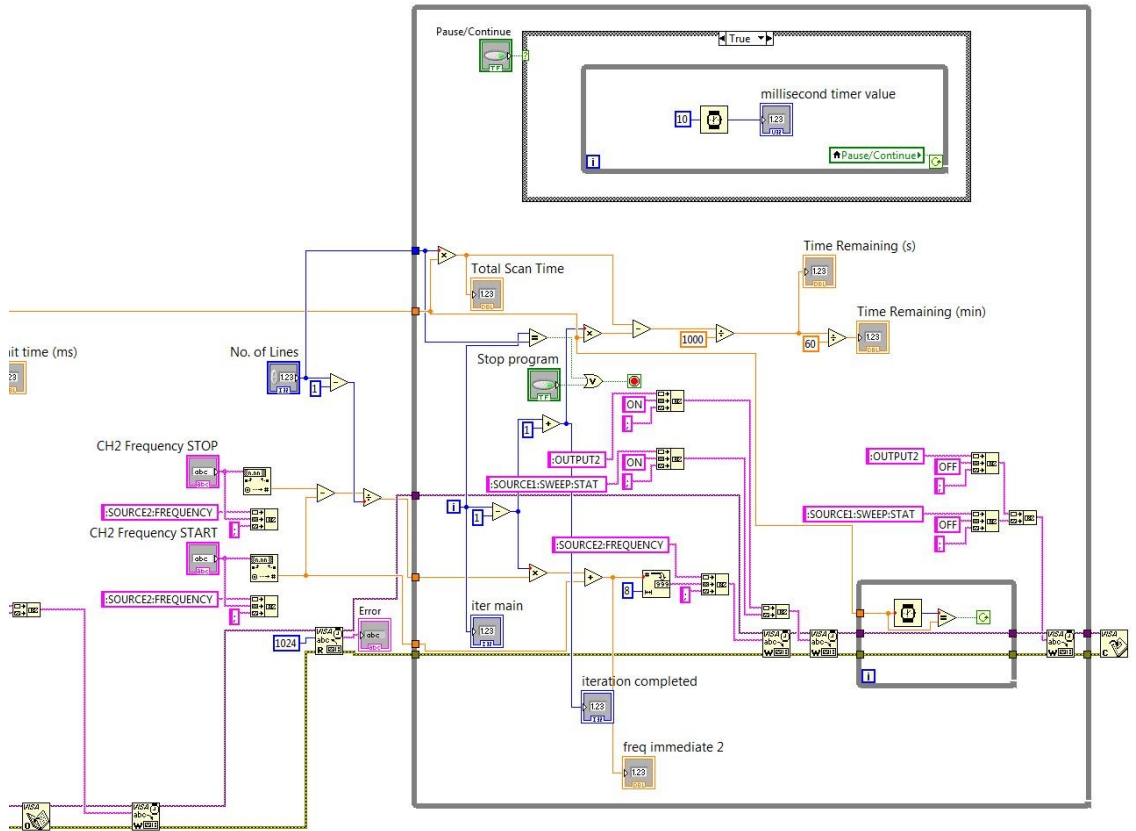












MatLab 2017A code

```
clear ALL;
%assign Base QTF frequency
f0=2^15;
%assign a0L = 1.87510
a0L=1.87510;
a0L2=(1.87510*1.87510);
a0L3=(a0L2*1.87510);
base=(f0/a0L2);

fn=f0*5;
f=(f0-2500):10:fn;
delf=(f./f0);
Kpointmass=((delf).^2)-1;
root=(sqrt(delf));
%f0sqr=(f0.*f0);
%fsqr=(f.*f);
%fdivsqr=(fsqr./f0sqr);
%a0L4=(a0L3*1.87510);
%Bob=(fsqr./f0sqr);
%Bob2=(a0L4.*Bob);
%Bob3=(sqrt(Bob2));
%aL=(sqrt(Bob3));
a0Lroot=(sqrt(1.87510));
%aL=(a0Lroot.*root);

%degrad=(pi/180);
%aL=root.*(1.87510);
aL=((sqrt(delf)).*1.87510);
D=sin(aL);
E=sinh(aL);
F=cos(aL);
G=cosh(aL);
%funct1=((D.*G)-(F.*E)); %trig (sin(aL) cosh(aL)-cos(aL) sinh(aL))
funct1=((F.*E)-(D.*G)); %trig (cos(aL) sinh(aL)-sin(aL) cosh(aL))
%funct2=- (1+(F.*G)); % trig -(1+cos(aL) cosh(aL))
funct2=(1+(F.*G)); % trig (1+cos(aL) cosh(aL))

f2=funct2./funct1;
%f3=((f2.*aL3)./3);
aL2=(aL.*aL);
aL3=(aL2.*aL);
f3=((f2.*aL3)./3);
kratio=f3;
f5=abs(Kpointmass-kratio);
```

```

figure
%subplot(2,2,1);
%semilogx(Kp,delf);
%axis([0.01 100 0 5])

%subplot(2,2,2);
%semilogx(f4,delf)
%axis([0.01 10 0 5])
%subplot(2,2,3);

% sensitivity of pointmass
del=(sqrt(1+kratio));
dell=(1./del);
del2=(1/2).*dell;
dwdk=del2;

subplot(3,2,1);
semilogx(Kpointmass,delf,kratio,delf)
axis([0.01 1000 0.5 5])
ylabel('f/f0')
xlabel('k*/kc')
legend('Point mass','Beam','Location','northwest')

subplot(3,2,2);
semilogx(Kpointmass,delf,kratio,delf)
axis([0.1 1.5 1.0 1.5])
ylabel('f/f0')
xlabel('k*/kc')
legend('Point mass','Beam','Location','northwest')

%df/dk calculation
D=sin(aL);
E=sinh(aL);
F=cos(aL);
G=cosh(aL);

H=(F.*E); %cos sinh
I=(D.*G); %sin cosh
J=(D.*E); %sin sinh
K=(F.*G); %cos cosh

L1=(2.*aL);
L2=(H-I); % (cos sinh - sin cosh)
Ltot=(L1.*L2); % (2aL) (cos sinh - sin cosh)
%Ltottot=(base.*Ltot);

M1=(3.*(aL2));
M2=(1+K); %trig (1+cos cosh)
Mtot=(M1.*M2); % 3(aL^2) (1+cos cosh)

N1=(aL3); % (aL^3)

```

```

N2=(H-I); % (cos sinh - sin cosh)
Ntot=(N1.*N2); % (aL^3) (cos sinh - sin cosh)

O1=(2.*kratio);
Otot=(O1.*J); % 2*kratio(sin sinh)

Bottom=(Mtot+Ntot+Otot);

% Ltotpap=(Ltot./3.5160);
% dfdk=(Ltotpap./Bottom);
dfdk=(Ltot./Bottom);

dfdbn1=((2.*aL.*((cos(aL).*sinh(aL))-
(sin(aL).*cosh(aL)))))/((3.*aL.*aL.*(1+cos(aL).*cosh(aL)))+(aL.*aL.*
aL.*((cos(aL).*sinh(aL))-
(sin(aL).*cosh(aL))))+(2.*kratio.*(sin(aL).*sinh(aL)))));

h1=6.*aL.*(cos(aL).*sinh(aL))-sin(aL).*cosh(aL);
h2=3.*aL2.*(1+(cos(aL).*cosh(aL)));
h3=aL3.*(cos(aL).*sinh(aL))-sin(aL).*cosh(aL);
h4=6.*kratio.*(sin(aL).*sinh(aL));
h5=(h2+h3+h4).*a0L2;
h6=h1./h5;

g1=(f0./a0L);
dfdk2=(dfdk./g1);
kratio2=(kratio.*10);

krar=kratio.*10;
subplot(3,2,5);
loglog(kratio,h6,kratio,dwdk)
axis([0.01 1000 0.0001 1])
ylabel('sensitivity')
xlabel('k*/kc')
legend('Distributed Beam sensitivity','pointmass
sensitivity','Location','southwest')

% dfdk=((32768/(1.8751*1.8751))*((2.*aL).*((cos(aL).*sinh(aL))-
(sin(aL).*cosh(aL)))))/((3.*(aL.*aL.*aL.*(1+cos(aL).*cosh(aL)))+(a
L.*aL*aL.*(cos(aL).*sinh(aL))-
sin(aL).*cosh(aL))))+(2.*kratio.*(sin(aL).*sinh(aL))))

subplot(3,2,6);
loglog(kratio,h6,kratio,dwdk)
axis([0.001 1 0.3 0.6])
ylabel('sensitivity')
xlabel('k*/kc')
legend('Distributed Beam sensitivity','Pointmass
sensitivity','Location','southwest')

subplot(3,2,3);
semilogx(Kpointmass,delf,kratio,delf)

```

```

axis([0.0001 1 0.9999 1.0035])
ylabel('f/f0')
xlabel('k*/kc')
legend('Point mass','Beam','Location','northwest')

```

```

f6=(Kpointmass+kratio)./2;
f7=((f5./f6).*100);
%f8=abs((Kpointmass./kratio)-1);
%f9=f8.*100;
%f10=(f5.*100);

```

```

subplot(3,2,4);
loglog(kratio,f7)
axis([0.01 10 1 100])
ylabel('% difference')
xlabel('k*/kc')
legend('% Difference of models','Pointmass
sensitivity','Location','northwest')

```

```

%filename1='kpointmass.csv';
%csvwrite(filename1,Kpointmass)
%filename2='delf.csv';
%csvwrite(filename2,delf)
%filename3='kratio.csv';
%csvwrite(filename3,kratio)
%filename4='beamsensitivity.csv';
%csvwrite(filename4,h6)
%filename5='PointMassSensitivity.csv';
%csvwrite(filename5,dwdek)

```

```

%subplot(2,2,2);
%semilogx(kratio,delf)%
%axis([0 100 0 10])

```